

High Precision Diagnostics of Ultrashort High-Power Laser for Strong-Field QED Experiments

Dissertation

zur Erlangung des akademischen Grades
doctor rerum naturalium (Dr. rer. nat.)



Fakultät für Mathematik und Physik
Albert-Ludwigs-Universität Freiburg

von **Xinhe Huang**, M. Sc.
geboren am 28.08.1994 in Taicang, China

Betreuer

1. **Prof. Dr. Beate Heinemann**
Universität Hamburg
Deutsches Elektronen-Synchrotron DESY
2. **Prof. Dr. Matt Zepf**
Institut für Optik und Quantenelektronik
Friedrich-Schiller-Universität Jena
3. **Dr. Alexander Sävert**
Institut für Optik und Quantenelektronik
Friedrich-Schiller-Universität Jena

Gutachter

1. **Prof. Dr. Beate Heinemann**
Universität Hamburg
Deutsches Elektronen-Synchrotron DESY
2. **Prof. Dr. Giuseppe Sansone**
Freiburg Institute for Advanced Studies (FRIAS)
Albert-Ludwigs-Universität Freiburg
3. **Prof. Dr. Heidi Rzehak**
Theorie der Elementarteilchen und Quantenfeldtheorie
Albert-Ludwigs-Universität Freiburg

Dekan

Prof. Dr. Michael Růžička
Fakultät für Mathematik und Physik
Albert-Ludwigs-Universität Freiburg

Tag der Disputation: 09. 12. 2024

Abstract

Strong-Field Quantum Electrodynamics (SFQED) investigates the behavior of light and matter interactions in extremely intense electromagnetic fields, where non-perturbative effects become significant. The LUXE (Laser Und XFEL Experiment) project aims to explore the SFQED with unprecedented precision. By colliding high-power laser beams with electron bunches from the European XFEL or a secondary high-energy photon beam, LUXE seeks to investigate non-perturbative processes such as non-linear Compton scattering, Breit-Wheeler pair production, and the trident process. LUXE explores an uncharted domain by reaching the Schwinger critical field for the first time. However, the precision measurement of processes in SFQED experiments is challenged by shot-to-shot intensity fluctuations of ultrashort laser pulses.

This thesis describes the high-precision on-shot intensity measurement of ultrafast high-power laser pulses required by the LUXE project. The goal is to achieve a precision of 1%.

The first step is to image the focal spot at the interaction point to the diagnostic system to ensure a high-precision measurement. This thesis numerically investigates a proposed setup regarding the aberrations of the beam in terms of long-distance propagation and relay imaging of the focal spot to the diagnostic system.

To fully characterize the intensity, a diagnostic system is designed and implemented on the JETi200 laser, which includes measuring the focal spot image using a high-resolution imaging system, near-field image, spectrum using a spectrometer, and pulse duration using a single-shot technique. Furthermore, an on-shot intensity tagging method with high precision for relative intensity diagnostics was developed. This method involves utilizing second harmonic generation to create a nonlinear replica of the focal spot and measuring the ratio of the peak fluences between the fundamental beam and the corresponding second harmonic beam.

The presence of spatial-temporal couplings necessitates a three-dimensional characterization of the focal spot. It can be achieved by two methods, using the INSIGHT technique and measuring the wavefront of each wavelength, as a verification and cross-check of INSIGHT measurement. This allows for the characterization of STCs, obtaining the transversal and longitudinal focal shift, and thus the local temporal profile, resulting in the determination of the intensity at local positions across the

focal spot.

The diagnostic system developed can be applied to more complex laser structures such as Laguerre-Gaussian beams with OAM. The characterization and optimization of beams with OAM are described as well.

Zusammenfassung

Starkfeld-Quantenelektrodynamik (SFQED) untersucht das Verhalten von Licht- und Materie-Interaktionen in extrem intensiven elektromagnetischen Feldern, wo nicht-perturbative Effekte signifikant werden. Das LUXE (Laser Und XFEL Experiment) Projekt zielt darauf ab, SFQED mit beispielloser Präzision zu erforschen. Durch die Kollision von Hochleistungslaserstrahlen mit Elektronenbündeln aus dem Europäischen XFEL oder einem sekundären Hochenergie-Photonenstrahl will LUXE nicht-perturbative Prozesse wie nichtlineare Compton-Streuung, Breit-Wheeler-Paarbildung und den Trident-Prozess untersuchen. LUXE betritt ein unerforschtes Gebiet, indem es zum ersten Mal das Schwinger-Kritikfeld erreicht. Allerdings wird die präzise Messung von Prozessen in SFQED-Experimenten durch Schuss-zu-Schuss-Intensitätsschwankungen ultrakurzer Laserpulse erschwert.

Diese Arbeit beschreibt die hochpräzise Messung der Intensität von ultrakurzen Hochleistungslaserpulsen, die für das LUXE-Projekt erforderlich ist. Das Ziel ist es, eine Präzision von 1 % zu erreichen.

Der erste Schritt besteht darin, den Fokuspunkt am Interaktionspunkt zum Diagnosesystem zu bilden, um eine hochpräzise Messung zu gewährleisten. Diese Arbeit untersucht numerisch einen vorgeschlagenen Aufbau hinsichtlich der Aberrationen des Strahls in Bezug auf die Fernfeld-Ausbreitung und die Relaisabbildung des Fokuspunkts zum Diagnosesystem.

Um die Intensität vollständig zu charakterisieren, wird ein Diagnosesystem am JETi200-Laser entworfen und implementiert, das die Messung des Fokuspunktbildes mit einem hochauflösenden Abbildungssystem, des Nahfeldbildes, des Spektrums mit einem Spektrometer und der Pulsdauer mit einer Einzelschuss-Technik umfasst. Darüber hinaus wurde eine hochpräzise On-Shot-Intensität-Tagging-Methode für relative Intensitätsdiagnostik entwickelt. Diese Methode beinhaltet die Nutzung der zweiten Harmonischen Erzeugung zur Erstellung einer nichtlinearen Replik des Fokuspunkts und die Messung des Verhältnisses der Spitzenfluenz zwischen dem fundamentalen Strahl und dem entsprechenden zweiten harmonischen Strahl.

Die Anwesenheit von räumlich-zeitlichen Kopplungen erfordert eine dreidimensionale Charakterisierung des Fokuspunkts. Dies kann durch zwei Methoden erreicht werden, die INSIGHT-Technik und die Messung der Wellenfront jeder Wellenlänge, als Verifika-

tion und Kreuzprüfung der INSIGHT-Messung. Dies ermöglicht die Charakterisierung von STCs, das Erhalten der transversalen und longitudinalen Fokalverschiebung und somit das lokale zeitliche Profil, was zur Bestimmung der Intensität an lokalen Positionen im Fokuspunkt führt.

Das entwickelte Diagnosesystem kann auf komplexere Laserstrukturen wie Laguerre-Gauss-Strahlen mit OAM angewendet werden. Die Charakterisierung und Optimierung von Strahlen mit OAM wird ebenfalls beschrieben.

Contents

Abstract	iii
Zusammenfassung	i
1 Introduction	1
1.1 LUXE Project at DESY	1
1.2 Precision Laser Intensity Diagnostics	7
1.3 Laser Pulse Characterizations	8
1.4 Thesis Outline	11
2 Theory	13
2.1 Ultrashort Laser Pulses in Temporal and Spectral Domains	13
2.1.1 Temporal-Domain Description of Ultrashort Laser Pulses	13
2.1.2 Spectral-Domain Description of Ultrashort Laser Pulses	14
2.1.3 Fourier Transform Relationship	14
2.1.4 Magnetic Field Description	15
2.1.5 Intensity	16
2.1.6 Gaussian Pulse Example	17
2.1.7 Temporal and Spectral Phase	18
2.2 Laser Pulses in the Spatial Domain	20
2.2.1 Near-Field Diffraction	21
2.2.2 Far-Field Diffraction	22
2.2.3 Gaussian Beam Propagation	23
2.2.4 Non-Gaussian Beams	25
2.2.5 Laguerre-Gaussian Beams	27
2.2.6 Zernike Polynomials	28
2.3 Spatial-Temporal Couplings	31
2.4 Second Harmonic Generation	33
3 Point-to-Point Imaging of Focal Spot	37
3.1 Pulse aberrations in the transversal plane	37

3.2	Simulations of two imaging setups using Zemax	41
3.2.1	Imaging setup using 3 parabolic mirrors	41
3.2.2	Imaging setup for direct imaging	42
3.2.3	Comparison of two setups	43
4	Full On-Shot Laser Intensity Diagnostics	47
4.1	Experiment setup	47
4.2	JETi200 laser system	48
4.3	Precision Assessment on Laser Intensity Diagnostics	50
4.4	Near Field	53
4.5	Focal Spot	53
4.5.1	Focal Spot	53
4.5.2	High Dynamic Range	55
4.6	Energy	56
4.6.1	Spectrum	57
4.6.2	Calculation of Energy	59
4.7	Characterization of Pulse Temporal Profile	60
4.7.1	Self-Referenced Spectral Interferometry	60
4.7.2	Results	64
4.8	Temporal Contrast	65
4.9	Laser Stability	66
5	Laser Intensity Tagging Using Nonlinear Optical Process	75
5.1	Experimental Setup	75
5.2	Results and Discussions	77
6	Three-dimensional Characterization of Ultrashort Laser Pulses	85
6.1	Method	85
6.1.1	INSIGHT	85
6.1.2	Spectrally-Resolved Wavefront Measurement	88
6.1.3	Longitudinal Focal Shift Measurement	88
6.2	Results	89
6.2.1	Spectrally-Resolved Wavefront	89
6.2.2	Spectrally-Resolved Far-Field	90
6.2.3	Longitudinal Focal Shift	93
6.2.4	Local Spectrum and Local Temporal Profile	97

7	Characterization and Optimization of Laguerre-Gaussian Laser Pulses with Orbital Angular Momentum	101
7.1	Characterization of Laser Pulse with Orbital Angular Momentum . . .	102
7.1.1	Influence from Near-field Intensity Profile	103
7.1.2	Influence from Alignment of the Singularity Point	104
7.1.3	Influence from Wavefront Aberrations	106
7.1.4	Influence from Different Spectral Components	107
7.1.5	Influence from Spiral Phase Plate	107
7.2	Optimization of beam with OAM	109
8	Conclusion and Outlook	115
8.1	Conclusion	115
8.2	Outlook	116
	Bibliography	118
	Danksagung	131

1 Introduction

1.1 LUXE Project at DESY

Quantum electrodynamics (QED) is a field of physics that investigates the interactions between light and matter. It has been investigated and measured with remarkable precision in many experiments, contributing significantly to the understanding of the quantum world [1]. In QED, perturbative methods involve expanding interactions in terms of a small parameter, typically the fine-structure constant α [2], allowing accurate calculations for weak fields. However, exploring the strong-field regime of QED (SFQED), where non-perturbative effects become prominent, remains a frontier largely uncharted by experimental physics. In these regimes, new approaches are needed to understand phenomena where interactions cannot be treated as small perturbations. Especially, the processes to explore in SFQED are the non-linear Compton scattering, represented by $e^- + n\gamma_L \rightarrow e^- + \gamma$ [3], where n is the number of laser photons γ_L ; Breit-Wheeler pair production, expressed as $\gamma + n\gamma_L \rightarrow e^- + e^+$ [4, 5]; the two-step trident process where the photon from the Compton process interacts subsequently with laser photons and an e^-e^+ pair is produced via the Breit-Wheeler process [6, 7]; quantum radiation reaction, where multiple photons are emitted by a single high-energy electron, causing the back-reaction on the radiating electrons [8].

In quantum mechanics and QED, the vacuum is not simply empty space but a dynamic environment filled with fluctuating energy and virtual particles [10]. These virtual particles constantly create and annihilate. A significant concept related to these fluctuations is the Schwinger critical field, defined by the equation $E_{cr} = m_e^2 c^3 / (e\hbar) = 1.32 \times 10^{18}$ V/m [5, 11]. This critical field represents the electric field strength required to create electron-positron pairs from the vacuum over a Compton wavelength. In the weak-field regime below this critical field, the strong-field effects, like Breit-Wheeler

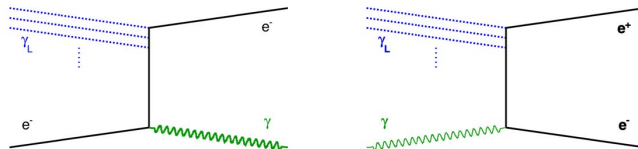


Figure 1.1: The scheme for the Compton scattering and Breit-Wheeler pair production process. [9]

pair production, are exponentially suppressed and hence difficult to measure [12]. Although this critical field has not been experimentally achieved in laboratories, it is believed to exist naturally in extreme environments such as the surface of neutron stars [13] or during interactions at future linear high energy lepton colliders [14].

An important parameter used to characterize the laser intensity is the so-called laser normalized vector potential a_0 , which is defined as $a_0 = eE_L/m_e\omega_L$, where e is the electron charge, E_L the electric field of laser, m_e the mass of the electron at rest, and ω_L the angular frequency of laser. The region $a_0 \ll 1$ corresponds to the perturbative regime. Another key parameter is the quantum non-linearity parameter, χ_e , which corresponds to the ratio of the laser field to the critical field in the rest frame of an electron, $\chi_e = E_*/E_{cr}$.

In the 1990s, at the Stanford Linear Accelerator Center (SLAC), the E144 experiment was the first experiment colliding laser fields with electrons [15, 16]. It explored non-linear Compton scattering and pair production by colliding a 46.6 GeV electron beam and laser pulses with intensities around 5×10^{17} W/cm², with $a_0 \leq 0.4$ and $\chi_e \leq 0.25$. E144 successfully measured non-linear Compton scattering and the trident process. However, it was still within the perturbative regime and did not reach the critical field. Additionally, the experiment results showed considerable uncertainties related to laser intensity.

The experiment conducted at the Astra-Gemini laser system at the Rutherford Appleton Laboratory (RAL) produced electron beams up to 2 GeV through laser wakefield acceleration (LWFA) and interacted them with laser pulses ($a_0 = 10$) [17]. However, with $\chi_e < 1$, the experiment were unable to clearly observe quantum radiation reaction. At present, experiments have been proposed to explore the SFQED processes with $a_0 > 1$ and $\chi_e > 1$. The E320 experiment is ongoing at SLAC, utilizing the FACET-II facility, by colliding a 13 GeV electron beam and a 16 TW laser [18]. The FOR2783 at the ATLAS laser at the Centre of Advanced Laser Applications (CALA) employs electron beams with an energy of 2.5 GeV from laser-plasma acceleration and intense laser pulses with $a_0 \approx 66$ [19].

The LUXE (Laser Und XFEL Experiment) project [9] is a proposed experiment at DESY (Deutsches Elektronen-Synchrotron) in Hamburg which explores the strong-field regime of QED with high precision. Compared to other SFQED experiments, the LUXE project explores an unexplored regime of electron-laser interactions where $a_0 \gg 1$ and $\chi_e \sim 1$ by reaching the Schwinger critical field for the first time. Fig.1.2 a)

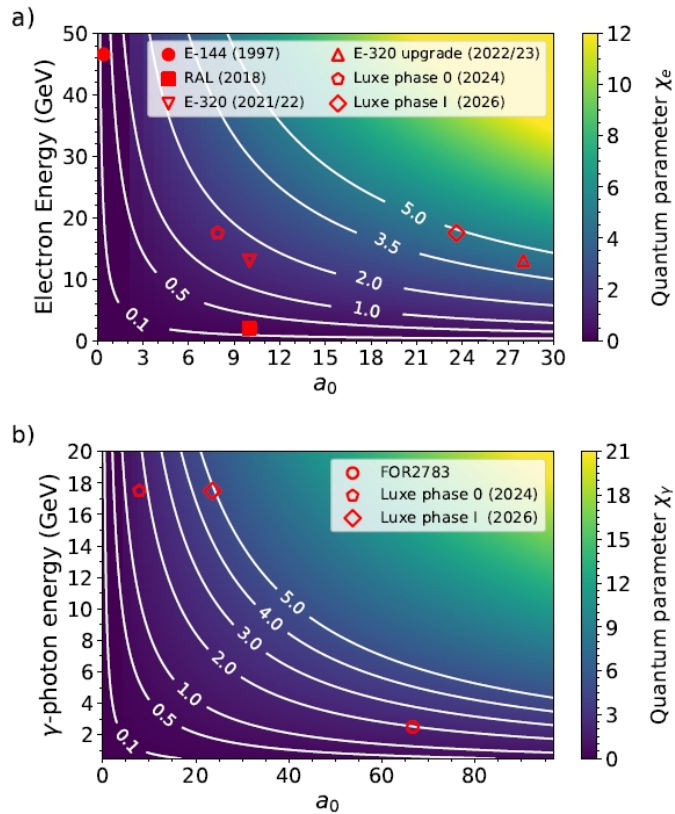


Figure 1.2: (a) Electron quantum parameter χ_e for different a_0 . (b) Dependence of χ_γ on γ -ray energy and a_0 for 800 nm. [19]

shows the different regimes of electron-laser interactions of several experiments, while the dependence of the parameter χ_γ on the γ -photon energy and a_0 for photon-laser collision experiments is presented in Fig.1.2 b) [19]. Additionally, LUXE performs measurements with exceptionally high precision on the non-perturbative processes such as nonlinear Compton scattering, nonlinear Breit-Wheeler pair production, and the trident process. The experimental approach involves colliding tightly focused, high-power laser beams with either the electron bunches from the European XFEL (X-Ray Free-Electron Laser) or a secondary high-energy photon beam, at a repetition rate of 1 Hz. The experiment's primary goals include the precision measurement to explore the transition into the non-perturbative regime of QED and to search for new particles beyond the Standard Model that interact with photons. Specifically, LUXE aims to:

- Measure the interactions between real photons, electrons, and other photons at field strengths where the coupling to charges becomes non-perturbative.

- Perform precision measurements of electron-photon and photon-photon interactions during the transition from the perturbative to the non-perturbative regime of QED.
- Utilize strong-field QED processes to design a highly sensitive search for new particles beyond the Standard Model that couple to photons, such as axion-like particles (ALPs) [20, 21].

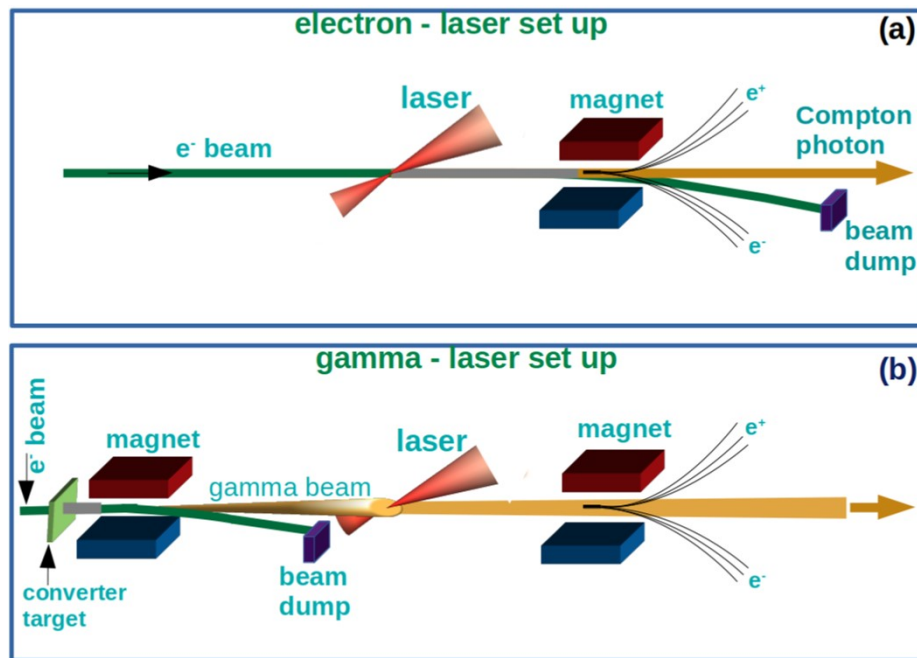


Figure 1.3: Interaction between the ultrashort high-power laser and (a) high-energy electron beams, or (b) γ -photons. [9]

The LUXE project investigates the processes through two distinct experimental schemes, as illustrated in Fig.1.3. The first scheme, shown in Fig.1.3(a), involves a high-intensity laser colliding with an electron beam, with an energy range of 9-17 GeV. In the second scheme shown in Fig.1.3(b), the high-energy electron bunches interact with a bremsstrahlung target, converting them into high-energy photons (γ beam), which are subsequently made to collide with the laser pulses. The project aims to perform precise measurements of non-linear Compton scattering and Breit-Wheeler pair production, as well as the trident process.

To explore these phenomena, it is necessary to reach the Schwinger field. The development of ultrashort, high-intensity lasers has provided a promising tool for experiments that can achieve the Schwinger limit. The technique, known as chirped pulse amplification (CPA, Nobel Prize 2018) [22] amplifies the laser pulse energy to the order

of several or 100s of joules and compresses the pulse length to a few femtoseconds, resulting in a focal peak intensity exceeding 10^{23} W/cm² [23]. While this intensity corresponds to an electric field of approximately 10^{15} V/m in the laboratory frame, it is still three orders of magnitude below E_{cr} .

However, according to the laws of relativity, high-energy electrons with a relativistic gamma factor $\gamma_e \gg 1$ will see a Lorentz-boosted electric field E_* at the order of E_{cr} in their own rest frame, where $E_* = \gamma_e E_L (1 + \cos\theta)$, with θ the collision angle and E_L the laser electric field. This means that the LUXE project can reach the SFQED regime by using high-energy electron beams or photons colliding with intense laser pulses with a power of up to 350 TW.

In phase 0 of LUXE, a laser with a power of 40 TW will be employed and will be focused to about 8 μm , and later further down to 3 μm , to scan the SFQED parameter space. The laser will operate at a repetition rate of 1 Hz with a pulse duration of 30 fs. An intensity of up to 1.3×10^{20} W/cm² will be achieved, to enter a regime where non-perturbative quantum effects become likely ($\chi_e \sim 1$). In phase 1, the laser will be upgraded to 350 TW to reach an intensity of up to 1.2×10^{21} W/cm². It becomes possible to explore the super-critical regime up to $\chi_e \sim 3$. The parameters concerning the laser both before and after the upgrade are listed in the Table 1.1.

However, the LUXE project encounters challenges related to shot-to-shot variations

	Phase 0	Phase 1
Laser power (TW)	40	350
Laser energy after compression (J)	1.2	10
Laser focal spot waist w_0 (μm)	3	3
Focus peak intensity ($\times 10^{20}$ W/cm ²)	1.33	12
Peak intensity parameter a_0	7.9	23.6
Quantum parameter χ_e		
for $E_e=14.0\text{GeV}$	1.28	3.77
for $E_e=16.5\text{GeV}$	1.5	4.45
for $E_e=17.5\text{GeV}$	1.6	4.72

Table 1.1: Parameters for different initial laser power and focusing geometries planned for the different phases of the LUXE experiment. The quantum parameter χ_e is given for three different electron energies.

in electron and laser parameters, which impact the precision of measurements. Even though the project benefits from the long-term stable operation of high-power laser systems, which typically exhibit a stability level within several percent for pulse pa-

rameters, this level of stability still presents issues. For example, the low event rate ($\ll 1$ per shot) of Breit-Wheeler pair production in certain configurations, demands extremely accurate and precise pulse characterization techniques. This challenge is illustrated by the simulation results for the Breit-Wheeler pair production rate as a function of the laser intensity parameter a_0 , as shown in Fig.1.4 [24]. A mere 2.5%

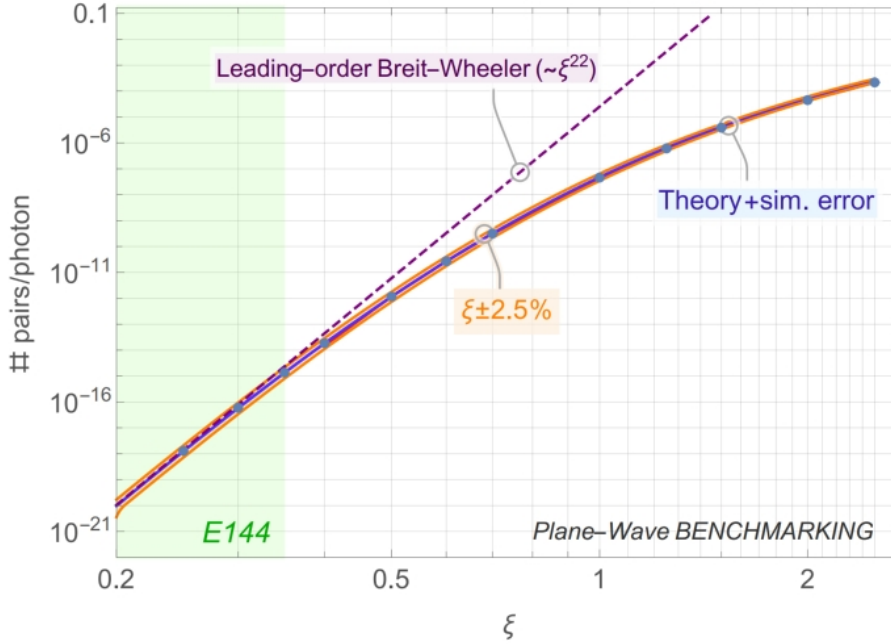


Figure 1.4: Number of pairs per photon versus ξ (which is denoted as a_0 in this thesis) for phase-0 and phase-1. The uncertainty of $\pm 2.5\%$ highlights the precision required in laser intensity to achieve high-precision experimental results. [24]

variation in a_0 can lead to a substantial uncertainty of up to 40% in the pair production rate.

The goal of the LUXE project is to achieve measurements of SFQED processes with high precision that permits a detailed comparison of the measured data with theoretical calculations. This objective necessitates extremely accurate measurements of laser intensity. To meet this requirement, the project is targeting a precision of 5% for the absolute measurement of laser intensity, based on the simulations involving ponderomotive scattering electrons, as detailed in [25]. Additionally, the project requires a higher precision of 1% in the relative measurement of the laser intensity parameter. This doctoral thesis presents the development and implementation of a state-of-the-art laser diagnostics suite, specifically designed to fulfill LUXE’s goal of the relative laser intensity measurement with a precision of better than 1%.

1.2 Precision Laser Intensity Diagnostics

Ultrashort high-power laser systems based on the technique of CPA are employed in the research on SFQED. Ultra-intense lasers with power in the order of petawatt are rapidly being developed all over the world, including facilities such as Apollon at LULI in France [26], ATLAS-3000 at CALA in Germany [27], BELLA at Lawrence Berkeley National Laboratory in the USA [28], and ELI-NP in Romania [29], and the highest laser peak intensity at present can reach over 10^{23} W/cm² in CoReLS in South Korea [23]. However, laser intensity fluctuations are a common problem that can impact the performance and reliability of laser systems. The major contributions to the shot-to-shot intensity fluctuations of the laser pulse are changes in both spatial and spectral phases. They can be caused by environmental factors such as air current flow, thermal drift, and mechanical vibrations in the laser laboratory. Specifically, spatial profile fluctuations arise from intensity-dependent variations in nonlinear wavefront distortion and fluctuations in the pump-beam profiles. Temporal profile fluctuations, on the other hand, result from intensity-dependent changes in self-phase modulation [30]. Together, these spatial and temporal instabilities cause variations in focal spot size and temporal profile, ultimately leading to unstable peak intensity. In the JETi200 laser laboratory, where the experiments in this thesis were performed, effective measures have been implemented to control the room temperature and humidity using an air-conditioning system and to prevent air currents by enclosing the laser system in boxes. However, the passive stabilization approach to seal the entire laser system into a vacuum chamber, which eliminates most environmental disturbances, can be inconvenient for daily maintenance.

Instead of focusing solely on stabilizing the laser output, another approach is to perform laser on-shot diagnostics. This is made possible because, in the LUXE experiment, the laser pulses are not distorted or absorbed after interacting with electron bunches.

The state-of-the-art measurement of the laser pulse intensity is essential to ensure the precision and the reproducibility of the experimental data for the LUXE project. In recent years, various methods to directly measure ultra-high laser intensities with absolute values have been proposed. One method analyses the ionization of atoms and molecules by ultra-intense laser pulses [31–36]. Other methods measure the pulse intensity by analysing scattered electrons from laser-plasma acceleration [37–40], or Thomson scattering [41, 42]. These methods are limited to low laser peak intensi-

ties up to 10^{15} W/cm² to circumvent ionization saturation. At intensities above 10^{22} W/cm² the dependence of positron yield on laser intensity in laser-foil interactions can be used [43], but with several percent accuracy. Also, the absolute measurement of laser intensity based on the simulations involving ponderomotive scattering electrons, discussed in [9] and detailed in [25], presents a precision of 5%, which would not be sufficient for the LUXE project.

To achieve high-precision measurements of SFQED processes, this thesis project is to develop a diagnostic system to tag the relative laser pulse intensity shot-to-shot with the goal of achieving a precision of better than 1%.

1.3 Laser Pulse Characterizations

Usually, the laser pulse peak intensity is derived through a calculated approach, using the following equation to determine the laser intensity I :

$$I = \frac{E}{\tau A} \tag{1.1}$$

where E is the pulse energy, τ is the full-width-at-half-maximum (FWHM) pulse temporal duration and A is the FWHM area of the laser beam's transversal plane. Each of these parameters is measured independently.

In the realm of ultrafast optics, characterizing the complex electric field of ultrashort laser pulses in the temporal or spectral domain is challenging, as the pulse duration is of the order of a few ps or even down to a few fs. These pulses are too short for direct measurement with conventional electronic devices, necessitating the development of advanced optical techniques to resolve the amplitude and spectral phase of light pulses across such short time scales.

Frequency-Resolved Optical Gating (FROG) [44, 45] is a well-established method that offers a comprehensive characterization of ultrashort pulses by measuring the intensity and phase across different frequencies and time delays. It relies on creating a nonlinear optical interaction between the pulse under examination and a reference pulse, generating a spectrogram that encodes the pulse's properties. The spectrogram provides information about the pulse, including phase distortions and temporal features.

On the other hand, Spectral Phase Interferometry for Direct Electric-field Recon-

struction (SPIDER)[46] offers a more direct approach to pulse characterization by employing spectral shearing interferometry. In SPIDER, two replicas of the pulse are created, spectrally shifted (sheared) relative to each other, and then overlapped in a non-linear crystal to produce an interference pattern. This pattern directly reveals the spectral phase differences induced by the shearing, allowing for a straightforward reconstruction of the pulse's electric field.

Another technique is the dispersion scan (D-scan)[47] which involves measuring the spectral phase of a laser pulse by introducing variable dispersion (e.g., by changing the glass thickness in the beam path) and recording the spectrum of the pulse after nonlinear frequency conversion (usually second-harmonic generation). The technique reconstructs the pulse by analyzing how its spectrum changes with the introduced dispersion. However, it requires multiple shots to span the range of dispersions, impacting the accuracy of the measurement due to variations between shots. To address this limitation, a single-shot D-scan has been proposed for real-time measurements. It involves an imaging spectrometer, a prism, and a transversal SHG crystal, and demands a fine alignment to minimize aberrations. Moreover, it is highly dependent on the uniformity of the beam intensity profile. Variations in beam homogeneity can significantly affect the reliability of the measurement.

In this study, the commercial device Wizzler from Fastlite is utilized to measure the ultrashort pulse duration. The Wizzler, based on the principle of Self-Referenced Spectral Interferometry (SRSI)[48], generates the reference beam directly from the pulse under investigation, which substantially simplifies the setup. SRSI is able to achieve a temporal dynamic range of over 40 dB due to the temporal contrast enhancement by a third-order nonlinear optical process [49], which is the cross-polarized wave generation (XPW) [50], utilizing a standard spectrometer that offers only a 20 dB spectral signal-noise-ratio (SNR).

In the spatial domain, one crucial parameter of laser characterization is the wavefront, which significantly impacts the quality of the focal spot and the peak intensity. Typically, the Shack-Hartmann wavefront measurement segments the incoming beam using a lenslet array. By analyzing the deviations of the focal spots of each beam segment focused by a lenslet, the local wavefront gradient across each segment can be determined to reconstruct the wavefront. However, the spatial resolution is limited by the size of lenslets in the array and the beam size to be measured is limited by the number of lenslets.

In this study, SID4 HR from Phasics is used to measure the beam wavefront. SID4 using a diffractive grating and the technique of quadrawave lateral shearing interferometry (QWLSI)[51] offers higher spatial resolution and phase accuracy. The SID4 provides a higher phase and intensity sampling resolution of 416×360 [51] compared to the Shack-Hartmann wavefront measurement device, such as HASO4 from Imagine Optics with a resolution of 68×50 [52]. In terms of wavefront accuracy, the HASO4 achieves $\lambda/100$ accuracy, which is 8 nm for the laser system with a central wavelength of 800 nm, while the SID4 delivers an accuracy of less than 2 nm root-mean-square (RMS). This technology is more suitable for this research needs where precise wavefront characterization is essential.

The calculation of laser pulse intensity using Eq.2.63 can be accurate only under the assumption that these parameters are all independent of each other [23, 28]. However, the presence of spatial-temporal couplings (STC), where the spatial and temporal distribution of the beam is dependent on its spectrum, makes the laser pulse intensity characterization more complicated. Advanced techniques now enable measurements of the laser's complex electric field in three dimensions, allowing for a comprehensive reconstruction of the laser profile beyond the limitations of traditional tools that measure parameters in only the spectral or spatial domain. Two techniques, TERMITES [53] and INSIGHT [54], can be employed to characterize the three-dimensional electric field of the laser pulses in both spatial and spectral domains.

TERMITES, which stands for ‘total E-field reconstruction using a Michelson interferometer temporal scan’, is a 3D interferometric technique that combines a beam under investigation self-referencing with its radially stretched beam to produce a spatially-resolved cross-correlation function. The corresponding measurement device is designed to be placed on the collimated beam. As a result, it faces challenges when applied to large-size laser beams.

In this thesis, the technique of INSIGHT is employed. It operates effectively near the focal point, unrestricted by beam size. It is designed for reconstructing the complex electric field with a simple and compact setup. For comprehensive details on INSIGHT, including its operational principles, setup, and measurement results, refer to Chapter 6 where it is discussed in depth.

The study in Ref. [55] measured the spectrally-resolved wavefront to retrieve spatio-temporal coupling coefficients using an experimental setup that included various band-pass filters in front of a Shack-Hartmann wavefront sensor. However, this study only

presented the wavefront measurements for different wavelengths. Building upon this work, the transversal focal profiles and longitudinal focal shift are calculated from the measured spectrally-resolved wavefront and subsequently obtained the local intensity distribution at the focal plane. This approach was implemented to cross-verify the results obtained by INSIGHT.

1.4 Thesis Outline

This work focuses on designing a diagnostic system to tag the laser intensity shot-to-shot for the upcoming SFQED experiment LUXE at DESY with a precision of better than 1%.

Chapter 2 introduces the mathematical description of high-power ultrashort laser pulses in the temporal or spectral domain. In the spatial domain, it includes the propagation of a Gaussian beam and the wavefront in the transversal plane represented by Zernike polynomials. The chapter also discusses different types of spatial-temporal couplings, where the spatial characteristics of a laser pulse vary along with its temporal (or spectral) characteristics, which will decrease the peak intensity and make the intensity characterization more complicated. Additionally, the chirped-pulse-amplification technique and the JETi200 laser system are introduced at the Helmholtz Institute Jena used in the experiments in this thesis.

Chapter 3 examines the impact of laser beam propagation in vacuum over long distances, as required by the LUXE project, where the lab housing the laser system and diagnostic system is approximately 40 meters from the interaction point. Reconstructing a focal spot at the diagnostic table identical to the focal spot at the interaction point is necessary. Two different methods for relay-imaging the focal spot to the diagnostic system are explored and the results are compared.

Chapter 4 details the full diagnostics of laser focal spot intensity with high precision. The focal spot image is captured on-shot using a high-resolution imaging system and calculate the on-shot energy with high precision by measuring the near-field image and spectrum. Simultaneously, the pulse duration is measured using the SRSI technique. In addition to measuring the temporal profile of the main pulse, temporal intensity contrast over a longer time scale is also measured. Furthermore, the statistical behavior of the laser pulse parameters is analyzed to understand its stability.

In **chapter 5**, a non-linear intensity tagging method has been developed that tags the on-shot laser pulse intensity using a second-harmonic-generation (SHG) crystal.

Chapter 6 describes the three-dimensional measurement of the pulse by using the INSIGHT technology. The spectrally-resolved wavefronts are measured using a series of narrow band-pass filters in front of a wavefront sensor to verify the results of INSIGHT. This allows to deduce the longitudinal and transversal focal shifts across the spectrum and reconstruct the 3D focal spot.

Chapter 7 explores the application of the developed diagnostic methods to more complex situations, such as diagnosing Laguerre-Gaussian beams with orbital angular momentum (OAM) as well as the 3D characterization using INSIGHT. The factors contributing to the focal spot intensity distribution of such beams are analyzed and a method is developed to optimize this distribution using a wavefront mask composed of Zernike modes.

Chapter 8 draws the conclusion of the work presented in this thesis and presents the outlook on how the techniques developed will be applied in the LUXE experiment.

2 Theory

An ultrashort laser pulse is an electromagnetic wave packet with a temporal duration in the order of picosecond (10^{-12} s) or femtosecond (10^{-15} s). These pulses are typically characterized by their electric field $E(\mathbf{r}, t)$, which is a function of spatial coordinates \mathbf{r} and time t . The temporal variation of this electric field will be discussed in Section 2.1, as well as its corresponding Fourier-transformed spectral domain. The laser pulses in the spatial domain, both along the propagation direction and in the transversal plane perpendicular to the propagation, will be discussed in Sec. 2.2. However, it is not accurate to isolate $E(\mathbf{r})$ from $E(t)$. These two components are interdependent. A phenomenon known as spatial-temporal coupling (STC) will be discussed in Sec. 2.3. Finally, the high-power JETi200 laser system used for our experiment will be introduced in Sec. 4.2.

2.1 Ultrashort Laser Pulses in Temporal and Spectral Domains

This section draws extensively on the mathematical descriptions provided by [56].

2.1.1 Temporal-Domain Description of Ultrashort Laser Pulses

We first consider the temporal dependence of the electric field and neglect its spatial dependence. A complete description of the electric field of laser pulses can be given both in the temporal and frequency domains. These representations are interconnected through the Fourier transform, which allows us to switch between time and frequency descriptions.

In the temporal domain, the electric field of a pulse can be written as:

$$E(t) = A(t)e^{i[\phi(t)+\omega_0 t]} \quad (2.1)$$

where:

- t is the time.

- $A(t)$ is the envelope function, representing the slowly varying amplitude of the pulse.
- ω_0 is the central angular frequency of the pulse.
- $\phi(t)$ is the time-dependent phase, which can include effects such as chirp.

For practical purposes, the complex representation of the electric field is often used, in terms of its complex field envelope and a rapidly oscillating carrier wave:

$$E(t) = \text{Re} \left\{ \tilde{E}(t) e^{i\omega_0 t} \right\} \quad (2.2)$$

Here, $\tilde{E}(t)$ is the complex envelope of the electric field, containing both amplitude and phase information:

$$\tilde{E}(t) = A(t) e^{i\phi(t)} \quad (2.3)$$

2.1.2 Spectral-Domain Description of Ultrashort Laser Pulses

An ultrashort laser pulse can be treated as the superposition of a broad spectrum of monochromatic waves and its complex electric field in the spectral domain $E(\omega)$ is written as:

$$E(\omega) = A(\omega) e^{-i\varphi(\omega - \omega_0)} \quad (2.4)$$

where:

- $A(\omega)$ is the spectral envelope.
- ω is the angular frequency.
- ω_0 is the carrier frequency.
- $\varphi(\omega - \omega_0)$ is the spectral phase relative to the carrier frequency.

2.1.3 Fourier Transform Relationship

Temporally ultrashort pulses are generated in mode-locked lasers, where the spectral components constructively interfere with each other. Its electric field in the temporal domain $E(t)$ is yielded by the inverse Fourier transform of $E(\omega)$:

$$E(t) = \mathcal{F}^{-1}\{E(\omega)\} = \frac{1}{\sqrt{2\pi}} \int_0^{+\infty} E(\omega) \exp(-i\omega t) d\omega, \quad (2.5)$$

The integral over ω in Eq.2.5 begins from $\omega = 0$. It is often convenient to work with the complex electric field that contains only positive frequencies in the spectral domain and the negative components are neglected:

$$\tilde{E}^+(\omega) = \begin{cases} E(\omega) & \text{for } \omega \geq 0 \\ 0 & \text{for } \omega < 0 \end{cases}$$

The Fourier transform allows us to retrieve the spectral-domain electric field from its temporal representation:

$$E(\omega) = \mathcal{F}\{E(t)\} = \frac{1}{\sqrt{2\pi}} \int_{-\infty}^{+\infty} E(t)e^{-i\omega t} dt \quad (2.6)$$

These transforms allow us to analyze and manipulate the electric field in either domain, depending on the context of the problem.

2.1.4 Magnetic Field Description

To fully describe the electromagnetic laser field, we must also consider the magnetic field component. For light propagating in a vacuum, the magnetic field at any given time can be deduced from the electric field by examining the potentials related to the electromagnetic fields, as derived from Maxwell's equations. Through this method, both \mathbf{E} (electric field) and \mathbf{B} (magnetic field) can be expressed in terms of a vector potential \mathbf{A} for light in a vacuum in the absence of free charges. The electric field is given by:

$$\mathbf{E}(\mathbf{r}, t) = -\frac{\partial \mathbf{A}(\mathbf{r}, t)}{\partial t} \quad (2.7)$$

If we insert the ansatz for \mathbf{A} into the above equation, where:

$$\mathbf{A}(\mathbf{r}, t) = \mathbf{A}_0 \cos(\omega_0 t - \mathbf{k} \cdot \mathbf{r} + \phi) \quad (2.8)$$

The electric field becomes:

$$\mathbf{E}(\mathbf{r}, t) = \omega_0 \mathbf{A}_0 \sin(\omega_0 t - \mathbf{k} \cdot \mathbf{r} + \phi) \quad (2.9)$$

Similarly, the magnetic field can be expressed as:

$$\mathbf{B}(\mathbf{r}, t) = \nabla \times \mathbf{A}(\mathbf{r}, t) = \mathbf{k} \times \mathbf{A}_0 \sin(\omega_0 t - \mathbf{k} \cdot \mathbf{r} + \phi) \quad (2.10)$$

In this simple consideration, we find that:

$$|\mathbf{B}| = \frac{|\mathbf{k}|}{\omega_0} |\mathbf{E}| = \frac{|\mathbf{E}|}{c} \quad (2.11)$$

where c is the speed of light.

Here, \mathbf{B} is in phase with \mathbf{E} but oriented perpendicularly.

2.1.5 Intensity

In a vacuum, the Poynting vector \mathbf{S} represents the instantaneous energy flux density and has units of intensity (W/cm^2). It gives the power density carried by an electromagnetic wave and the direction in which power is carried.:

$$\mathbf{S} = \frac{1}{\mu_0} (\mathbf{E} \times \mathbf{B}) \quad (2.12)$$

Since \mathbf{E} and \mathbf{B} are in phase, \mathbf{S} oscillates rapidly between 0 and $\epsilon_0 c E_0^2$ with ϵ_0 the vacuum permittivity, representing the instantaneous energy density. Due to this oscillatory nature, \mathbf{S} is challenging to measure directly. The temporal average of \mathbf{S} is termed the laser intensity, $I(t) = \langle \mathbf{S} \rangle$, a commonly accessible experimental quantity. The intensity $I(t)$ can be formulated in terms of either \mathbf{E} or \mathbf{B} :

$$I(t) = \langle \mathbf{S}(t) \rangle = \epsilon_0 c^2 \langle \mathbf{E}(t) \times \mathbf{B}(t) \rangle = \epsilon_0 c \langle \mathbf{E}^2(t) \rangle = \epsilon_0 c \langle \mathbf{B}^2(t) \rangle \quad (2.13)$$

The slow-varying envelope approximation (SVEA) separates the wave's fast oscillating carrier from its slowly varying envelope. By employing SVEA and executing the temporal average, the result gives:

$$I(t) = \frac{\epsilon_0 c}{2} \langle E_0(t)^2 \rangle = \frac{\epsilon_0 c^3}{2} \langle B_0(t)^2 \rangle \quad (2.14)$$

The temporal pulse duration τ is defined as the full width at half maximum (FWHM) of $I(t)$.

The spectral intensity function is defined by:

$$I(\omega) = \frac{1}{2} \epsilon_0 c n |E(\omega)|^2 \quad (2.15)$$

where n is the refractive index. The spectral bandwidth $\Delta\omega$ is defined as the FWHM of $I(\omega)$.

2.1.6 Gaussian Pulse Example

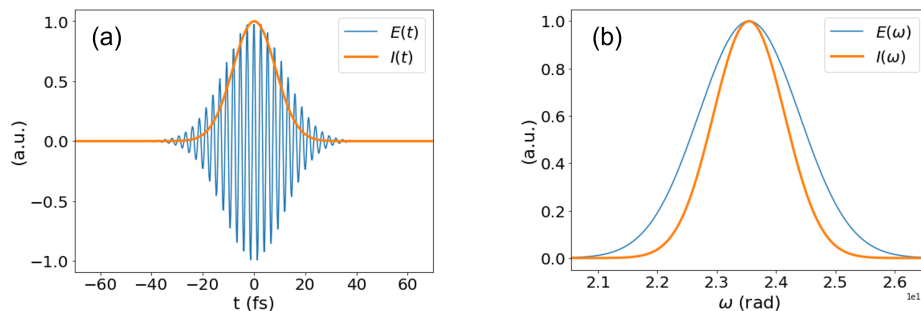


Figure 2.1: The electric field and intensity envelope of a Gaussian ultrashort laser pulse in (a) the temporal domain and (b) the spectral domain. $E(\omega)$ and $E(t)$ can be converted to each other by Fourier transform and inverse Fourier transform.

Consider a Gaussian pulse with a normalized peak value, as shown in Fig.2.1(a), mathematically described by:

$$E(t) = \exp\left(-\frac{4\ln 2 t^2}{\tau^2}\right) \exp(-i\omega_0 t) \quad (2.16)$$

where τ is the FWHM pulse duration. The spectral field, obtained by Fourier transformation, as shown in Fig.2.1(b), is:

$$E(\omega) = \sigma \sqrt{2\pi} \exp\left(-\frac{\sigma^2}{2} (\omega - \omega_0)^2\right) \quad (2.17)$$

where σ is the standard deviation:

$$\sigma = \frac{\tau}{2\sqrt{2\ln 2}} \quad (2.18)$$

This corresponds to a Gaussian spectrum centered at ω_0 . The temporal intensity,

which is the square of the modulus of the temporal field, is:

$$I(t) = \exp\left(-8\ln 2 \frac{(t - t_0)^2}{\tau^2}\right) \quad (2.19)$$

In the spectral domain, the spectral intensity is:

$$I(\omega) = \exp\left(-\sigma^2(\omega - \omega_0)^2\right) \quad (2.20)$$

and the FWHM spectral width is:

$$\Delta\omega = \frac{2\sqrt{2}}{\sqrt{\ln 2}\sigma} \quad (2.21)$$

Temporal duration and spectral bandwidth are related by $\tau\Delta\omega = 4\ln 2$. This equality holds only for Gaussian pulses, which are Fourier transform-limited.

2.1.7 Temporal and Spectral Phase

A laser pulse whose spectral phase is relatively constant across the spectrum is phase-locked to achieve the shortest pulse duration, which is known as Fourier limited. However, dispersion happens when it propagates in a dispersive medium, for example, glass. The refractive index of a medium is defined as the ratio between the speed of light c and the phase velocity ν_p :

$$n(\omega) = c/\nu_p, \quad (2.22)$$

where ν_p is the velocity of the phase of a spectral component related to the wave number k , written as:

$$\nu_p = \frac{\omega}{k}. \quad (2.23)$$

For a laser pulse, its velocity is described by the overall envelope velocity, known as the group velocity ν_g , written as:

$$\nu_g = \frac{\partial\omega}{\partial k}. \quad (2.24)$$

With the frequency-dependent refractive indices, different spectral components in the broad spectrum travel with different velocities and experience different optical path lengths. As a result, the pulse envelope deforms and its velocity is also changed.

Such deformation is characterized as group velocity dispersion (GVD) β_2 , which is the derivative of the inverse ν_g to ω :

$$\beta_2 = \frac{\partial}{\partial \omega} \frac{1}{\nu_g} \quad (2.25)$$

As a pulse travels through a dispersive medium, the GVD induces a chirp on the pulse. Then the temporal phase $\phi(t)$ in Eq.2.5 of a chirped pulse contains a quadratic term $bt^2/2$, which implies a linear change of frequency in time. The instant frequency $\omega(t)$ is the derivative of $\phi(t)$ to t and it gives:

$$\omega(t) = \omega_0 + \frac{d}{dt}\phi(t) \quad (2.26)$$

With a positive GVD ($\beta_2 > 0$), also known as positive chirp, the higher frequency

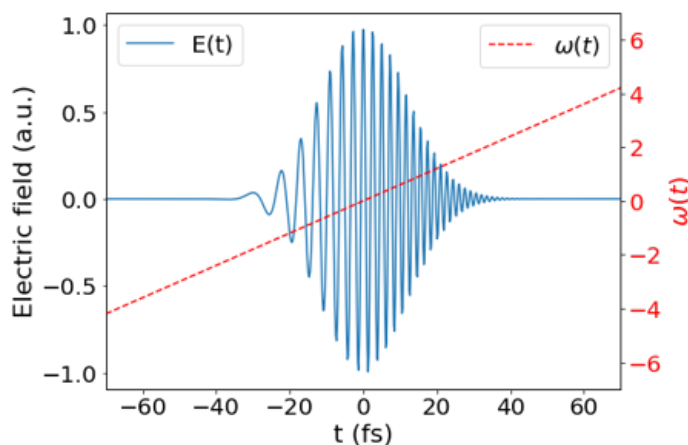


Figure 2.2: Electric field of a positively chirped pulse, where the instantaneous frequency grows with time. This pulse is obtained by adding 600 fs^{-2} to $\phi(t)$ of the pulse in Fig.2.1(a).

components in the spectrum travel with larger group velocities than the lower ones, where the leading edge arrives earlier than the trailing edge, as illustrated in Fig. With a negative chirp ($\beta_2 < 0$), the instant frequency decreases with time and the higher frequency components travel with smaller group velocity.

The dispersion in the spectral domain can be described by rewriting the spectral phase $\varphi(\omega - \omega_0)$ in Eq. 2.4 into the form of Taylor expansion:

$$\varphi(\omega) = \sum_{n=0}^{\infty} \frac{(\omega - \omega_0)^n}{n!} D_n, \quad (2.27)$$

where D_n is called the dispersion coefficient, which is the derivative of $\varphi(\omega)$ with respect to ω evaluated at ω_0 :

$$D_n = \left(\frac{\partial^n \varphi(\omega)}{\partial \omega^n} \right)_{\omega=\omega_0}. \quad (2.28)$$

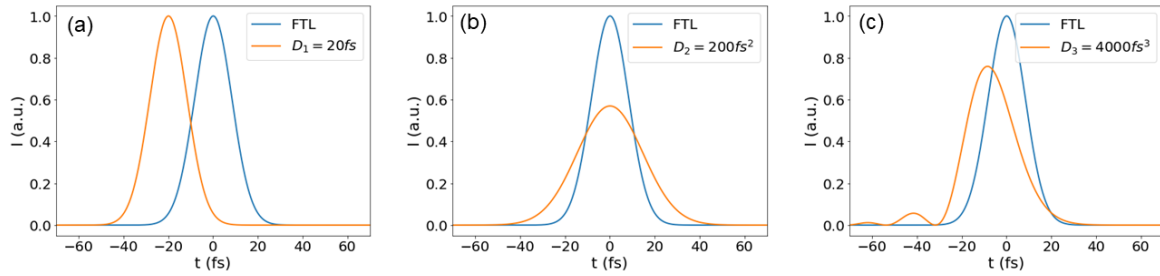


Figure 2.3: (a)-(c) are the intensity distribution of ultrashort laser pulses in the time domain with different spectral phase profiles added to the pulse in Fig.2.1(a). The pulse labeled with FTL is the Fourier transform limit with $\varphi(\omega) = 0$. In (a), the pulse shape does not change but is shifted by $20 fs$ with $D_1 = 20 fs$. The pulse plotted in (b) is obtained by adding a chirp of $D_2 = 200 fs^2$. And the pulse in (c) is with a dispersion of $D_3 = 4000 fs^3$.

The Fourier transform limited pulse has the shortest duration where the spectral phase $\varphi(\omega)$ is constant across ω . The absolute term D_0 changes the carrier phase but is only significant for few-cycle pulses. The first term D_1 , named group delay (GD), is the linear spectral phase corresponding to the shift in time, as illustrated in Fig.2.3 (a). The GD per unit length yields the inverse group velocity, $1/\nu_g$. D_2 , the pulse group delay dispersion (GDD), broadens the temporal profile and decreases the peak intensity, as shown in Fig.2.3 (b). GDD per unit length gives the GVD. D_3 is the third-order dispersion (TOD), which decreases the peak intensity and lifts the side lobes asymmetrically, as plotted in Fig.2.3(c).

2.2 Laser Pulses in the Spatial Domain

In the preceding section, the characterization of ultrashort laser pulses in both the temporal and spectral domains has been introduced. Now this section focuses on the spatial domain, including the propagation along z-axis and the behavior in the transverse plane. This section draws extensively on the mathematical descriptions

provided by [57].

2.2.1 Near-Field Diffraction

The description of light propagation in free space and through various optical systems can use Fourier optics and harmonic analysis by decomposing arbitrary wavefronts into harmonic components.

An arbitrary function in a plane can be represented as a sum of harmonic functions, as the concept of Fourier transform, each characterized by specific spatial frequencies and complex amplitudes. A plane wave $U(x, y, z)$ propagating in the z -direction can be described as:

$$U(x, y, z) = A \exp[-i(k_x x + k_y y + k_z z)] \quad (2.29)$$

where A is the complex amplitude, and k_x , k_y , and k_z are the components of the wavevector \mathbf{k} . The wavevector components are related by:

$$k_z = (k^2 - k_x^2 - k_y^2)^{1/2} \quad (2.30)$$

Near-field diffraction, or Fresnel diffraction, occurs when the observation distance from the diffracting aperture is relatively short. It provides a detailed understanding of how light waves propagate and form diffraction patterns in the near-field regime. In this regime, the curvature of the wavefront and the varying distances from different points on the aperture to the observation plane significantly affect the diffraction pattern.

In the near-field, the complex amplitude $U(x, y, z)$ of a wavefront can be described using the Fresnel approximation. The Fresnel diffraction integral, which accounts for the quadratic phase terms due to the curvature of the wavefront, is given by:

$$U(x, y, z) \propto \frac{1}{i\lambda z} \iint_{-\infty}^{\infty} U_0(x', y') \exp\left[i\frac{\pi}{\lambda z} \left((x - x')^2 + (y - y')^2\right)\right] dx' dy' \quad (2.31)$$

Here, $U_0(x', y')$ represents the complex amplitude at the aperture plane ($z = 0$), and λ is the wavelength of light. This integral accounts for the varying phase shifts introduced by the different path lengths from points on the aperture to the observation point.

The Fresnel number F is a dimensionless parameter that characterizes the near-field diffraction regime:

$$F = \frac{a^2}{L\lambda} \quad (2.32)$$

where a is the characteristic size of the aperture, L is the distance to the observation screen, and λ is the wavelength of light. Fresnel diffraction is significant when $F \gg 1$.

2.2.2 Far-Field Diffraction

Far-field diffraction, also known as Fraunhofer diffraction, occurs when the observation distance from an aperture is significantly larger than the dimensions of the aperture and the wavelength of light. It can also describe the focal plane of a complex amplitude transformed by a focusing optical element. In this regime, the diffraction pattern depends primarily on the angles at which light propagates, rather than the distances. The far-field diffraction pattern can be obtained using the Fourier transform of the aperture function, which translates the spatial distribution of the aperture into an angular distribution in the far field.

When the propagation distance L is sufficiently large, the complex amplitude $U(x, y, L)$ at the output plane can be expressed as:

$$U(x, y, L) = h_0 \tilde{U} \left(\frac{x'}{\lambda L}, \frac{y'}{\lambda L} \right) \quad (2.33)$$

Here, $\tilde{U}(\nu_{x'}, \nu_{y'})$ is the Fourier transform of $U(x', y')$ at $z=0$, with the spatial frequencies $\nu_{x'} = \frac{x'}{\lambda L}$ and $\nu_{y'} = \frac{y'}{\lambda L}$, and $h_0 = \frac{i}{\lambda L} \exp(-ikL)$.

A focusing optics such as a lens transforms a plane wave into a paraboloidal wave focused to a point in the focal plane, with small incident angles of θ_x and θ_y and a focal length of f . The complex amplitude $U(x, y, L)$ at point (x, y) at $z=L$ is proportional to the Fourier transform of $U(x', y')$ with $\nu_{x'} = \frac{x'}{\lambda f}$ and $\nu_{y'} = \frac{y'}{\lambda f}$.

At the focal plane with $L = f$:

$$U(x, y, f) = h_f \tilde{U} \left(\frac{x'}{\lambda f}, \frac{y'}{\lambda f} \right) \quad (2.34)$$

where $h_f = \frac{i}{\lambda f} \exp(-ikf)$. When $L \neq f$:

$$U(x, y, L) = h_l \exp \left[i\pi \frac{(x^2 + y^2)(L - f)}{\lambda f^2} \right] \tilde{U} \left(\frac{x'}{\lambda f}, \frac{y'}{\lambda f} \right) \quad (2.35)$$

where $h_l = \frac{i}{\lambda f} \exp[-ik(L)]$.

2.2.3 Gaussian Beam Propagation

The Gaussian beam propagating in the direction of the z-axis in vacuum or in free space can be mathematically described in a cylindrical coordinate, and its electric field can be expressed as:

$$E(r, z) = E_0 \frac{w_0}{w(z)} \exp\left[-\frac{r^2}{w(z)^2}\right] \exp\left(i\left[kz - \arctan\left(\frac{z}{z_R}\right) + \frac{kr^2}{2R(z)}\right]\right) \quad (2.36)$$

where

- r is the radius from the z-axis;
- E_0 is the peak electric field at the beam center;
- w_0 is the radius of the beam waist;
- $w(z)$ is the radius where the intensity drops to $1/e^2$ of the peak intensity I_0 at z , (or where the electric field drops to $1/e$ of E_0), written as:

$$w(z) = w_0 \sqrt{1 + \left(\frac{\lambda z}{\pi w_0^2}\right)^2} \quad (2.37)$$

- z is the distance from the beam waist in the direction of propagation;
- k is the wave number for λ ;
- $R(z) = z + z_R^2/z$ is the wavefront radius curvature;
- Z_R , the Rayleigh length as shown in Fig.2.4, is a distance in z direction where the cross-section area of the beam becomes double that at the beam waist, which is written as:

$$z_R = \frac{\pi w_0^2}{\lambda} \quad (2.38)$$

and the beam radius w_R at the Rayleigh length equals $\sqrt{2}w_0$ by definition.

As shown in Fig.2.4, the beam waist w_0 is the minimum value when the beam is at a diffraction limit. In an optical system where a lens or an equivalent optics is used to

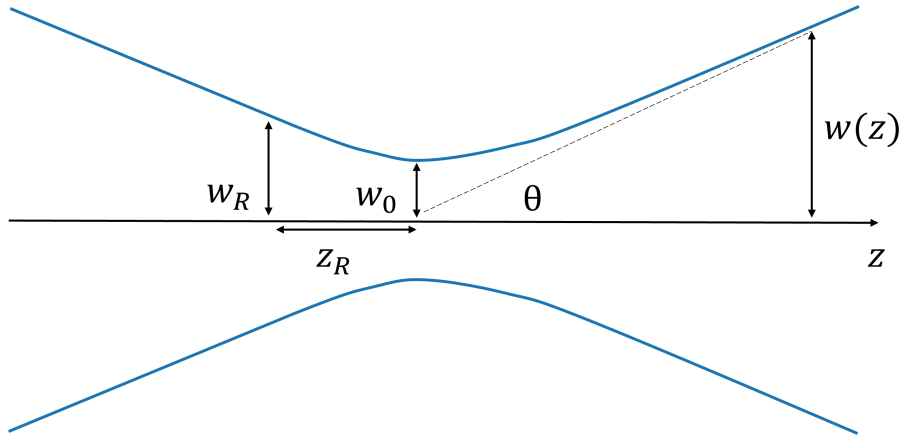


Figure 2.4: The scheme of a Gaussian beam propagating in the z-direction

focus a laser beam, the beam waist at focus is obtained by:

$$w_0 = \frac{1.22\lambda f}{\pi D} \quad (2.39)$$

where f is the focal length and D is the diameter of the effective aperture. The f-number is an index defined as f/D . Then the beam diverges at a divergence angle θ :

$$\theta = \frac{\lambda}{\pi w_0}. \quad (2.40)$$

Panel A in Fig.2.5 depicts a typical example of a beam with Gaussian intensity

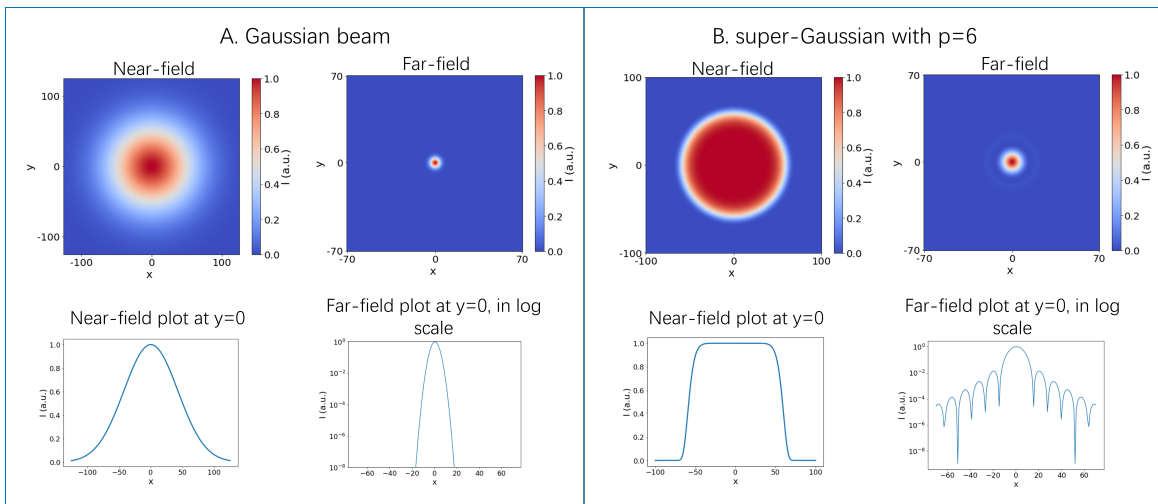


Figure 2.5: Block A: The near-field and far-field intensity distribution of a beam with Gaussian distribution in the transverse plane, and their respective plot along the x-axis in 1D. Block B: The NF and FF of a super-Gaussian beam with p=6 and their respective plots in 1D.

distribution in the transversal plane of the near field and its corresponding far field that also follows the Gaussian distribution. The intensity distribution in the transversal plane can be expressed in a polar coordinate as:

$$I(r) = I_0 \exp\left(\frac{-2r^2}{w(z)^2}\right) \quad (2.41)$$

where I_0 is the intensity of the peak maximum.

2.2.4 Non-Gaussian Beams

In another case, the beam profile in the transversal direction can have a super-Gaussian distribution or an approximate top-hat distribution, with the intensity distribution in the transversal direction of order p written as:

$$I(r) = I_0 \exp\left[-2\left(\frac{r^2}{w^2}\right)^p\right] \quad (2.42)$$

Panel B in Fig.2.5 shows an example with $p = 6$ of the near-field, as it is close to the approximation of the real beam and the corresponding far-field profile with a flat wavefront. The far field is obtained from the near field by the 2-dimensional Fourier transform and its intensity variation in angle φ is expressed as:

$$I(\theta) = I_0 \left[\frac{2J_1(kr \sin\varphi)}{kr \sin\varphi}\right]^2 \quad (2.43)$$

where k is the spatial angular frequency expressed as $k = 2\pi/\lambda$, and J_1 is the Bessel function of the first kind of order one.

The Airy size is the radius of the first dark ring, which is the distance from the central peak to the first local minimum.

$$\sin(\theta) = 1.22 \frac{\lambda}{D} \quad (2.44)$$

The radius is then given as:

$$r = 1.22\lambda f/D \quad (2.45)$$

The energy encircled within the first dark ring contains 84% of the total energy, and the first sidelobe has an intensity of 1.7% of the central maximum.

Several methods are available for defining laser beam size, with the full width at half

maximum (FWHM) and the $1/e^2$ beam size being the most prevalent. These methods are particularly effective for beams with well-defined profiles, like those following a Gaussian distribution, where the beam diameter is determined at the point where intensity falls to half its maximum or $1/e^2$ of the peak intensity, respectively. However, for beams with arbitrary profiles that do not conform neatly to Gaussian distributions, a more comprehensive approach is needed to capture information beyond the central part of the beam. This is where the $D4\sigma$ method comes into play. $D4\sigma$, as the ISO international standard of beam size characterization[58], defines beam size as four times σ , the standard deviation of the intensity distribution across the beam. This method provides a more inclusive measurement by considering the entire beam profile, particularly useful for arbitrary beams. The standard deviation σ_x along the x-axis is calculated using the formula:

$$\sigma_x^2 = \frac{\int_x \int_y (x - \bar{x})^2 I(x, y) dx dy}{\int_x \int_y I(x, y) dx dy} \quad (2.46)$$

where \bar{x} is the beam's center of mass on the x-axis, determined by:

$$\bar{x} = \frac{\int_x \int_y x I(x, y) dx dy}{\int_x \int_y I(x, y) dx dy} \quad (2.47)$$

As a result, $D4\sigma_x = 4\sigma_x$, with an analogous process applied to determine $D4\sigma_y$ along the y-axis. This methodology proves particularly valuable for assessing beam divergence along the propagation axis of non-diffraction-limited beams characterized by a specific M^2 factor. The M^2 factor, indicating beam quality, equals 1 for an ideal Gaussian beam and exceeds 1 for beams with non-Gaussian or arbitrary profiles. It is defined as:

$$M^2 = \frac{\pi\theta w_0}{\lambda} \quad (2.48)$$

where θ is the half divergence angle and w_0 is the minimum beam radius of the real beam. This factor is crucial for evaluating the extent to which a beam deviates from the ideal Gaussian profile, offering insights into beam quality and propagation characteristics.

Furthermore, by definition, the Rayleigh length z_R becomes:

$$z_R = \frac{\pi w_0^2}{\lambda M^2} \quad (2.49)$$

2.2.5 Laguerre-Gaussian Beams

The transverse mode of a laser pulse refers to the spatial mode of the pulse in the plane perpendicular to its propagation direction. This mode can be described as a product of a Gaussian profile and a Laguerre polynomial, forming a Laguerre-Gaussian (LG) beam. The electric field of a point (r, φ) on an LG beam in polar coordinates, with r the radial distance and φ the azimuthal angle, is written as:

$$E_{pl}(\rho, \varphi) \propto \sqrt{I_0} \rho^{l/2} [L_p^l(\rho)] e^{il\varphi} e^{-\rho/2}, \quad (2.50)$$

where $\rho = 2r^2/w^2$, with w the radius at which the intensity drops to $1/e^2$ of its maximum value. L_p^l is the Laguerre polynomial of radial order p and azimuthal index l . A beam with Gaussian intensity distribution corresponds to the fundamental mode of an LG beam with $p = 0$ and $l = 0$.

For higher orders, in the work by Allen *et al.*[59], LG beams were shown to carry orbital angular momentum (OAM) along their propagation axis. This certain type of laser mode contains the azimuthal phase variation of the wavefront, characterized by the non-zero topological charge l . Its far-field intensity profile is ring-shaped, featuring a hollow central core. Various methods have been proposed to generate an LG beam carrying OAM. It can be achieved through computer-generated holograms[60], segmented deformable mirrors[61], and a variety of spiral phase plates (SPPs), such as SPP made of liquid crystals[62] and those fabricated by the method of electron beam lithography on polymethylmethacrylate layers over glass substrates[63, 64]. An SPP is an optical element that introduces an azimuthal dependence, $l\varphi$, with φ representing the azimuthal angle, to the electric field of the laser, transforming a flat wavefront into a helix. Though ideal SPPs exhibit continuous azimuthal phase variations, fabrication complexities lead to multi-step decompositions. For instance, an $l = 1$ SPP comprises 16 steps with a phase gap of 2π at the central wavelength λ_0 , as depicted in Fig.2.6. The figure also illustrates the Poynting vector of a beam transmitting through such a phase plate and the corresponding far-field intensity profile in the shape of a doughnut.

Laser beams carrying OAM have applications in various fields of science and technology, such as optical manipulation, where LG beams enable precise control of motions of micro-particles in optical tweezers by transferring the OAM to trapped particles [65], and in microscopy, where LG beams are employed in stimulated-emission deple-

tion (STED) microscopy to enhance the resolution to scales of 30-80 nm [66], and in the field of particle acceleration, where structured wakefields can be generated using OAM-carrying laser beams to accelerate positrons [67] and ring-shaped electron beams [68]. In the experiments utilizing the JETi200 laser, the vortex focus is generated for the application of laser guiding in plasma [69].

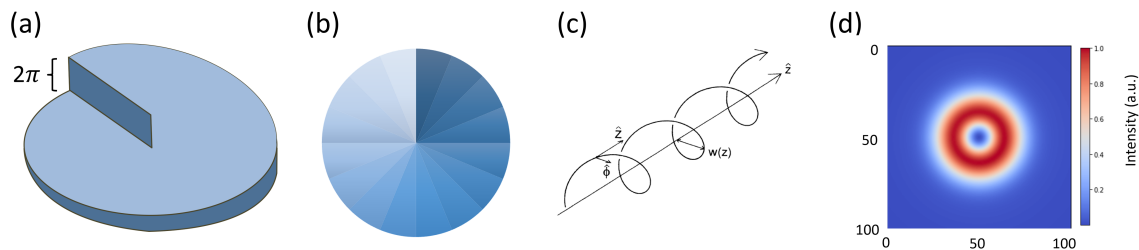


Figure 2.6: (a) a scheme of an ideal spiral phase plate with a phase gap of 2π ($l = 1$) and (b) the top view of the phase plate exhibits the gradient of the phase gap in 16 discrete steps. (c) the Poynting vector of a linearly polarized Laguerre-Gaussian laser beam with orbital angular momentum[59]. (d) an ideal far-field intensity profile of a Gaussian beam transmitted through a spiral phase plate with $l = 1$.

2.2.6 Zernike Polynomials

The far-field figures in Fig.2.5 are obtained by taking the Fourier transform of each respective near field with a flat wavefront. The wavefront of a laser beam can be distorted due to various factors such as the imperfect surfaces or inhomogeneous materials of the optics. These wavefront distortions can be decomposed into a sum of the Zernike polynomials Z_n^m . These polynomials are a series of orthogonal functions on a unit disk, used to characterize the aberrations of the wavefront of the laser beam, which are written as [70]:

$$Z_{even,n}^m(r, \varphi) = \sqrt{n+1} R_n^m(r) \sqrt{2} \cos(m\varphi), \quad (2.51)$$

$$Z_{odd,n}^{-m}(r, \varphi) = \sqrt{n+1} R_n^m(r) \sqrt{2} \sin(m\varphi), \quad (2.52)$$

where φ is the azimuthal angle, n and m are the integers with $n \geq m \geq 0$, r the radial distance, and $R_n^m(r)$ the radial polynomials expressed as:

$$R_n^m(r) = \sum_{k=0}^{n-m} \frac{(-1)^k (n-k)!}{k! \binom{n+m}{2-k}! \binom{n-m}{2-k}!} r^{n-2k}. \quad (2.53)$$

Each Zernike polynomial corresponds to a specific type of aberration. The mathematical expressions of the six most commonly used polynomials and their corresponding names are listed below:

oblique astigmatism (45°)

$$Z_2^{-2} = \sqrt{6} r^2 \sin 2\varphi; \quad (2.54)$$

vertical astigmatism (0°)

$$Z_2^2 = \sqrt{6} r^2 \cos 2\varphi; \quad (2.55)$$

vertical coma (Y)

$$Z_3^{-1} = \sqrt{8} (3r^3 - 2r) \sin \varphi; \quad (2.56)$$

horizontal coma (X)

$$Z_3^1 = \sqrt{8} (3r^3 - 2r) \cos \varphi; \quad (2.57)$$

vertical trefoil (0°)

$$Z_3^{-3} = \sqrt{8} r^3 \sin 3\varphi; \quad (2.58)$$

oblique trefoil (30°)

$$Z_3^3 = \sqrt{8} r^3 \cos 3\varphi. \quad (2.59)$$

Astigmatism is presented when the focal lengths are different in the two orthogonal coordinates in the transverse plane, x and y , resulting in different divergence and radii in the two directions. Coma aberration describes the wavefront with a tilted plane and the trefoils describe the wavefront with a three-fold rotational symmetry.

Fig.2.7 illustrates the phase patterns of a flat wavefront and the six Zernike polynomials. When these phase masks are applied to a beam with perfect Gaussian intensity distribution, the resulting intensity distribution patterns can be seen in Fig.2.8. Furthermore, numerical calculations were performed to investigate the effects of these Zernike aberrations on beams with OAM, and the results are shown in Fig.2.9. These findings demonstrate the impact of Zernike aberrations on beams with OAM, which have applications in fine-tuning the doughnut-shaped focus profile for the structured LWFA experiments.

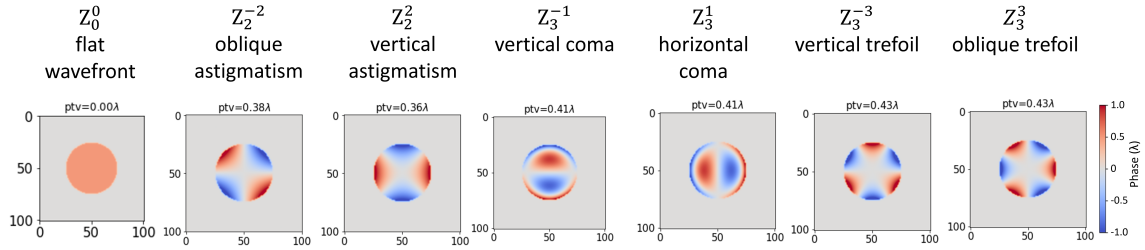


Figure 2.7: The flat wavefront (Z_0^0) and the 6 higher-order Zernike phase masks.

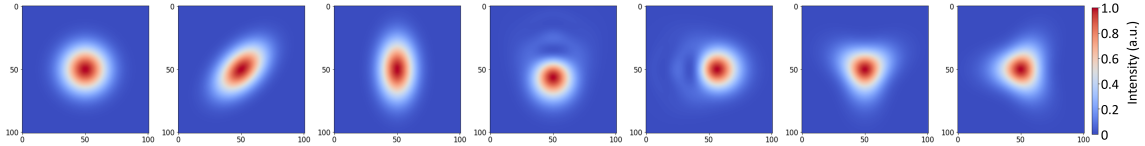


Figure 2.8: The Gaussian intensity distribution with flat wavefront and the 6 Zernike phase masks applied respectively.

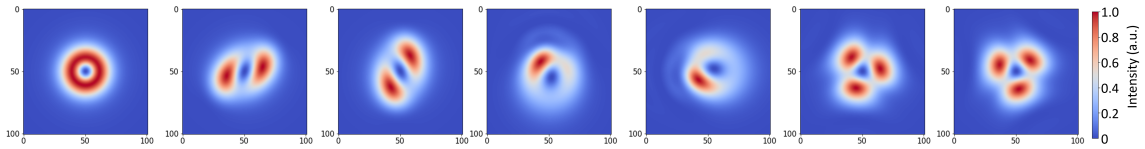


Figure 2.9: The doughnut-shaped focal spot of a laser beam with OAM and the extra Zernike phase masks applied respectively.

The Zernike aberrations of the wavefront can be corrected by measuring the wavefront distortion using a wavefront sensor, and then applying a corrective phase using a deformable mirror.

The Strehl ratio, denoted as S , quantifies the intensity degradation due to wavefront aberrations and is calculated using the formula [71]

$$S = \exp \left[-(2\pi\sigma_{WF})^2 \right] \quad (2.60)$$

where σ_{WF} is the RMS value of the wavefront aberrations. This ratio is the actual beam intensity relative to an ideal aberration-free beam.

The Q-factor evaluates the quality of a two-dimensional focal spot by quantifying the energy concentration within the FWHM of the focal spot relative to the total energy of the beam. It can be acquired by:

$$Q = \frac{\iint_0^r I(x, y) dx dy}{\iint_0^\infty I(x, y) dx dy} \quad (2.61)$$

where r is the radius of FWHM. A high Q-factor indicates that the beam's energy is well-concentrated within the FWHM, resulting in a more consistent and intense focal spot with minimal fluctuations. Conversely, the presence of wavefront aberrations causes the focal spot to deviate from an ideal focus with a spread of energy over a larger area, resulting in a decrease in the Q-factor. A low Q-factor indicates greater variations in the focal spot shape and intensity fluctuations. By reducing the complexity of 2D focal spot analysis to a single scalar value, the Q-factor simplifies the assessment of beam quality. For example, the Q-factor for the far field of the Gaussian beam in Fig.2.5 is calculated to be 50%, while it is 48% for the far field of the Super-Gaussian beam.

2.3 Spatial-Temporal Couplings

The electric field of an ultrashort laser pulse is typically expressed as the product of its temporal and spatial components, denoted as $E(\mathbf{r}, t) = E(\mathbf{r})E(t)$. This expression separates the pulse temporal profile from its spatial electric field. However, it is important to note that these two terms exhibit interdependence on each other, referred to as spatial-temporal couplings (STC), and treating them separately leads to inaccuracies.

STCs arise in ultrashort laser pulses due to their broad spectrum. This happens when the spectral components of the pulse travel at different velocities and in different directions after being diffracted by dispersive optics, such as gratings and prisms, or refracted by lenses. Spatial-temporal distortions can be intentionally introduced by the gratings or prisms in the pulse compressors, which can be corrected by careful alignment of the compressors. However, residual STCs may still persist. Additionally, STCs can occur unintentionally in the laser system, such as when the ultrashort laser pulse transmits through a tilted substrate or a singlet lens. Four primary types of STCs need to be considered, namely angular dispersion (AD), spatial dispersion (SD), pulse-front tilt (PFT), and 'time versus angle'. Although these four STCs exist in different domains, they are interrelated to each other through Fourier transformation [72].

Angular dispersion occurs in the k - ω domain, where k represents spatial frequency, and ω represents angular frequency. It is introduced by angularly dispersive optics

such as gratings in pulse compressors, where the propagation directions of each spectral component are different, denoted as $d\varepsilon/d\lambda$, with ε the angle from the AD optics. It can be optimized by proper alignment of the gratings in the compressor.

Spatial dispersion occurs in the x - ω domain, where x is the transverse coordinate. This describes a situation where different color components are spatially separated, rather than the centroid point of beams at each wavelength overlapping. Overall the pulse is spatially stretched or compressed and the pulse temporal profile differs across the transversal plane. Furthermore, the research also shows that spatially chirped pulse does not stay collimated as the undistorted beam [73]. The Gaussian pulse in the x - ω domain with spatial dispersion ζ can be expressed as:

$$E(x, \omega) = E_0(\omega, x - \zeta\omega) = E_0 \exp \left[- \left(\frac{\omega}{\Delta\omega} \right)^2 \right] \exp \left[- \left(\frac{x - \zeta\omega}{\Delta x} \right)^2 \right]. \quad (2.62)$$

Pulse-front tilt is a phenomenon in the x - t domain where different parts of the pulse travel at different velocities, causing the leading edge of the pulse to tilt in the time domain. This can lead to pulse stretching and distortion. It can be described as $E(x, t) \propto E_0(x, x - \gamma t)$, with γ the coefficient of couplings. PFT is often the result of AD and SD, but it can also arise from the simultaneous presence of spatial and temporal chirp in the absence of AD. Specifically, as explained in Ref.[74], a Fourier-transform limited, spatially chirped pulse, transmitted through a thick dispersive medium, causes the redder components to travel faster than the bluer side, resulting in PFT.

'Time versus angle', also known as the 'ultrafast lighthouse effect'[75], a STC phenomenon in the k - t domain, describes the pulse amplitude propagation direction change as a function of time.

As a result of the presence of STCs, the focal spot exhibits a longitudinal focal shift, where the best focus of each wavelength shifts along the propagation direction (z -axis). This shift causes different wavelengths to reach their minimum focal spot size at different positions along the propagation axis, as shown in Fig.2.10(a). The propagation direction varies for each wavelength due to the angular dispersion introduced by the grating or prism. At the best focal plane, where the spectrally integrated focal spot size is at its minimum, the focal spots of different wavelengths exhibit varying diameters, as shown in Fig.2.10(b). This variation in spot size is due to the differing diffraction limits and longitudinal focal shifts of each wavelength. Additionally, the

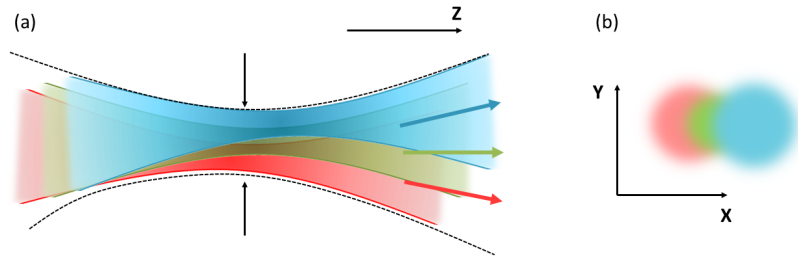


Figure 2.10: (a) Illustration of the longitudinal focal shift and varying propagation directions caused by STC. Different wavelengths (red, green, and blue) focus at different points along z-axis, leading to varying focal spot sizes. The dotted lines represent the envelope of the beam's propagation. (b) At the best focal plane, the focal spots of different wavelengths exhibit different diameters, and the centroid positions are shifted in the transversal plane.

centroid of each focal spot drifts in the transversal direction (x and y axes), causing a spatial separation between the focal spots of different wavelengths. This centroid drift further reduces the peak intensity of the integrated focal spot, as the energy is spread out over a larger area.

The presence of STCs alters the pulse spatial and temporal configurations, consequently significantly reduces the peak intensity of the laser pulse. The classical method to determine the laser pulse intensity I is to calculate it using the equation:

$$I = \frac{E}{\tau A} \quad (2.63)$$

by measuring the pulse total energy E , the focus spot area A , and the temporal duration τ individually. However, it is only valid assuming no effects from STCs. The real situation is more complicated. The three-dimensional reconstruction of the complete complex electric field $E(x, y, \omega)$ is introduced in Chapter 6, with the measurements of STCs and their resulting effects on the focal spot.

2.4 Second Harmonic Generation

Second Harmonic Generation (SHG) is a nonlinear optical process where two photons of the same frequency interacting with a nonlinear material are combined to form a new photon with twice the frequency (and half the wavelength) of the original photons.

Maxwell's equations in the absence of free charges and currents in an isotropic space are:

$$\nabla \cdot \mathbf{E} = 0, \quad (2.64)$$

$$\nabla \cdot \mathbf{B} = 0, \quad (2.65)$$

$$\nabla \times \mathbf{E} = -\frac{\partial \mathbf{B}}{\partial t}, \quad (2.66)$$

$$\nabla \times \mathbf{B} = \mu_0 \epsilon_0 \frac{\partial \mathbf{E}}{\partial t}. \quad (2.67)$$

$$(2.68)$$

In nonlinear optics, the polarization \mathbf{P} of a medium is not linearly proportional to the electric field \mathbf{E} . Instead, it can be expanded as a power series in \mathbf{E} :

$$\mathbf{P} = \epsilon_0 \left(\chi^{(1)} \mathbf{E} + \chi^{(2)} \mathbf{E}^2 + \chi^{(3)} \mathbf{E}^3 + \dots \right), \quad (2.69)$$

where $\chi^{(1)}$ is the linear susceptibility, and $\chi^{(2)}$ and $\chi^{(3)}$ are the second- and third-order nonlinear susceptibilities, respectively. The wave equation for the electric field in a nonlinear medium can be derived from Maxwell's equations by using $\mathbf{D} = \epsilon_0 \mathbf{E} + \mathbf{P}$. The following equation can be obtained:

$$\nabla \times (\nabla \times \mathbf{E}) = -\mu_0 \frac{\partial^2 \mathbf{D}}{\partial t^2} \quad (2.70)$$

Assuming $\nabla \cdot \mathbf{E} = 0$ and using the vector identity $\nabla \times (\nabla \times \mathbf{E}) = \nabla(\nabla \cdot \mathbf{E}) - \nabla^2 \mathbf{E}$, it can be written as:

$$\nabla^2 \mathbf{E} - \mu_0 \epsilon_0 \frac{\partial^2 \mathbf{E}}{\partial t^2} = \mu_0 \frac{\partial^2 \mathbf{P}}{\partial t^2} \quad (2.71)$$

By considering a second-order nonlinearity, which leads to three-wave mixing, the nonlinear polarization is:

$$\mathbf{P}^{(2)} = \epsilon_0 \chi^{(2)} \mathbf{E}^2 \quad (2.72)$$

The total field \mathbf{E} is written as the sum of the two-color incident field, consisting of two components E_1 and E_2 at angular frequencies ω_1 and ω_2 respectively:

$$\mathbf{E} = \frac{1}{2} E_1 e^{-i\omega_1 t} + \frac{1}{2} E_2 e^{-i2\omega_2 t} + c.c. \quad (2.73)$$

The polarization $\mathbf{P}^{(2)}$ is given by:

$$\begin{aligned} \mathbf{P}^{(2)}(t) = \epsilon_0 \chi^{(2)} & \left[E_1^2 e^{-2i\omega_1 t} + E_2^2 e^{-2i\omega_2 t} + 2E_1 E_2 e^{-i(\omega_1 + \omega_2)t} \right. \\ & \left. + 2E_1 E_2^* e^{-i(\omega_1 - \omega_2)t} + c.c. \right] \\ & + \epsilon_0 \chi^{(2)} |E_1|^2 + |E_2|^2 \end{aligned} \quad (2.74)$$

where *c.c.* is the complex conjugate.

Second Harmonic Generation is a special case of three-wave mixing where $\omega_1 = \omega_2 = \omega$ and $E_1 = E_2 = E_\omega$. Eq.2.74 can be simplified as:

$$\mathbf{P}^{(2)}(t) = 2\epsilon_0 \chi^{(2)} |E_\omega|^2 + (\epsilon_0 \chi^{(2)} E_\omega^2 e^{-i2\omega t} + c.c.) \quad (2.75)$$

which has frequency components at 2ω and 0. The second term, which corresponds to the oscillation at 2ω , gives the second-order polarization, which is written as:

$$\mathbf{P}_{2\omega}^{(2)} = \epsilon_0 \chi^{(2)} E_\omega^2 \quad (2.76)$$

$$= 2\epsilon_0 d_{eff} E_\omega \quad (2.77)$$

where d_{eff} is the effective nonlinearity, used instead of the susceptibility $\chi^{(2)}$.

Similarly, $\mathbf{P}_\omega^{(2)}$ can be obtained by using $\omega_1 = 2\omega$ and $\omega_2 = -\omega$, $E_1 = E_{2\omega}$ and $E_2 = E_{-\omega} = E_\omega^*$ in equations 2.73 and 2.74. The result can be expressed as:

$$\mathbf{P}_\omega^{(2)} = 4\epsilon_0 d_{eff} E_{2\omega} E_\omega^* \quad (2.78)$$

Substituting Eq.2.77 and 2.78 into 2.71 results in:

$$\frac{\partial E_\omega}{\partial z} = \frac{2i\omega^2}{k_1 c^2} d_{eff} E_{2\omega} E_\omega^* e^{-i\Delta k z} \quad (2.79)$$

$$\frac{\partial E_{2\omega}}{\partial z} = \frac{2i(2\omega)^2}{k_2 c^2} d_{eff} E_\omega^2 e^{i\Delta k z} \quad (2.80)$$

where k_1 and k_2 are the wave vectors for the fundamental and second-order waves and $\Delta k = 2k_1 - k_2$. Phase matching is essential for efficient SHG. It requires the phase velocities of the interacting waves to be matched such that $\Delta k = 0$. This can be achieved using various techniques such as angle tuning.

At low conversion efficiency, the fundamental beam is nearly undepleted, meaning its

amplitude does not significantly change as it propagates through the medium with an interaction length of l . With $|E_\omega(z)| = \text{const}$, $E_{2\omega}$ can be obtained directly by integrating the second equation in Eq.2.80, written as:

$$E_{2\omega} = \frac{2i(2\omega)^2}{k_2c^2}d_{eff}E_\omega^2 \int_0^l e^{i\Delta kz} dz \quad (2.81)$$

The phase matching $\Delta k = 0$ gives the result:

$$E_{2\omega} = \frac{2i(2\omega)^2}{k_2c^2}d_{eff}E_\omega^2 \int_0^l 1 dz \quad (2.82)$$

$$= \frac{2i(2\omega)^2}{k_2c^2}d_{eff}E_\omega^2 l \quad (2.83)$$

According to Eq.2.14, the intensity of 2ω beam is:

$$I_{2\omega} \propto |E_{2\omega}|^2 \propto |E_\omega|^4 \propto I_\omega^2 \quad (2.84)$$

In conclusion, at low conversion rate and with phase matching, the generated second-order beam intensity is proportional to the quadratic of the fundamental beam intensity.

3 Point-to-Point Imaging of Focal Spot

3.1 Pulse aberrations in the transversal plane

Fig.3.1 shows the map of the outskirts area of Hamburg with the locations of DESY, European XFEL, and the LUXE project. LUXE uses the accelerated electron beams from European XFEL before undulators.

The blueprint of the building of the LUXE project [9], as depicted in Fig.3.2, shows

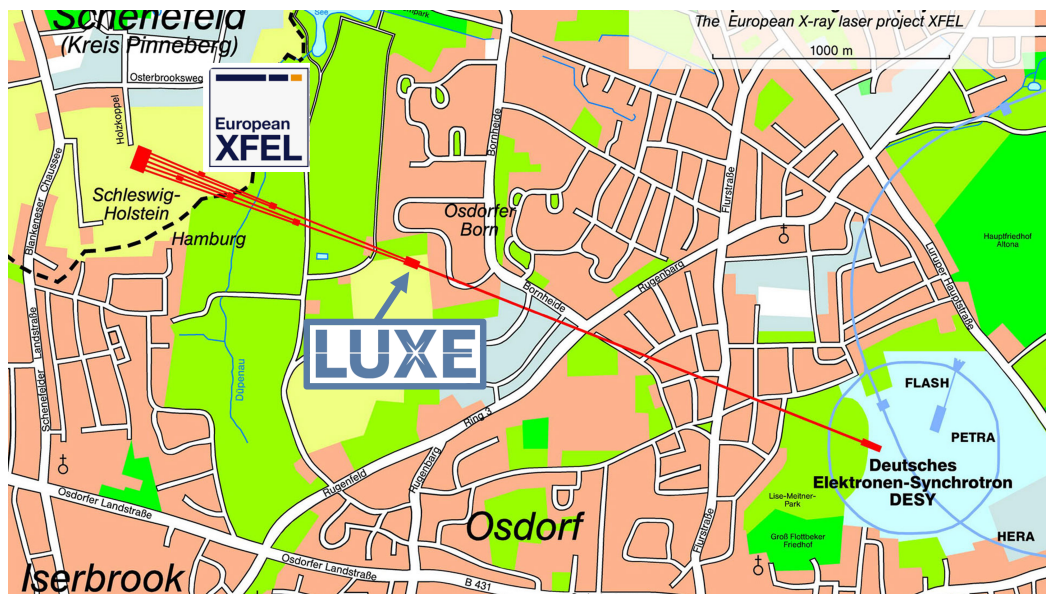


Figure 3.1: The map of the outskirts area of Hamburg shows the locations of DESY, European XFEL, and the building for the LUXE project.

that the laser and diagnostic system are housed in a separate building from the interaction point (IP), where the laser interacts with electron bunches. The laser pulse should propagate approximately 40 meters through the vacuum pipes (represented by red lines) to reach the IP. After the interaction, it propagates back to the diagnostic system, which lies next to the laser system, for another 40 meters.

However, for a laser beam propagating in free space, the laser beam intensity distribution gains aberrations during such a long distance. As a result, the laser focal spot at the diagnostic table differs from that at IP, which will significantly degrade

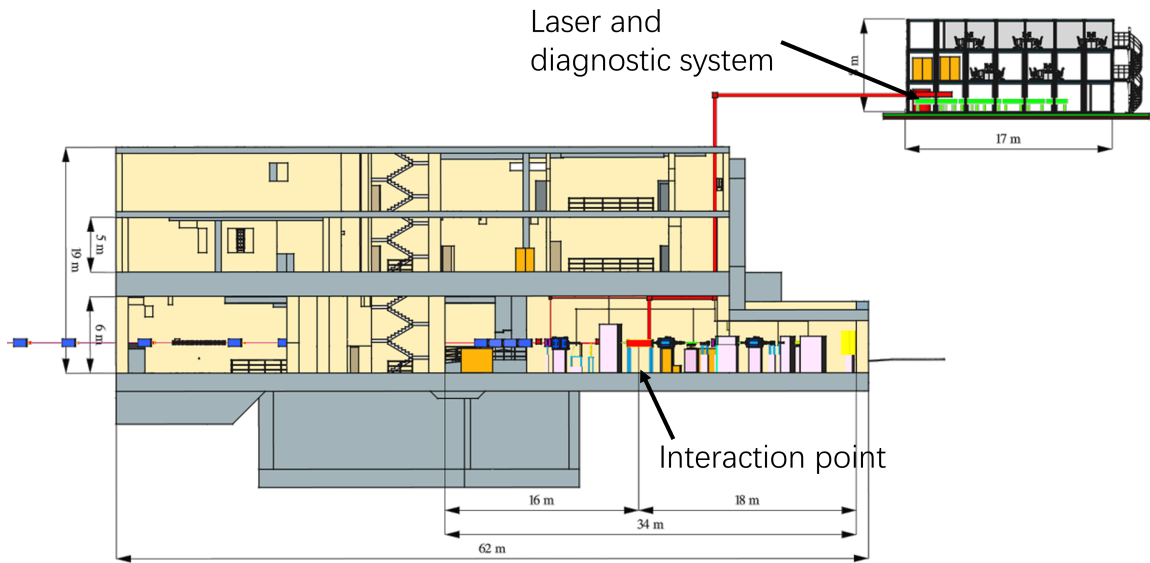


Figure 3.2: The design of the LUXE building and the layout.

the accuracy and precision of laser intensity diagnostics. In addition, the imperfect optics used in the real world cause distortions to pulse transversal mode as well. Here, this section characterizes the aberrations and discusses the possible solutions to these aberrations in the next section.

Pulse aberrations can be caused due to long-distance propagation as the wavefront curvature varies with the distance. As discussed in Sec.2.2.3, the wavefront curvature radius is defined as:

$$R(z) = z + z_R^2/z. \quad (3.1)$$

$R(z)$ has the minimum value at $z = z_R$ and approaches infinity near the beam waist. Further propagation causes the beam to diverge, leading to an increase in $R(z)$ as the beam spreads out and it also approaches infinity when extremely far from the focus. For the laser beam used in the initial stage of LUXE, the beam diameter is 5 cm. As the beam propagates freely to a distance of 40 m the value of $R(z)$ changes. This indicates that the beam is no longer identical to the initial beam profile.

Simulations of a laser beam propagating freely for a distance of 40 meters in a vacuum beam line are calculated. The beam has an initial Gaussian intensity profile and an aberration-free wavefront, as depicted in Fig.3.3(a). The simulation results show that, over the long-distance propagation, the intensity distribution does not change, while the wavefront gains a curvature with a peak-to-valley (PtV) value of 0.03λ . The simulation results for a super-Gaussian beam with the same diameter are plotted

in Fig.3.3(d)-(f). The intensity profile becomes distorted with a structure of fringes, with a peak fluence reaching 1.2 of the initial. The wavefront has gained an aberration with a PtV of 0.28λ .

To focus a collimated beam to the diffraction limit, it is crucial to select the ap-

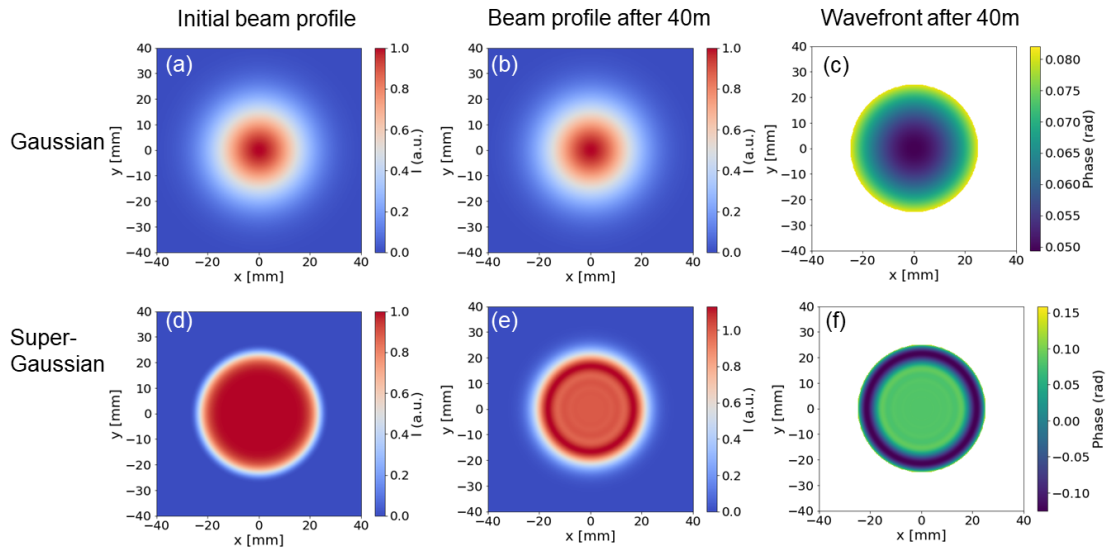


Figure 3.3: To emphasize the importance of imaging the beam to the diagnostic table, simulation shows that long-distance free-space propagation causes significant distortion on the laser profile. (a)/(d) The initial beam is defined with a Gaussian/super-Gaussian with $p=6$ intensity profile and flat wavefront with a central wavelength of 800 nm. After propagation in vacuum for 40 meters, (b) and (e) show the beam intensity profiles of each. (c) (f) the wavefront aberrations become significant.

propriate optics. Otherwise, both the wavefront and the intensity profile would gain significant distortions. For point-to-point imaging, elliptical mirrors are preferred, whereas spherical mirrors excel in 1:1 imaging of a point source back to its original position. The conic constant K is a coefficient that describes conic sections, defined as $K = -e^2$, where e is the eccentricity. A sphere has $K = 0$, a parabola has $K = -1$, and ellipses are in the range of $-1 < K < 0$ and $K > 0$. However, using a concave spherical mirror for focusing a collimated beam can introduce spherical aberrations, enlarging the focal spot size to be larger than the diffraction limit.

In the initial phase of the LUXE project, it requires to focus a collimated beam with a diameter of 5 cm with $f/3$ to the interaction point. To understand the possible wavefront distortions caused by focusing optics and to compare different focusing optics, simulations are performed using Zemax OpticStudio ray-tracing software [76],

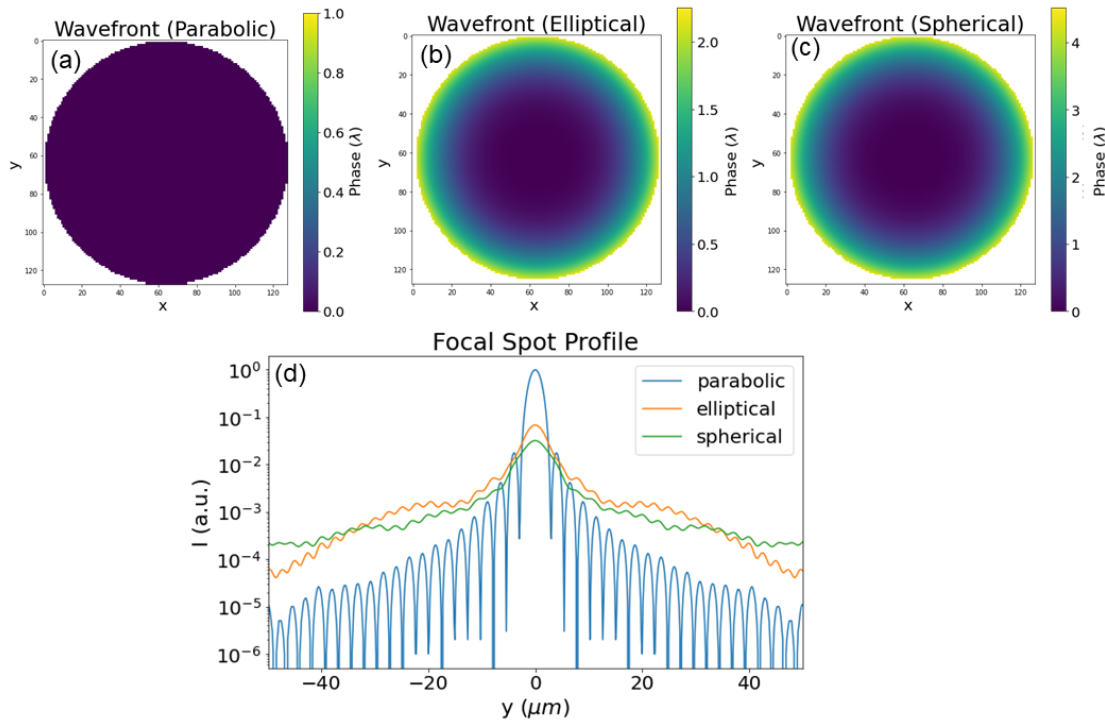


Figure 3.4: The wavefront at the focal plane after focusing a collimated beam by (a) a parabolic, (b) an elliptical, and (c) a spherical mirror, respectively. Note that the scales of the color bars are different for each plot. (d) Lineout of the focal spot intensity vertical profile at $x=0$, plotted in the log scale for the three cases.

and the simulation results are shown in Fig. 3.4. The initial input conditions for all three cases are the same with a super-Gaussian intensity distribution as depicted in Fig.3.3 (d) and a flat wavefront. The wavefront of the focal spot using the parabolic mirror is flat with infinite curvature, as shown in Fig. 3.4(a), making the diffraction-limited focus profile possible. In contrast, the wavefront using an elliptical mirror with $K = -0.5$ shows significant distortion with a peak-to-valley (PtV) value of 2.25λ and a root mean square (RMS) value of 0.67λ , as shown in Fig. 3.4(b). Such wavefront distortions can be decomposed into Zernike modes, with the term of defocus $Z_2^0 = 1.40\lambda$ and the primary spherical aberration term $Z_4^0 = 0.11\lambda$. The wavefront using a spherical mirror has a PtV value of 4.52λ and an RMS value of 1.34λ , as shown in Fig. 3.4(c). Its decomposition into Zernike modes is $Z_2^0 = 2.40\lambda$ and $Z_4^0 = 0.25\lambda$. When the focusing optics are not selected appropriately, wavefront distortions of high orders will be introduced, such as Z_4^0 . The focal spot size exceeds the diffraction limit, and the peak fluence can be significantly decreased to less than 10%.

In the laser beam path, the surface figures of the optical elements also contribute to wavefront aberrations. The two main parameters to describe the surface figure are accuracy and roughness. The accuracy refers to the deviation of the surface from a perfect plane. The primary source of flatness is the manufacturing process which introduces deviations due to the residual stresses or thermal gradients. Mechanical stress can also cause extra tension on the surface during improper handling or mounting. Roughness, on the other hand, refers to the random variations or irregularities in a surface's topography on a microscopic scale, finer than flatness. It is introduced during the manufacturing or surface treatment process. In addition to accuracy and roughness, scratches and pits are distinct types of surface defects that are more visible and can significantly impact optical performance. These defects can arise from the grinding and polishing process during manufacturing, where small particles of abrasive material may become embedded in the surface, causing microscopic scratches and pits. Improper handling and the presence of contaminants can also contribute to the occurrence of scratches and pits.

3.2 Simulations of two imaging setups using Zemax

To accurately characterize the intensity of the laser focus at the IP, it is essential to reconstruct an identical focus at the diagnostics system while minimizing any distortions. Two different setups have been simulated using ZEMAX to achieve this goal, as shown in figures 3.5 and 3.6.

3.2.1 Imaging setup using 3 parabolic mirrors

The Setup1 is depicted in Fig. 3.5. At the transversal plane A, the incident beam parameters are defined to be the same as those in Fig. 3.3(d), where a super-Gaussian intensity profile and a wavefront with infinite curvature are presented. The first off-axis parabolic mirror (OAP1) is used to focus the laser with $f/3$, aiming to achieve diffraction-limit at the IP plane. Once a tightly focused, aberration-free focal spot is obtained at the IP, the beam is recollimated by OAP2, which is identical to OAP1. The distance between IP and OAP2 is exactly the focal length of OAP2. The beam is then transported through a 40m laser path in vacuum to the diagnostic table. An identical image of the focus at IP' is obtained using the same focusing parabolic mirror

OAP3 at the entrance to the diagnostic system. This setup has been designed to ensure minimal distortion and maximum precision in characterizing the focus intensity at the IP.

Although this approach is theoretically feasible, achieving the required level of pre-

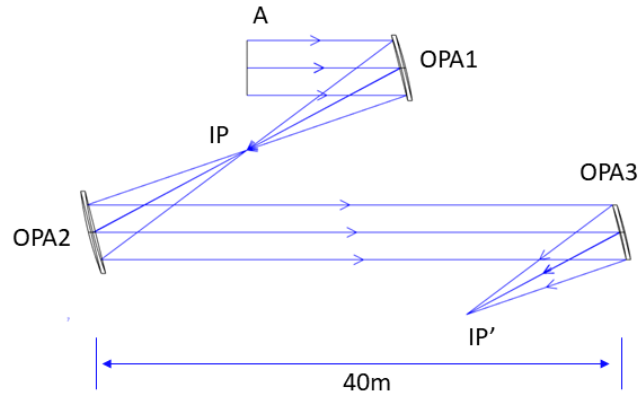


Figure 3.5: The setup 1 of imaging the focal spot at IP to the IP' plane at the diagnostic system using 3 OAPs.

cision can be challenging. It necessitates high surface precision for the two imaging off-axis parabolic mirrors (OAP2 and OAP3) and all the large aperture mirrors used to steer the beam between them. Any surface irregularity or imperfection in these optics can introduce additional wavefront distortions, degrading the imaging performance and ultimately compromising the precision of the focus intensity characterization at the IP.

3.2.2 Imaging setup for direct imaging

An alternative system, Setup2 sketched in Fig.3.6, has been considered to image the focal spot at IP directly to IP'. The initial beam settings and OAP1 are identical to those in Setup1 shown in Fig.3.5. However, instead of re-collimating the beam, OAP2 is shifted slightly off position and converges the beam over a distance of 40 meters, directly imaging the plane at IP to IP'. The beam during propagation over the 40 m distance can be treated as quasi-collimated. Moreover, it has a smaller diameter on the optics in the beam path, resulting in less wavefront distortion as high-quality optics in smaller sizes are easier to manufacture and more available. This setup reduces the complexity of the optical system while maintaining the required level of precision.

Most importantly, this direct imaging ensures that any changes present at IP are reproduced at IP', and minimizes the potential for introducing new aberrations during the imaging process.

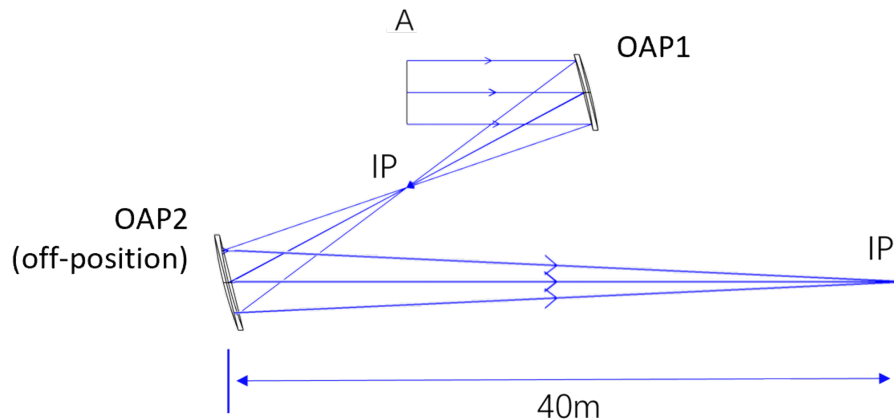


Figure 3.6: The setup 2 directly images the IP plane to IP' at the diagnostic system using OAP2 that slightly shifted off position.

3.2.3 Comparison of two setups

The simulation results of the focal spot intensity profiles and the wavefront at the IP' plane are presented in Fig.3.7. Fig.3.7(a) shows the wavefront for Setup1, which is ideally flat and aberration-free as the incident beam. In the case of Setup2, although an off-axis ellipsoidal mirror would have been a better option for point-to-point imaging, it is not readily available due to the difficult manufacturing process. Despite this limitation, the wavefront aberration shown in Fig.3.7(b) has a PtV value of 0.07λ and RMS of 0.02λ . Compared to the surface accuracy of the best available OAPs ($\lambda/20$ RMS wavefront distortion [77]), the effect of using the OAP directly to image the spot is acceptable. The wavefront aberration is mainly composed of the defocus term with $Z_2^0 < 0.01\lambda$, which only corresponds to the longitudinal focal shift and the higher-order Zernike modes are negligible here. Such small aberrations allow a high-quality image to be formed, as the lineout of the focal spots shown in Fig.3.7(c). The focal spot sizes are different with a magnification of 250 times for Setup2 compared to Setup1. But the intensity profiles overlap very well until the diameter of 7 times the focal spot size to the order below 10^{-4} .

The setups depicted for simulation purposes in Fig.3.5 and Fig.3.6 are simplified

representations of more complex real-world configurations. In reality, there will be wedged, uncoated fused silica for laser energy attenuation, steering mirrors for beam transportation, and other optical surfaces. All of these optical surfaces have to be of excellent quality to achieve high-fidelity wavefronts, especially the OAPs. For example, Optical Surface [77] offers OAPs with surface accuracy up to $\lambda/20$ at 633 nm and micro-roughness typically less than 1.2 nm RMS.

The focus profiles in Fig.3.5(b) and Fig.3.6(b) have different radius scales but share

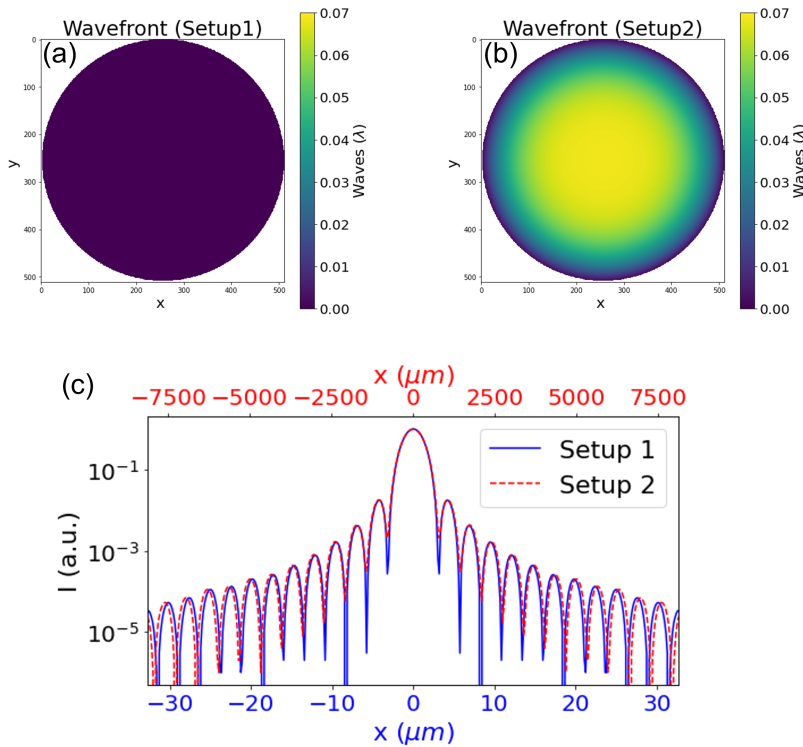


Figure 3.7: (a) the wavefront at IP' in Setup 1 (b) the wavefront at IP' in Seupt 2 (c) the lineout of focal spot intensity profiles at IP' in both Setup1 (blue solid line, lower x-axis) and Setup2 (red dashed line, upper x-axis).

the same shape, including side maxima peaks, under the assumption of perfect optical surfaces. For subsequent diagnostics, it is necessary for Setup2 to calibrate the intensity profile according to the magnification of the beam size. However, the focal spot diameter between the two first sidelobes is roughly 2 mm, while the size of the CCD camera's sensor chips used to capture these focal spot images is also a few mm. A camera with a large enough sensor should be used to capture the focal spot images. In the first setup, all the beam-transporting optics require a full aperture, which is 5 cm in the first phase and will be upgraded to 15 cm later as planned by the LUXE project. Large optics with their bulky mountings are constrained by the limited space

in vacuum pipes. Conversely, the second setup benefits from a beam converging over 40 meters, allowing near-collimated operation with a smaller beam size, easing the demands for bulky optics and complex alignment.

4 Full On-Shot Laser Intensity Diagnostics

On-shot laser intensity diagnostics on the JETi laser involve comprehensive measurements of laser focal spot parameters, including pulse duration, energy, spectrum, and fluence distribution. Prior to the measurement process, the optimization of the wavefront by an adaptive mirror and spectral phase by a Dazzler has achieved. This diagnostic approach aims to achieve on-shot intensity measurements with a precision of 1%, as required by the LUXE project, ensuring a high level of precision in assessing laser performance and SFQED phenomena.

4.1 Experiment setup

The intensity of an ultrashort laser pulse with negligible STCs can be computed using Eq.2.63, wherein the three parameters the energy E , the FWHM pulse duration τ , and the FWHM area A are determined by measuring individually. To this end, a dedicated measurement system is designed, as illustrated in Fig. 5.1.

This experimental setup utilizes the leak light from a steering mirror located before the laser beam entering the interaction chamber. The steering mirror exhibits a high reflection rate and only a 0.1% transmission rate. As the input and output surfaces of the steering mirror are parallel and flat, the wavefront will remain unchanged. The beam is initially focused by an off-axis parabolic mirror with a focal length of 60 cm. Subsequently, the focal plane is imaged onto CCD1 via a microscope objective (MO, Mitutoyo M Plan Apo NIR 10X).

The energy of the pulse can be calculated from the on-shot near-field image captured by CCD2 and the corresponding spectrum. The CCD2 is located 75 cm from the parabola and obtains the NF image approximately 3 meters prior to the OAP, which is situated in the vicinity of the steering mirror. Simultaneously, the spectrum is obtained by using a spectrometer (Thorlabs CCS175/M), where a portion of the laser beam is separated using a beamsplitter and conveyed through an optical fiber to the spectrometer.

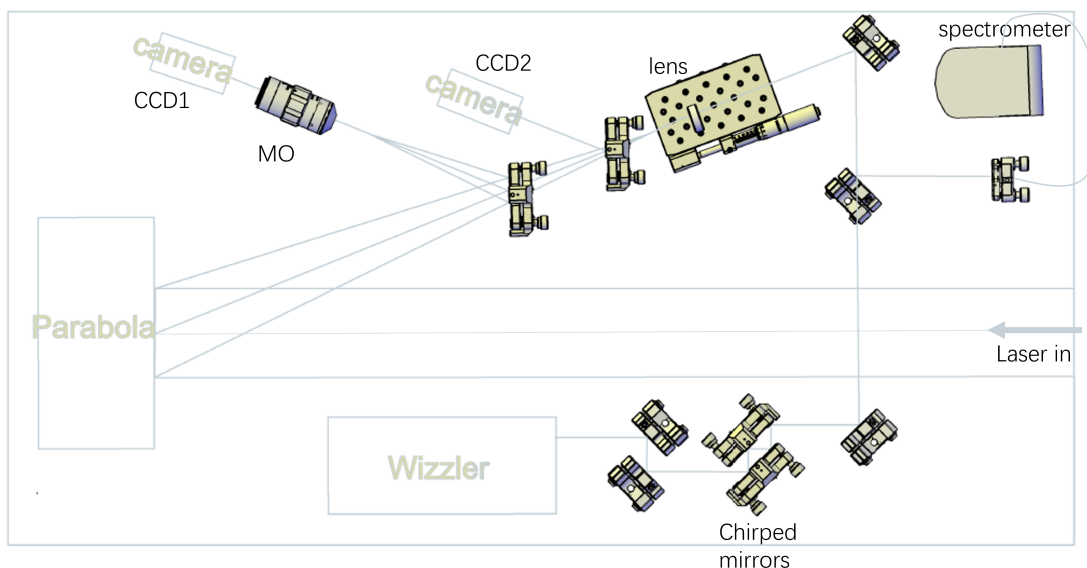


Figure 4.1: The experiment setup for on-shot diagnostics of ultrashort laser pulse

In order to ensure the collimation of the incident laser beam into the Wizzler, which is a device that measures the temporal profile and the spectral phase of ultrashort pulses, an achromatic lens with $f=50$ mm is used to re-collimate the beam. A pair of chirped mirrors before the Wizzler compensate for the dispersions caused by various optical components, including the thick steering mirror and the vacuum windows. The chirped mirrors provide a compensation of $-400fs^2$ per reflection.

4.2 JETi200 laser system

The experimental work presented in this thesis was conducted using the JETi200 laser system located at the Helmholtz Institute Jena in Germany [78]. The JETi200 is a commercial model of a high-intensity laser system from Amplitude Technologies that utilizes the medium of Ti:Sapphire with a central wavelength of 800 nm. With a peak power of 300 TW, the laser is capable of delivering on-target energy of up to 5 J with a pulse duration typically 20 fs at a repetition rate of 5 Hz.

JETi200 utilizes a double CPA amplification scheme. Chirped pulse amplification (CPA) is a groundbreaking technique that amplifies laser pulses to several Joules and compresses them to durations of down to femtoseconds, achieving power levels in the Petawatt range and peak intensities up to $10^{23} W/cm^2$ [23]. Initially developed for radar, CPA was adapted for optical waves in 1985 by Donna Strickland and Gérard

Mourou, who received the Nobel Prize in Physics in 2018 [22]. The CPA process involves three main steps: stretching, amplifying, and compressing the pulse. First, the pulse from an oscillator is stretched in time using dispersive optical elements like anti-parallel gratings, increasing its duration by 10^3 to 10^5 times to reduce peak power and prevent damage during amplification. The stretched pulse is then amplified using a gain medium, such as titanium-doped sapphire, excited by a pump laser. Finally, the pulse is compressed and compensated for the dispersion introduced during stretching, resulting in a short-duration, high-peak-power pulse.

In the first CPA system, the pulses are stretched, amplified to 1 mJ and then compressed to a duration of less than 30 fs.

After the first CPA, the laser transmits through an XPW crystal to improve the temporal contrast, which is defined as the ratio of the peak intensity of the main laser pulse to the intensity of the amplified spontaneous emission (ASE) background. In CPA systems, the temporal contrast ratio typically ranges between 10^{-6} to 10^{-7} due to various factors such as ASE from the regenerative amplifier, pre-pulses from previous amplification stages, and phase distortions from spectral clipping. The laser pulse is required to have high contrast to prevent the production of a pre-plasma before the arrival of the main pulse at the target. Cross-polarized wave generation (XPW) is a third-order nonlinear optical effect that generates a wave with polarization perpendicular to the incident wave [79]. The intensity of the generated signal exhibits a cubic dependence on the intensity of the fundamental wave, resulting in an enhancement of the temporal contrast by three orders of magnitude [80]. The temporal contrast of JETi200, measured by third-order cross-correlation measurement (Sequoia, Amplitude Technologies) [81], is lower than the order of 10^{-10} [82].

The pulses are once again temporally stretched and further amplified in the second CPA stage. Six Nd:YAG lasers (Titan, Amplitude) [83], are used to pump the Ti:Sapphire crystal in the amplifier, to amplify the laser energy stage-by-stage, to the level of 5 Joules.

To optimize the temporal profile of the laser pulse, the technology of acousto-optic programmable dispersive filter (AOPDF) [84] (Dazzler, Fastlite) is installed after the stretcher in CPA2 to compensate for the spectral phase of laser pulses. It operates by exploiting the longitudinal interaction between a polychromatic acoustic wave and a light wave within a birefringent crystal. This interaction allows precise control of the spectral phase by dynamically adjusting the phase and amplitude of different

frequency components by modulating the acoustic wave, allowing for real-time manipulation of the pulse shape and duration.

A deformable mirror (MD-140-C-53, ISP Systems) [85] is employed to compensate for accumulated wavefront aberrations from the laser chain and beamline, to focus the laser pulses close to their diffraction limit, or to shape the focal spots according to experimental requirements.

The pulse in this ultrafast laser system is optimized to achieve a peak intensity up to the level of 10^{21} W/cm^2 when focused by an off-axis parabolic mirror. Such a high-intensity laser system provides a powerful tool in various applications, such as laser-driven particle acceleration [86–88], and high harmonic generation [89].

4.3 Precision Assessment on Laser Intensity Diagnostics

This section focuses on the evaluation of individual measurements' precision for various laser parameters, including the resolution of the images of near-field and far-field, the relative energy related to counts detected by CCD and the pulse duration accuracy. The goal is to ensure each parameter is measured with high precision, contributing to the comprehensive on-shot diagnostics of laser intensity with a targeted precision of 1%.

To determine the precision of the fluence F captured by CCD, according to the equation $F = E/A$, the precision of the measurement of the total counts detected by CCD (which corresponds to E) and the size of laser beams (A) are evaluated.

To accurately determine the beam size, it is essential to calibrate the magnification of the images captured by cameras. This calibration involves the use of a grating with known period slits placed in the beam path, and then captures near-field and far-field images.

The process to determine the near-field image magnification is straightforward. The NF image of the grating captured by the CCD shows fringe distances that measure 35.5 pixels, which corresponds to the period length of the grating of 10 mm. The magnification factor of the NF image is $10 \text{ mm} \div 35.5 \text{ pixels} = 0.282 \text{ mm/pixel}$.

Calibrating the magnification for far-field images can be approached by capturing the FF image with the grating in beam path, which shows a periodic structure of bright

fringes. The magnification coefficient can be calculated using the formula $\lambda f / (n_{px}d)$, where f is the focal length of the focusing off-axis parabolic mirror, n_{px} is the number of pixels between two fringes, and d is the period length of the grating. This method yields a magnification factor of $0.40 \mu\text{m}/\text{pixel}$. The precision of the focal spot size is limited by the magnification of the focal plane. In instances where a focal spot image has a $D4\sigma$ diameter of approximately $50 \mu\text{m}$ in either vertical or horizontal axis, the precision of the focal spot area is:

$$\frac{\Delta A}{A} = \sqrt{\left(\frac{0.4\mu\text{m}/\text{pixel}}{50\mu\text{m}}\right)^2} \times 2 = 1.1\%. \quad (4.1)$$

CCD camera sensors exhibit nonlinear response characteristics to the fluence of the incident beam when peak counts approach saturation levels. This nonlinearity is plotted in Fig.4.2, showing the relationship between peak counts and incident energy measured using the GT1660 camera from Allied Vision [90]. The variation in incident laser energy on the CCD sensor is modulated by adjusting the neutral density filters placed before the camera. The plot reveals that the CCD sensor's conversion of incident photons to electronic signals deviates from linearity beyond peak counts of 10,000, up to the saturation threshold of 2^{14} . Appropriate ND filter values should be chosen carefully to utilize the CCD's linear dynamic range effectively which ensures an optimal signal-to-noise ratio, crucial for achieving high precision in intensity measurements, while maintaining peak counts at around 10,000 level to avoid uncertainties introduced by nonlinear response. Additionally, the dark current is up to 470 electrons per pixel per second [91], which refers to the signal that is generated by the camera's sensor in the absence of light. This noise is caused by thermal fluctuations and other electronic processes within the sensor. The effective dynamic range of this CCD gives 40 dB, obtained by:

$$\text{Dynamic Range} = 20\log_{10} \frac{\text{peak signal counts}}{\text{noise floor}} \quad (4.2)$$

With the high resolution of the focal spot and the appropriate peak count <1000 per pixel of the CCD, the total count within the FWHM yields approximately $N = 3 \times 10^6$, which results in the precision of the relative FWHM energy $\frac{\Delta E}{E}$ of better than 0.05%, derived from the Poisson noise defined as \sqrt{N}/N .

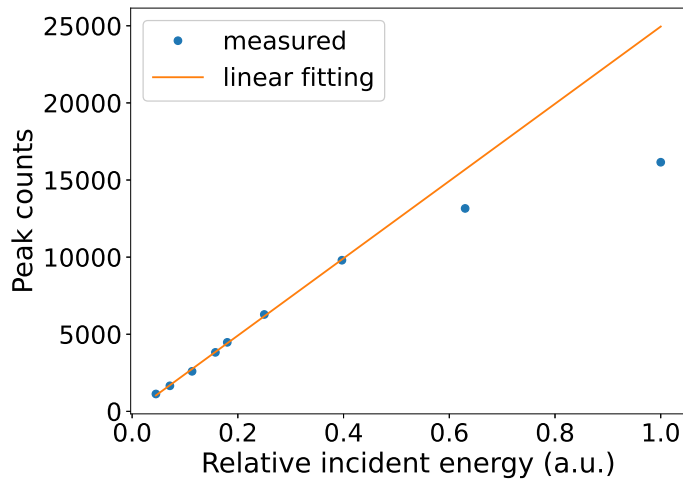


Figure 4.2: The peak counts vs relative incident laser energy with a linear fitting.

The relative energy of each pulse is gauged by aggregating the total counts from the NF image captured on a CCD, potentially reaching 10^9 , yielding precision at the order of 10^{-5} .

The pulse duration is measured using the Wizzler device, which is particularly accurate when the pulse approaches the Fourier transform limit (FTL). In the context of the LUXE experiment, which operates with pulses near the FTL, the Wizzler is expected to deliver a precision of better than 0.2% [92].

In total, the precision of the laser pulse intensity can be obtained by considering the precision of each measurement method:

$$\frac{\Delta I}{I} = \sqrt{\left(\frac{\Delta E}{E}\right)^2 + \left(\frac{\Delta A}{A}\right)^2 + \left(\frac{\Delta \tau}{\tau}\right)^2} \quad (4.3)$$

which gives $\sqrt{0.05\%^2 + 1.1\%^2 + 0.2\%^2} = 1.1\%$.

The precision of laser intensity measurement is fundamentally constrained by the Rayleigh length of the beam, as the laser radius and intensity vary along the z-axis, as shown in Eq.2.45. Achieving high-precision spatial-temporal overlapping between the ultrashort laser pulse and the electron bunch is crucial for the LUXE experiment. For the interaction between the laser pulse and the electron bunch to remain within an intensity variation of 1%, a temporal precision with a tolerance of 30 fs is required, underscoring the stringent demands for precision laser intensity and timing control in experimental setups [24].

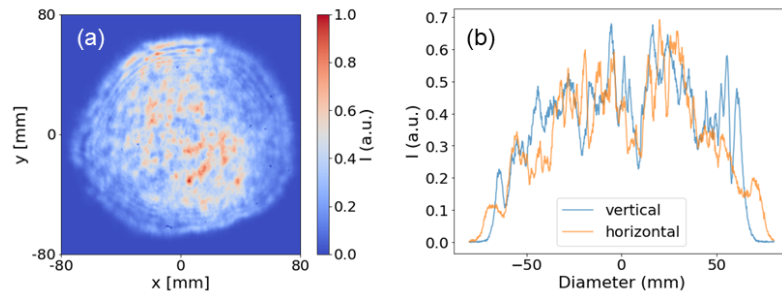


Figure 4.3: (a) The near field image and (b) the plot along the vertical and the horizontal axis

4.4 Near Field

Fig.4.3(a) displays the near-field image obtained via a CCD camera, with the image of the NF 2 meters prior to the OAP mirror being imaged onto the diagnostic system and captured by CCD2 for each shot, as described in Fig.5.1. The $D4\sigma_x$ of the near-field is 122.1 mm and the $D4\sigma_y$ is 119.7 mm. The fringes of the NF profile, as shown in Fig.4.3(b), happen when a laser beam with a super-Gaussian NF profile propagates for a long distance of approximately 20 meters to the OAP, as illustrated in Fig.3.3.

4.5 Focal Spot

The focal spot captured by CCD1 through the imaging of a microscope objective is presented in this section.

4.5.1 Focal Spot

Fig.4.4(a) shows the focal spot image along with the ellipse fitting contour at the half maximum values. The length of the major axis of the ellipse fitting is $24.7 \mu\text{m}$ and the minor axis measures $20.5 \mu\text{m}$. Fig.4.4(b) and (c) present the intensity profiles plotted along the vertical axis at $x=0$ and along the horizontal axis at $y=0$, respectively, along with their Gaussian fitting curves. From these Gaussian fits, the FWHM focal spot diameter is determined to be $19.1 \mu\text{m}$ vertically and $23.1 \mu\text{m}$ horizontally. The Q-factor, defined as the ratio of the energy encircled within FWHM relative to the

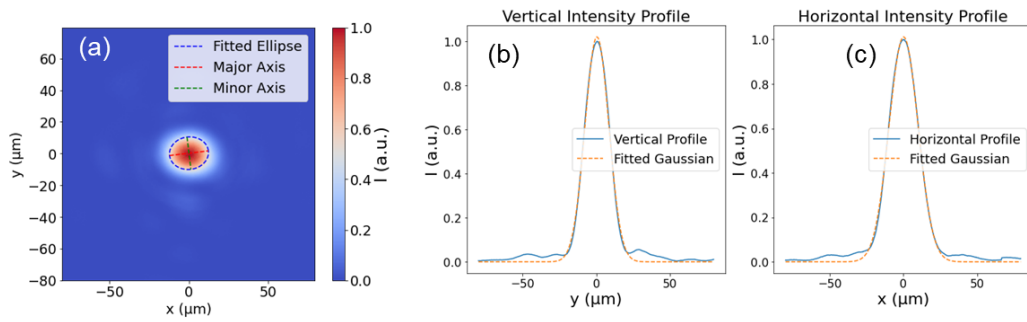


Figure 4.4: (a) the focal spot profile with an elliptical fitting and the plot along (b) the vertical and (c) the horizontal axis with Gaussian fitting curves

total energy, is determined to be 49.1%. Although this number is very close to the theoretical expectation for non-aberrated beams, which is 50% for a Gaussian beam, the area considered in practical measurements is finite, whereas the theoretical value is calculated over an infinite plane. Consequently, the energy spread in the outer regions is not considered in the finite area.

On the other hand, Fig.4.5 displays the diffraction-limited focal spot calculated by taking the Fourier transform of the measured near-field, as shown in Fig.4.3(a). The FWHM diameter is 14.9 and 14.8 μm for the vertical and horizontal axis respectively. The corresponding Q-factor is 52.6%.

Comparing these results, the experimentally obtained focal spot is larger and less

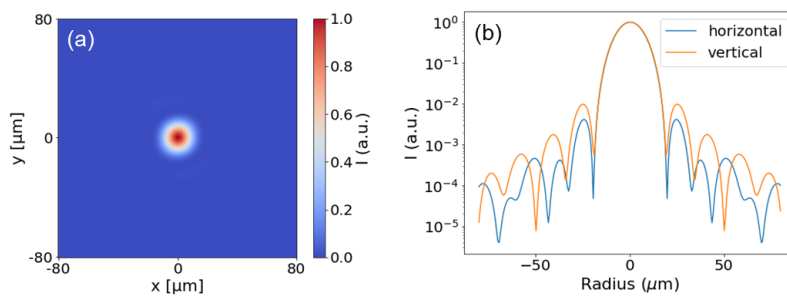


Figure 4.5: (a) Diffraction-limited focal spot and (b) its lineout along vertical and horizontal axis.

symmetrical than the diffraction-limited spot predicted by the Fourier transform of the near-field. The experimentally measured Q-factor of 49.1% is slightly lower than the calculated Q-factor of 52.6%, indicating that the experimental focal spot has a slightly lower energy concentration within the FWHM compared to the ideal diffraction-limited case. These discrepancies can be attributed to various factors, such

as wavefront aberrations.

Before the measurement of the laser intensity, the wavefront has been optimized

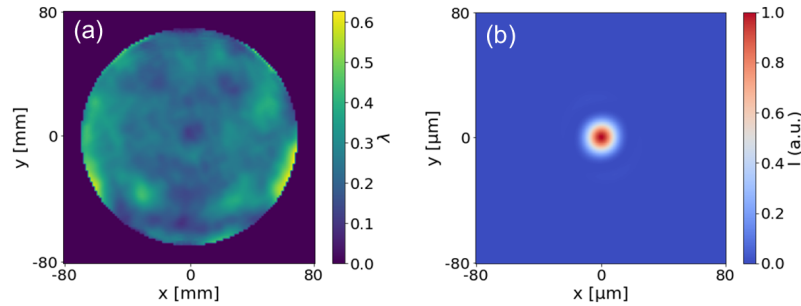


Figure 4.6: (a) the measured wavefront, (b) the calculated focal spot with the wavefront

by using a deformable mirror. The measured wavefront is presented in Fig.4.6. The peak-to-valley (PtV) value is 0.63λ and the root-mean-square (RMS) value is 0.07λ , resulting in a Strehl ratio of 0.87. Decomposing the wavefront into Zernike modes gives (in the unit of λ): $0.03Z_2^2$, $0.04Z_2^{-2}$, $0.01Z_3^1$, $0Z_3^{-1}$, $0Z_3^3$, and $-0.01Z_3^{-3}$. By calculating the focal spot by applying the wavefront to the nearfield, the resulting FWHM diameter is $15.1 \mu\text{m}$ and $14.9 \mu\text{m}$ for the vertical and horizontal axes, respectively, and the Q-factor is 52.2%. This calculation, however, does not match the measured value closely, indicating that wavefront aberrations alone do not entirely account for the observed discrepancies.

The difference suggests additional influencing factors, such as spatio-temporal couplings (STC). STC causes the focal spot of each wavelength to shift in both longitudinal and transversal directions. This results in a broader and less intense focal spot than theoretically predicted. The results of measuring spatio-temporal couplings are presented in Chapter 6.

4.5.2 High Dynamic Range

Including the fluence distribution at lower levels can significantly enhance the accuracy of calculating the energy enclosed within the central part of a laser pulse. A significant portion of the pulse energy might remain undetected in low dynamic range diagnostics. This underestimation can lead to systematic overestimates of laser intensity. By factoring in the lower-level fluence distribution, more accurate energy

calculations are obtained. This is achieved by employing high dynamic range (HDR) measurements of the focal spot. The method involves capturing focal spot images with different attenuation levels on the CCD. By discarding counts that exceed 10,000 to improve precision and stitching together the remaining data while adjusting for the energy ratios between the images, a dynamic range extension of 10^4 is achieved, as plotted in Fig.4.7. The Q-factor is determined to be 48.7% using this method.

The expected Q-factor value can be obtained by taking the Fourier transform of the

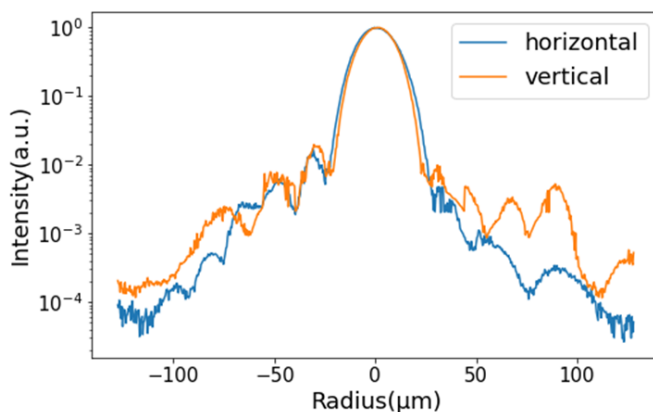


Figure 4.7: the dynamic range of the focal spot along the vertical axis at $x=0$ and along the horizontal axis at $y=0$

near field. The calculation result is plotted in Fig.4.8, which is the same result as in Fig.4.5 but with a larger distance to improve the accuracy of calculating the Q-factor. The result is 52.0%. Comparing these results to the measured Q-factor of 49.1% and the calculated Q-factor of 52.6% from the earlier calculation, a difference of 0.4% and 0.6%, respectively, is observed. This slight discrepancy highlights an improvement in the accuracy of determining the relative energy within the FWHM, thus improving the determination of focal spot intensity.

4.6 Energy

While an energy meter can provide a simple and direct measurement of laser pulse energy, the precision of this approach is not sufficient, with an uncertainty of $\pm 3\%$ (Gentec-EO, [93]). In this work, the laser pulse energy is calculated using the near-field profile and the corresponding spectrum of the pulse.

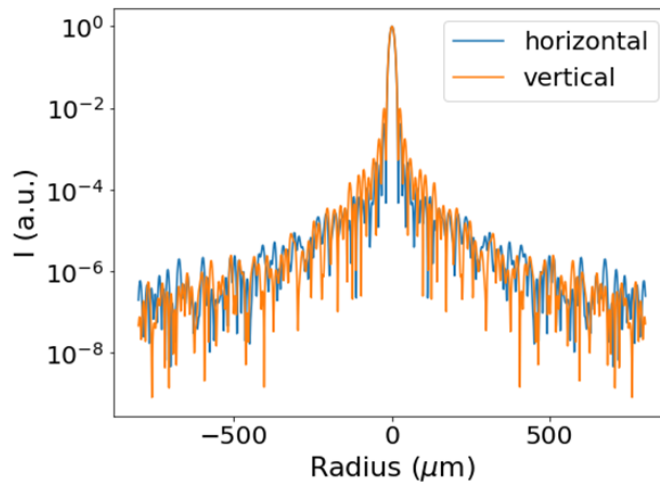


Figure 4.8: the calculated dynamic range of the focal spot over a larger radius

4.6.1 Spectrum

At the same time of taking the image of the near field, the on-shot spectrum is obtained simultaneously by using a spectrometer for each same shot, as the blue solid curve plotted in Fig.4.9.

However, the spectrum acquired by the spectrometer does not precisely match the spectral distribution of photons captured on the CCD chip. This is because the various optical elements in between exhibit various responses to different wavelengths, which inevitably results in spectral alteration, for instance, the beamsplitter, the achromatic lens, and ND filters on the CCD, as shown in the setup sketch in Fig.5.1. Fig.4.10 plots the transmission rate $T_{ND}(\lambda)$ of the neutral density (ND) filters mounted in front of the camera, the transmission $T_{BS}(\lambda)$ and reflection rates $R_{BS}(\lambda)$ of the beamsplitter, and the transmission rate of the achromatic lens $T_L(\lambda)$. Additionally, the quantum efficiency $QE(\lambda)$ of the CCD chip also varies across different wavelengths, as presented in Fig.4.10(a). To obtain an accurate spectrum, these wavelength response curves must be accounted for. The re-calibrated spectrum of the pulse on the CCD chip is obtained and plotted in the orange curve in Fig.4.9. The spectral distribution of the NF detected by CCD $I_{NF}(\lambda)$ is retrieved from the spectrum $I_{spec}(\lambda)$ measured by the spectrometer as the beam path difference includes the CCD2, ND filters in front, the beamsplitter, the achromatic lens, and another beamsplitter and finally the beam is

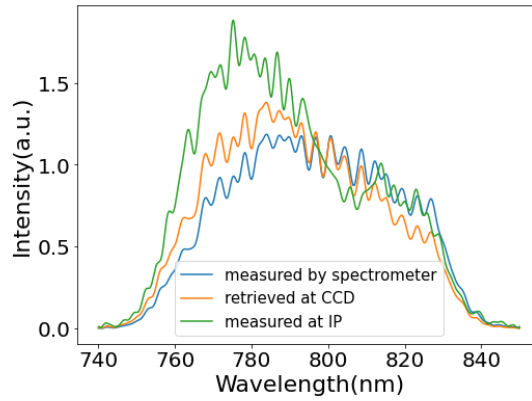


Figure 4.9: The blue curve is the spectrum measured by the spectrometer, the orange curve is the spectrum corrected for the pulse detected by CCD2, and the green curve is the spectrum measured at the interaction point.

detected the spectrometer: $I_{NF}(\lambda)/[QE(\lambda)T_{ND}(\lambda)R_{BS}(\lambda)] \cdot T_{BS}(\lambda) \cdot T_L(\lambda) \cdot R_{BS}(\lambda) \cdot T_{CC}(\lambda) = I_{spec}(\lambda)$

Furthermore, to accurately determine the energy of the laser pulse at the interaction

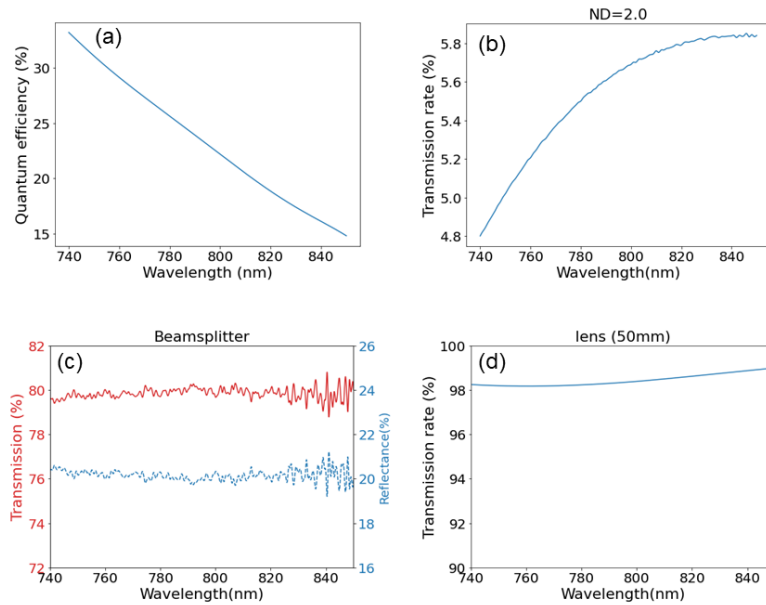


Figure 4.10: (a) The quantum efficiency curve of the CCD camera. (b) the transmission rate of each wavelength for the ND filter with ND=2.0. (c) the transmission rate and reflection rate of the beamsplitter. (d) the transmission rate of the achromatic lens with $f=50$ mm.

point, it is necessary to calibrate the spectrum measured at the diagnostic table. This

is achieved by simultaneously measuring the spectra at both the diagnostic table and the interaction point for the same pulse, as illustrated by the green curve in Fig.4.9. By obtaining the ratio of each wavelength from these measurements, the on-target spectrum and energy on a shot-to-shot basis can be inferred using only the measurement at the diagnostic table. This calibration ensures precise energy determination at the interaction point.

4.6.2 Calculation of Energy

The pulse energy received by the CCD2 camera for NF image can be calculated by the following steps. The diagnostic system uses the CCD2 camera with a bit depth of 14 bits and a saturation capacity of $18900 e^-$. This yields a sensitivity of $1.1 e^-$ per grayscale level. To obtain the total number N_{e^-} of electrons converted from the photons and read out by the CCD2, the values of all pixels in the NF image are summed after eliminating the noise. With amplitude information of each spectral component captured by the spectrometer and calibrated for the camera, the ratio $r(\lambda)$ of the number of electrons for each wavelength to the total number can be obtained. The photon number $n(\lambda)$ of each spectral component is $n(\lambda) = r(\lambda)N_{e^-}$. Using the Planck constant h and the speed of light c , the spectrally-resolved energy can be determined by:

$$E(\lambda) = \frac{hc}{\lambda}n(\lambda) \quad (4.4)$$

The total energy can be obtained by integrating over all wavelengths, $E = \int E(\lambda)d\lambda$, yielding $E = 0.012 \mu J$ detected by CCD as the NF image in Fig.4.3. The inferred energy before the laser enters the diagnostic system is $123.6 \mu J$. The average energy measured by an energy meter at this position is $122 \mu J$, with an uncertainty of $\pm 3\%$. This calculation method provides a precise measurement of the energy of the laser pulse at the diagnostic table, which can be used to obtain the high-precision on-target energy.

4.7 Characterization of Pulse Temporal Profile

The electric field of a laser pulse in the temporal domain can be written as:

$$E(t) = A(t)\exp[i(\phi(t) + \omega_0 t)] \quad (4.5)$$

It can be obtained by taking the inversed Fourier transform of the electric field in the spectral domain:

$$E(t) = \mathcal{F}^{-1}\{E(\omega)\} \quad (4.6)$$

with

$$E(\omega) = A(\omega)\exp[-i\varphi(\omega - \omega_0)] \quad (4.7)$$

As a result, $E(t)$ can be obtained by measuring the pulse spectrum with $A(\omega) \propto \sqrt{I(\omega)}$ and the spectral phase $\varphi(\omega - \omega_0)$.

4.7.1 Self-Referenced Spectral Interferometry

Self-Referenced Spectral Interferometry (SRSI) is a technique used for high-precision measurement of the spectral phase and intensity of optical pulses. It involves generating a reference pulse with a flat spectral phase and a broad spectrum collinearly from the pulse to be measured, utilizing cross-polarized wave generation (XPW). XPW is a third-order nonlinear process that rotates the polarization by 90 degrees and broadens the spectrum, thereby suppressing higher-order spectral phases and thus shortening the pulse duration, as expressed in Eq. 4.8:

$$E_{ref}(t) \propto |E_{in}(t)|^2 E_{in}(t). \quad (4.8)$$

where E_{in} is the electric field of the incident beam. The interferogram produced by the two pulses spectrally interfering with each other at the sensor chip of the spectrometer is then analyzed using Fourier-Transform Spectral Interferometry (FTSI) to retrieve the temporal profile and spectral phase. SRSI provides high-dynamic range intensity measurements of over 40 dB, with the XPW process enhancing the temporal contrast. This method requires no beam splitter or delay line, and offers single-shot, real-time pulse duration measurement at rates up to 10 Hz.

The scheme of SRSI is depicted in Fig. 4.11. The incident laser's polarization is ini-

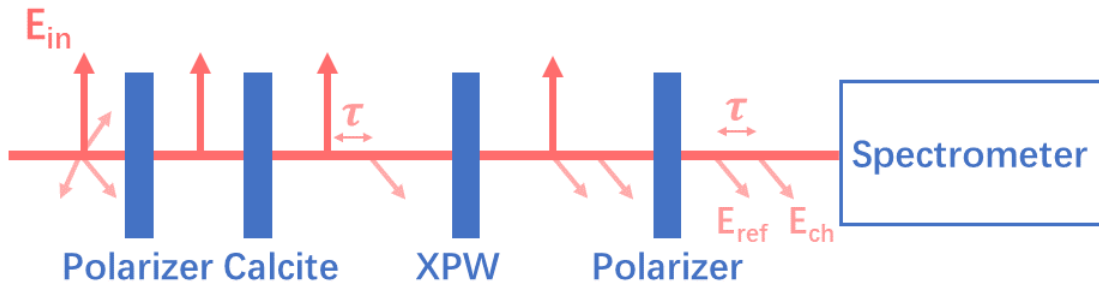


Figure 4.11: The figure shows the scheme of the optics inside the device Wizzler.

tially cleaned by a polarizer, followed by a calcite plate that generates a replica of the input beam with perpendicular polarization and introduces a delay τ . The reference beam is generated by focusing the laser to an XPW crystal made of Barium fluoride. A second polarizer is used to filter out the incident beam. Finally, the spectrometer captures the interferogram of the two pulses- the replica and the reference beam- with a delay of τ . The FTSI algorithm is utilized to retrieve the temporal profile and spectral phase from the obtained interferogram. With the retrieved results, the pulse's spectral phase can be further optimized and iteratively improved by providing feedback to the Dazzler, leading to highly improved temporal profiles.

Fourier-transform spectral interferometry (FTSI) is employed to retrieve the spectral phase of an ultrashort pulse. The interferogram obtained through FTSI is subjected to inverse Fourier transformation and filtering of terms other than the interference term with the positive delay. The peak centered at $t = \tau$ is then extracted and Fourier transformed to yield $f(\omega)e^{i\omega\tau}$. The process and the final results of FTSI for spectral phase retrieval are shown in Figure 4.12.

To model a chirped pulse in the time domain, dispersions, with $D_2 = 100\text{fs}^2$ and $D_n = 0$ for $n \neq 2$, are added to the spectral phase of a super-Gaussian spectrum with a central wavelength of 800 nm and an FWHM spectrum width of 80 nm. The FWHM duration of the input pulse E_{ch} is 21.2 fs. The reference pulse denoted as E_{ref} is obtained after the input pulse transmits through the XPW crystal using the Eq.4.8. Its FWHM duration is 12.4 fs with a flat spectral phase and broader spectrum width.

Both the incident and reference pulses in the temporal domain are plotted in Figure 4.12(a). The two pulses are temporally separated by a delay τ of 1.0 ps and spectrally interfere with each other when detected by a spectrometer, with the interferogram

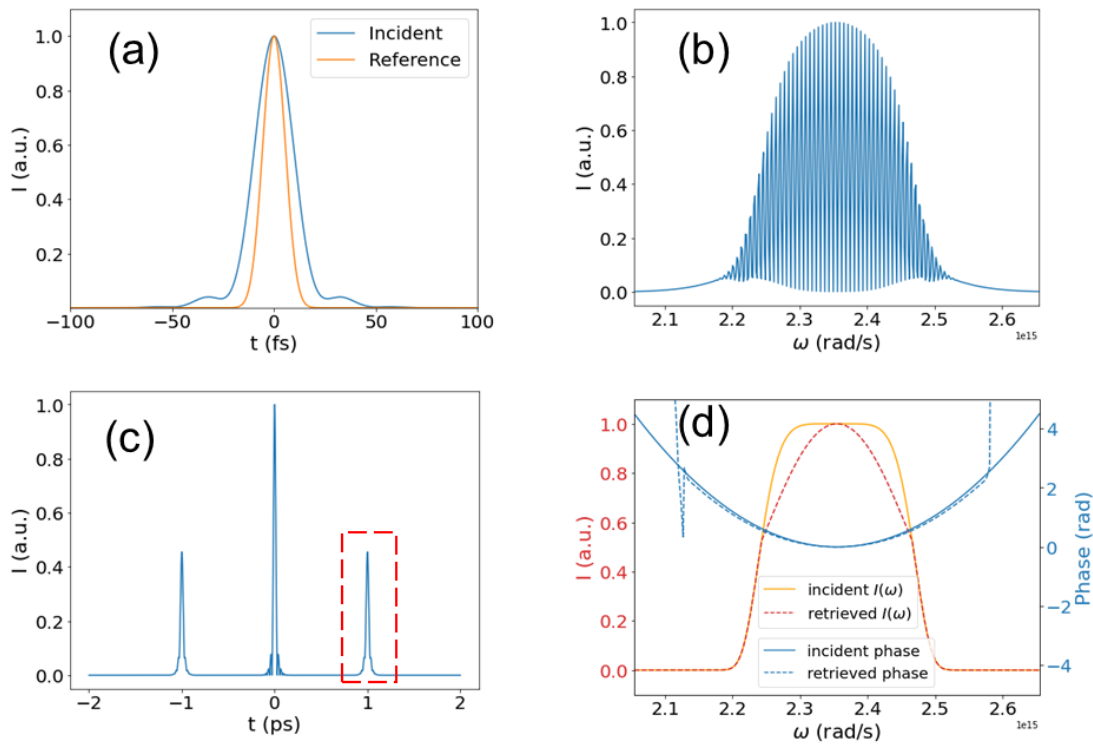


Figure 4.12: The figures show the steps involved in the FTSI technique to retrieve the spectral phase of an ultrashort laser pulse. (a) the blue curve represents the intensity of the pulse to be characterized I_{ch} with $D_2 = 100 \text{ fs}^2$. The orange curve represents the reference pulse intensity I_{ref} . (b) depicts the interferogram of the two pulses that interfere spectrally. (c) shows the temporal profile obtained by taking the Fourier transform of the interferogram. (d) the retrieved spectral phase and spectrum compared to the incident pulse to be characterized .

shown in Figure 4.12(b). The inverse Fourier transform of the interferogram is plotted in Figure 4.12(c), and the two subsidiary peaks are centered at $t = \pm\tau$, respectively. Each peak represents the conjugate interference term of the two pulses. The spectral phase is retrieved by taking the FT of the right peak and extracting its angle information. The retrieved phase (dashed blue curve in Figure 4.12(d)) agrees well with the phase defined for the input chirped pulse (plotted in solid lines) within the spectral range of interest, and the polynomial fitting of the retrieved phase also gives a result of $D_2 = 100 \text{ fs}^2$.

The temporal profile of the retrieved pulse is obtained by taking the Fourier transform of the retrieved spectrum and the retrieved spectral phase and the result is plotted in Fig.4.13. the pulse duration are the same The retrieved pulse overlaps with the

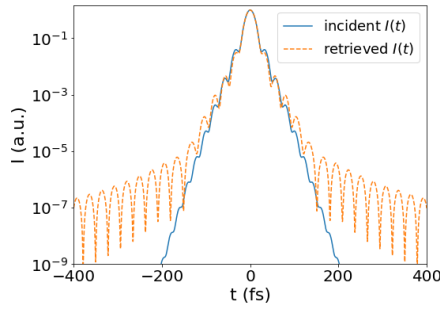


Figure 4.13: the temporal profile of the retrieved pulse and the incident pulse

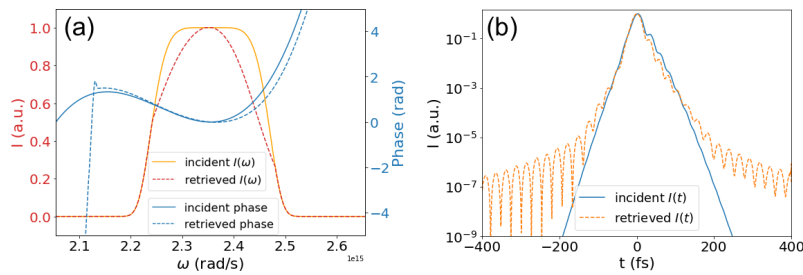


Figure 4.14: The result of FTSI of an incident pulse with large dispersion.

incident pulse down to order of 10^{-3} , with the RMS of the difference being less than 0.1% which is negligible.

However, the accuracy of this method can be affected when the incident pulse has greater spectral phase dispersion. If the reference pulse, generated from the incident pulse, is not ideal, the retrieved parameters can exhibit larger discrepancies from the true parameters of the pulse being characterized. For instance, the calculation result of FTSI with an incident pulse having the same spectrum but different spectral phase ($D_2 = 200 \text{ fs}^2$ and $D_3 = 2000 \text{ fs}^3$) is plotted in Fig.4.14. The polynomial fitting of the retrieved spectral phase gives $D_2 = -4000 \text{ fs}^2$ and $D_3 = 2000 \text{ fs}^3$. The pulse duration is 24.9 fs, while the incident is 24.1 fs. The intensity deviation starts at the order of 10^{-1} , with the RMS of the difference being 1.5%.

In conclusion, this method is effective for pulses with low spectral phase dispersion. However, as shown in the second case with greater spectral phase dispersion, the difference becomes more pronounced. The retrieved spectral phase and pulse duration significantly deviate from the actual values, which impacts the precision of the intensity measurements. Before measuring pulses using this techniques, the spectral phase should be optimized to approach Fourier transform limit to improve the measurement accuracy.

4.7.2 Results

To compensate for dispersions and recreate a pulse with the same spectral phase as at the interaction point, a pair of chirped mirrors is employed. These mirrors offer a dispersion compensation of -400 fs^2 per reflection. Notably, the steering mirror, constructed from glass through which the pulses propagate, introduces a dispersion of 1080 fs^2 over its 3 cm thickness, in addition to the GDD contributed by other optical components along the pulse path. By arranging the chirped mirrors in a face-to-face configuration to facilitate four reflections, a total compensation of -1600 fs^2 is achieved. The result of the SRISI measurement using the commercial device Wizzler from Fastlite is plotted in Fig.4.15.

The measured temporal profiles, with limited chirp ranges of D_2 within $\pm 400 \text{ fs}^2$

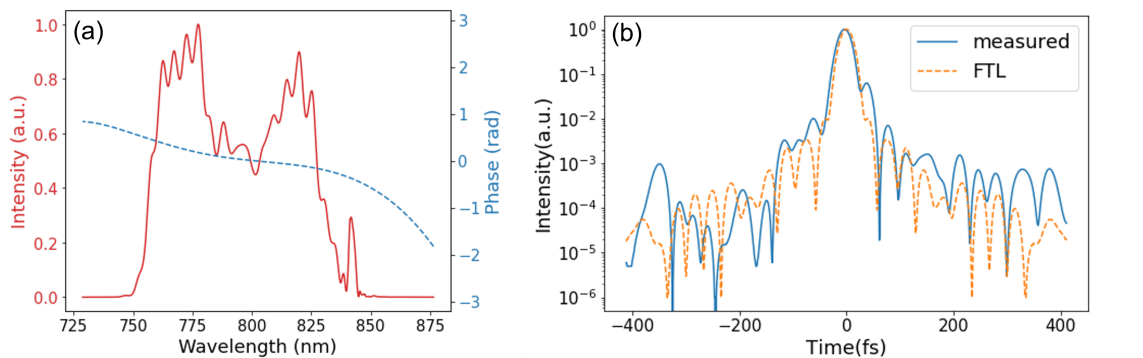


Figure 4.15: Ultrashort pulse temporal profile measured by SRISI (a) The spectral domain plot, including the spectrum intensity distribution alongside the spectral phase (b) The temporal profile of the pulse, retrieved from the spectral data, and the corresponding Fourier transform limit.

and D_3 within $\pm 4000 \text{ fs}^3$, are represented in Fig.4.16(a). However, when the incident beam exhibits significant dispersions, it will result in the reference beam without a flat spectral phase, ultimately leading to measurements with diminished accuracy. Conversely, when the same spectrum is utilized to compute the pulse duration with varying spectral phases, the calculated outcomes are shown in Fig.4.16(b), covering a broader range of D_2 and D_3 values. This comparison shows the limitations imposed by the SRISI technique on the measurement's accuracy and it can deliver a measurement with an error of approximately 0.2% on the pulses close to FTL [92].

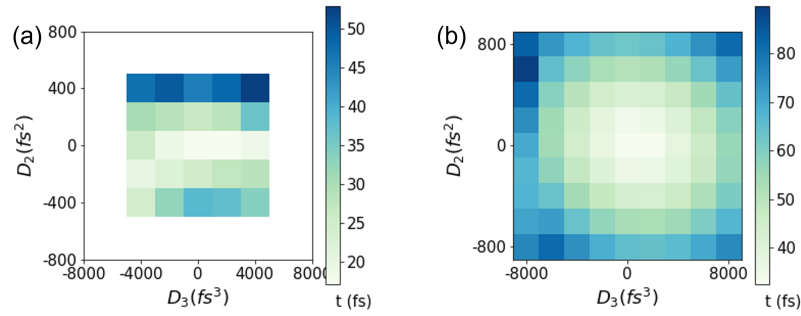


Figure 4.16: (a) The pulse durations measured by Wizzler vary with different values of GDD (D_2) and TOD (D_3) values introduced into the spectral phase by the Dazzler. These measurements by the Wizzler tend to be less reliable when spectral phase aberrations are significant, leading to a loss of accuracy. (b) The calculated pulse durations, utilizing the same spectral input as the measured one by the Wizzler, offer an extensive assessment of the pulse duration with more significant chirps.

4.8 Temporal Contrast

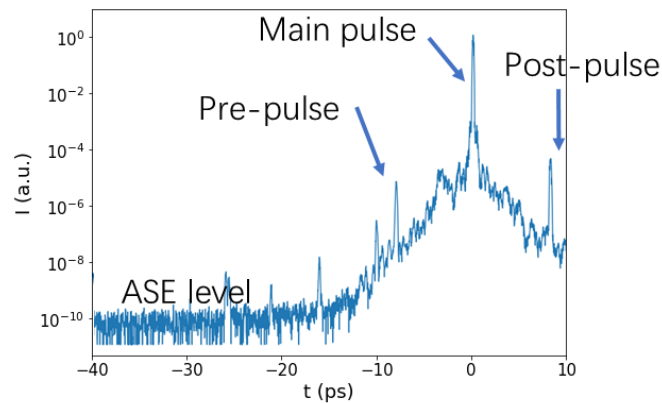


Figure 4.17: The temporal contrast measured. The maximum dynamic range reaches below the order of 10^{-11} within the time frame of 50 ps.

In addition to the temporal profile measurement of the main pulse, temporal intensity contrast over a longer time scale is another crucial parameter for precision intensity measurement. The energy from the pre-pulse, post-pulse, and amplified spontaneous emission (ASE) may go undetected in diagnostics with a low dynamic range and a small time window. This portion of energy should be subtracted from

the total energy to precisely calculate the laser intensity, ensuring that the measurement aligns with the high precision required for accurate experimental results. The pre-pulses comparable in duration to the main pulse but occurring on picosecond timescales, can result from optics in wrong orientation or nonlinear mixing processes of post-pulses. ASE originates from fluorescence emitted from the amplifying materials during various amplification stages of the laser[82].

The temporal contrast of high-intensity laser pulses is measured by a third-order cross-correlation interferometer by using the commercial device called Sequoia from Amplitude, with a dynamic range greater than 10^9 and a temporal span of 500 ps. The plot in Fig.4.17 focuses on a measurement within a 50 ps window, with ASE level, pre-pulse, post-pulse and main pulse indicated in the plot, providing a comprehensive overview of the pulse dynamics. The measurement was conducted with a step size of 17 fs, aggregating 5 shots per data point. The total dynamic range exceeds 10^{11} . The ratio of the energy less than 10^{-2} compared to the total energy accounts for 0.47%. This portion of energy should be subtracted from the total energy to precisely calculate the laser intensity.

4.9 Laser Stability

To evaluate the stability of a high-power laser system, a comprehensive measurement of 500 consecutive shots has been conducted. This approach allows for a detailed analysis of the laser's performance consistency over a significant number of cycles. By examining parameters such as pulse energy, duration, beam profile, and temporal contrast across these shots, variations and trends can be identified, providing insights into the system's reliability and operational stability. The statistical analysis of 500 consecutive laser shots, as depicted in Fig.5.7, characterizes the stability of the laser parameters. The results are:

- Energy: (With the first pump laser Titan 600 mJ), the mean energy output is measured at 282 mJ, with an RMS of 4%.
- Pulse Duration: The average pulse duration is 22.6 fs, with an RMS of 0.4%.
- Fluence of Focal spot: The fluence is calculated by averaging the pixel values within FWHM of the focal spots. The RMS of the fluence is 4%.

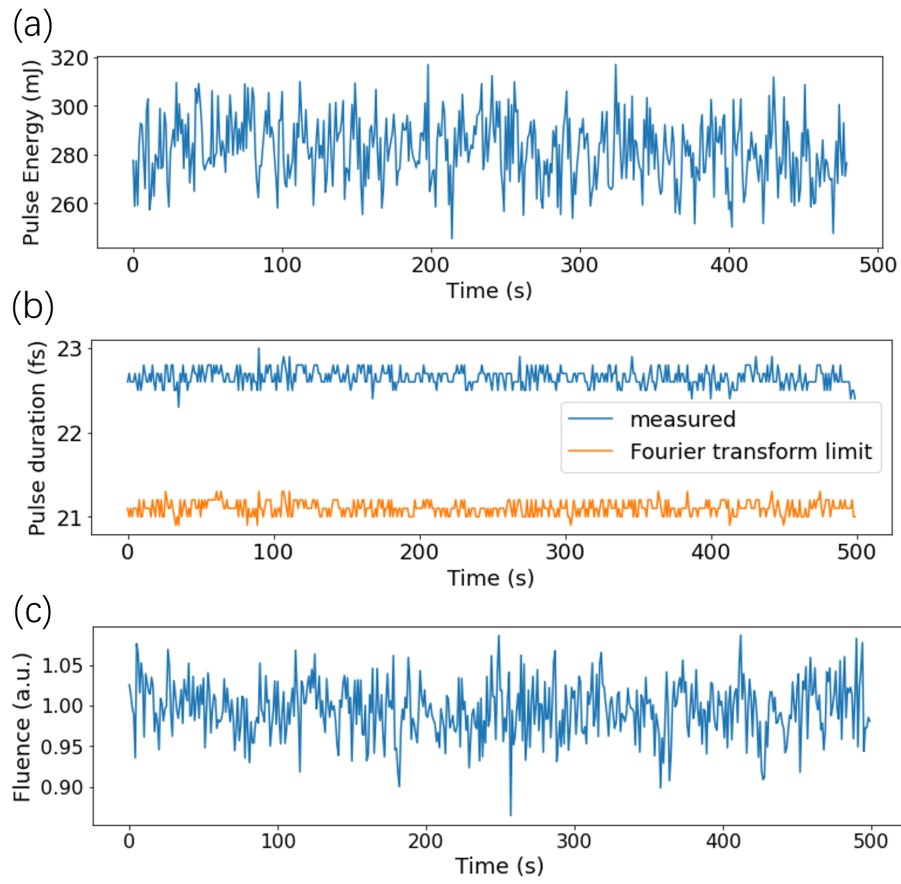


Figure 4.18: the measurement results of 500 laser shots taken consecutively of (a) the pulse energy, (b) the pulse duration, and (c) the fluence.

Fig.4.19 illustrates the Allan deviation for the measurement of energy (E), pulse FWHM duration (τ), and the average fluence within FWHM (F) over 500 consecutive laser pulses. The Allan deviation provides insight into the stability and precision of these measurements over time.

The solid red line indicates the Allan deviation for the measured energy, while the dashed line represents the fitted trend with a slope (k) of -0.94 . The trend shows that the measurement noise decreases as the number of averaged pulses increases, following a nearly perfect -1 slope, characteristic of white noise. This suggests that the energy measurements are primarily affected by random fluctuations, and averaging more pulses significantly reduces the measurement error.

The yellow curve shows the Allan deviation for the pulse duration, with the solid line the measured data, and the dashed line the fitted trend with $k=-0.94$, similar to the energy.

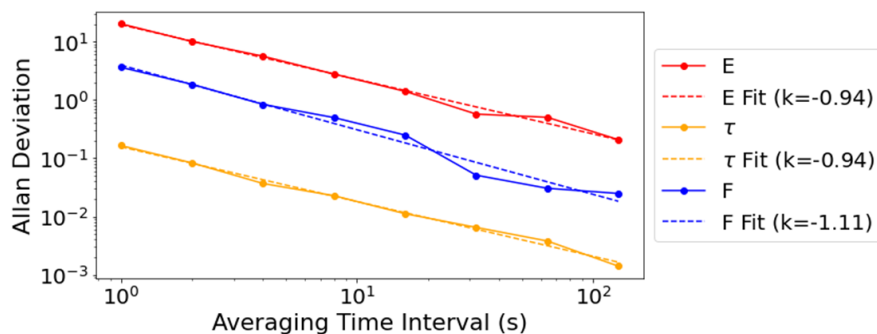


Figure 4.19: Allan deviation of the measured energy, pulse duration and fluence

The blue curve is for the fluence, with the solid line the measured data, and the dashed line the fitted trend with $k=-1.11$. The slope of -1.11 is slightly steeper than -1 , suggesting that the fluence measurement noise decreases slightly faster than white noise with the number of averaged pulses. This indicates that there might be some systematic noise sources being averaged out more efficiently than random noise.

To identify the causes of fluence fluctuations in high-power laser operations, further measurement and analysis are undertaken. This approach examines the laser parameters—such as phase shifts, energy stability, and beam profile consistency—to quantify the factors influencing fluence variations.

The fluence measurements were performed in air, where air currents and mechanical vibrations might affect the wavefront, leading to fluence fluctuations. To address this, the focal spot was measured in air and in vacuum simultaneously by employing a beamsplitter as illustrated in Fig.4.20. Both CCD cameras are ensured to image the same focal plane, allowing for a comparative analysis of the focal spot's behavior under different environmental conditions.

The results are presented in Fig.4.21. (a) is the average fluence within FWHM. In vacuum conditions, the RMS of F is 3.7%, while the RMS of F in air is 4.1 %, indicating a contribution from environmental disturbance to the focal spot fluence. It is crucial to perform the measurements of focal spot intensity in a vacuum chamber to improve the precision.

As the energy of each pulse fluctuates from shot to shot, the influence of energy on focal spot fluence is analysed by normalizing the average fluence to the energy of each shot. Fig.4.21(b) displays the relative energy obtained by taking the sum of the values in focal spot images. The RMS is 2.6% for both energies measured in air and in vacuum. It's notable that this RMS of energy differs from the RMS reported

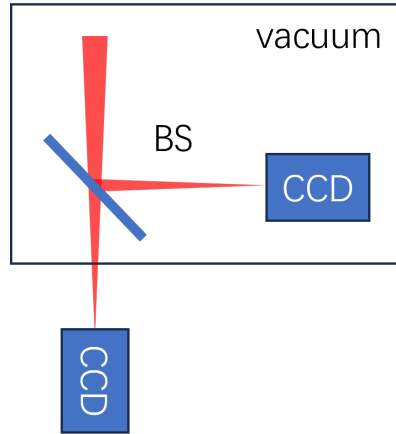


Figure 4.20: The experimental setup is designed to simultaneously measure the focal spot of each laser shot in both vacuum and air environments, utilizing two CCD cameras that are identical models, and ensuring that they are capturing the same focal plane.

in Fig.5.7(a). While measuring at the focal spot, attenuation is utilized to prevent camera chip saturation, albeit at the cost of low dynamic range data. Moreover, these measurements use the laser system's front end, unlike those in Fig.5.7(a) which include the front end and the first pump laser.

By dividing the averaged fluence to the energy of each shot to eliminate the impact of energy on fluence, as shown in Fig.4.21(c), the RMS of the normalized fluence $\langle F \rangle / E$ is reduced to 3.0% for measurements in air, and 2.7% for vacuum.

Although the stability of fluence improves by 34%, from 4.1% to 2.7%, by mitigating the effects of energy jitter and environmental factors, fluence fluctuations persist.

To further understand the fluence fluctuations, the wavefront of each laser shot was analyzed. The aberrations in the wavefront, even after optimization with a deformable mirror, can be attributed to a variety of factors that persistently cause shot-to-shot fluctuations. These include air currents and vibrations in the laser front end, as well as refractive index fluctuations within the amplifier caused by stochastic intensity variations in the pump profile.

The measurement of wavefront was conducted over 1000 consecutive shots at the repetition rate of 1 Hz and the results are plotted in Fig.4.22. The mean values of the PtV and RMS are 0.65λ and 0.08λ , respectively, and the respective RMS of each is 7.9% and 9.9%. The RMS of the Strehl ratio, as shown in Fig.4.22, is 2.6%, aligning closely with the observed fluence fluctuation of 2.7%. This consistency between the Strehl ratio and fluence fluctuation confirms the impact of wavefront aberrations on

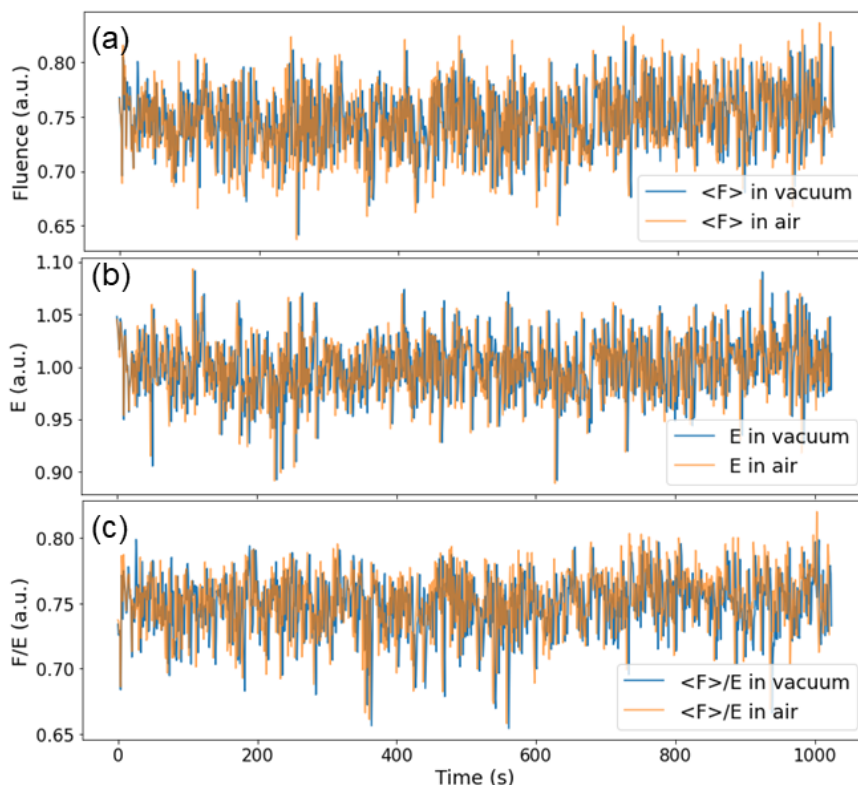


Figure 4.21: The measurement results of the focal spot in air and in vacuum simultaneously for more than 1000 shots consecutively. (a) the energy, (b) the average fluence within FWHM, and (c) the fluence normalized to the energy of each laser pulse.

the laser's focal performance.

By decomposing the measured wavefront into Zernike polynomials, one can assess the contribution of each type of aberration to the overall wavefront distortion. The decomposition of wavefront for each shot into six key terms—astigmatism at 0 and 45 degrees, coma in the X and Y directions, and trefoil at 0 and 30 degrees—is plotted in Fig.4.23 and the corresponding numerical results are presented in Table4.1. The data reveals that astigmatism at both 0 and 45 degrees are the predominant aberrations. During the process of wavefront optimization, repeated attempts have been made to minimize aberrations to achieve the desired laser beam quality. Despite numerous iterations, a residual astigmatism persisted. This residual aberration indicated that the optimization process had reached a point where further improvements were no longer possible.

The wavefront aberrations not only contribute to shot-to-shot fluence fluctuations,

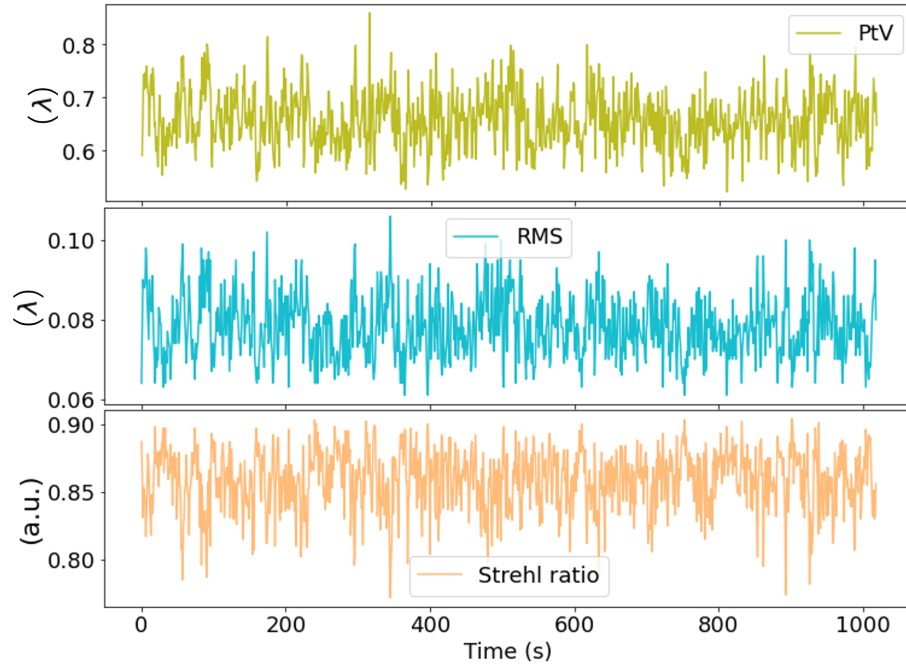


Figure 4.22: The PtV, RMS of the wavefront, and the Strehl ratio over 1000 consecutive shots at the repetition rate of 1 Hz

but also affect various characteristics of the focal spot. A comprehensive analysis includes the centroid's coordinates, which correspond to the beam pointing jitter, the $D4\sigma$ diameter, and the Q factor—defined as the ratio of energy encircled within the FWHM to the total energy of each focal spot. These parameters are crucial for evaluating the beam's quality and stability. The results are depicted in Fig.4.24 and the numerical analysis of each parameter is listed in Table4.2.

From the numerical results in Table4.2, the observed asymmetry in the focal spot diameters, featuring a larger $D4\sigma_x$ of $34.2 \mu m$ and a deviation of $0.5 \mu m$ in the x-direction, contrasts with the y-axis measurements with a $D4\sigma_y$ of $29.9 \mu m$ and a standard deviation of $0.3 \mu m$. Additionally, a more pronounced pointing jitter along the x-axis with a standard deviation of $13.7 \mu m$ compared to $6.2 \mu m$ along the y-axis, further underscores this asymmetry.

In addition to the observed shot-to-shot fluctuation, a drift in beam pointing in both x- and y-directions has been witnessed from the plot in Fig.4.24(b). Efforts to stabilize beam pointing are currently underway by colleagues at JETi200.

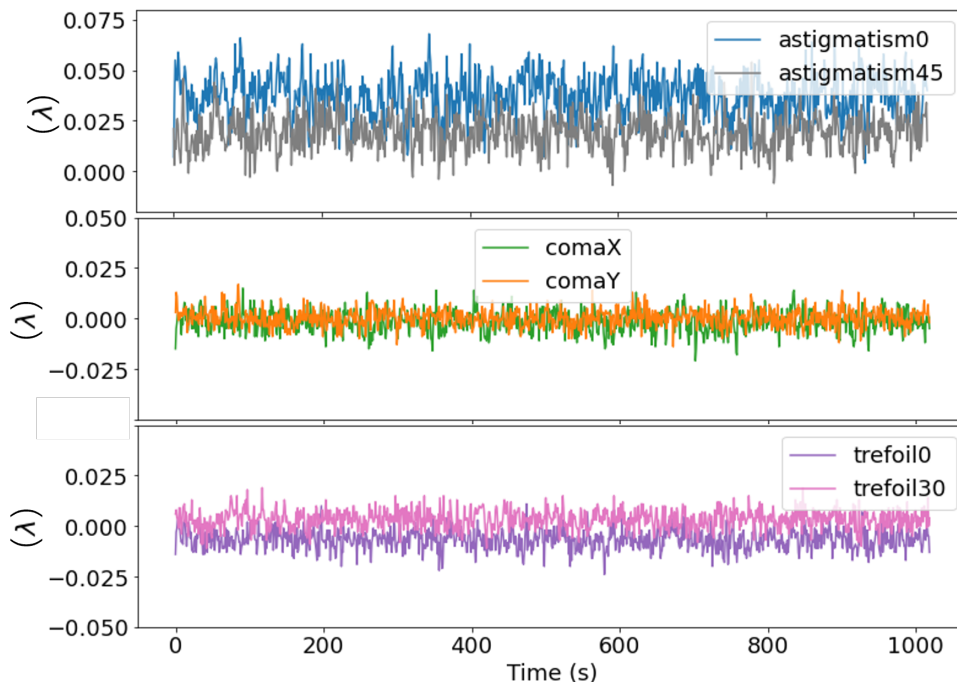


Figure 4.23: Zernike decompositions of the wavefront for each laser shot, highlighting the six principal terms impacting the focal spot profile

The RMS of the Q-factor is $2.8\% = 1.4\%/49\%$ according to the results in Table 4.2. It indicates a relatively stable Q-factor, suggesting that the focal spots are of good quality. The RMS of Q with 2.8% aligns with the observed fluence fluctuation of 2.7%, indicating the Q-factor's effectiveness in predicting and reflecting the stability of the focal spot.

In conclusion, the peak fluence of the focal spot is the predominant factor influencing shot-to-shot intensity fluctuations. After accounting for energy variations and doing the measurement in a vacuum chamber to eliminate environmental disturbances, it becomes clear that these fluctuations are primarily due to wavefront aberrations that vary from shot to shot. The decomposition of the wavefront into Zernike polynomials reveals that astigmatism 0 degree plays a significant role, impacting the focal spot size.

In Chapter 6, the three-dimensional characterization of the focal spot will be discussed, revealing the influences of spatio-temporal couplings on the focal spot. This characterization is essential for understanding focal spots with larger diameters compared to the diffraction limit and for achieving more precise focal spot intensity measurements.

	Mean value (± 0.01) [λ]	Standard deviation [λ]
Astigmatism 0°	0.04	0.01
Astigmatism 45°	0.02	0.01
Coma X	0.00	0.01
Coma Y	0.00	0.01
Trefoil 0°	-0.01	0.02
Trefoil 30°	0.00	0.01

Table 4.1: Numerical analysis of wavefront aberrations - mean values and standard deviations of the Zernike polynomial coefficients.

	Mean value	Standard deviation
$D4\sigma_x$ [μm]	34.2	0.5
$D4\sigma_y$ [μm]	29.9	0.3
Centroid X [μm]	0	13.7
Centroid Y [μm]	0	6.2
Q	49%	1.4%

Table 4.2: The mean values and standard deviations of the $D4\sigma$ diameters in x- and y-directions, the coordinates of the centroid of focal spots, and the Q factor.

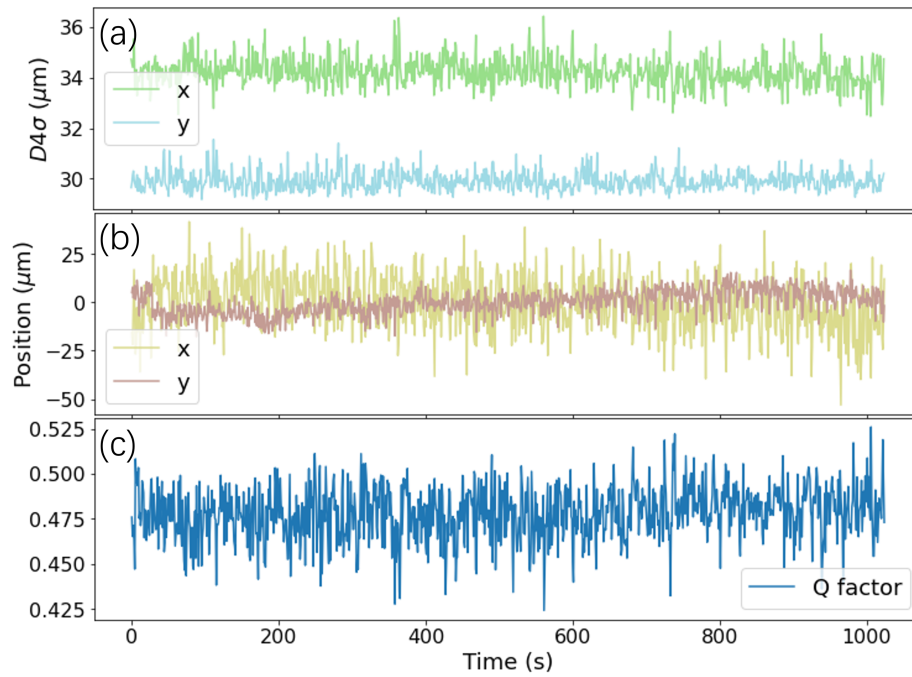


Figure 4.24: (a) The $D4\sigma$ diameter, (b) the coordinates of the centroid, and (c) the Q factor of the 1000 shots

5 Laser Intensity Tagging Using Nonlinear Optical Process

To tag the intensity of a laser pulse a second-order non-linear process, SHG is used, which depends quadratic on the intensity. In the all-optical setup, a near-infrared (NIR) laser pulse is focused into a thin beta-barium borate (BBO) crystal and image the focal spot of the fundamental beam and its frequency-doubled replica onto a CCD. In the regime of low conversion rates of SHG, specifically less than 0.1% in this experiment, only a small amount of the energy of the fundamental beam is converted to the SHG beam, where the depletion of the fundamental beam can be ignored and its intensity can be considered constant over its propagation through the thin SHG medium. The generated 2ω pulse intensity is proportional to the square of the intensity of the fundamental beam. Laser intensity fluctuations can lead to changes in the conversion rate of SHG. The ratio R , defined as $R = \sqrt{F_{2\omega}}/F_{\omega}$, where fluence F is given by $F = dE/dA$, can be obtained by capturing the focal plane images of both the fundamental and SHG beams. This ratio, comparing the fluences of the fundamental and the second harmonic pulses, can be used as a reference for on-shot intensity tagging to verify the peak fluence diagnostic. Changes of R across the transversal plane indicate that the wavefront aberrations cause the variations in focal spot profile. Furthermore, R increases as shorter pulses improve the conversion efficiency for a given pulse energy. By calibrating R against different temporal profiles, precise relative duration tagging can be achieved. This non-linear diagnostic system can be implemented in high-power laser systems by utilizing the leak light through a steering mirror, thereby monitoring the on-shot peak intensity.

5.1 Experimental Setup

The experiments were carried out with the JETi-laser system at the Institute of Optics and Quantum Electronics in Jena. The experimental setup, which generates the SHG and images the focus in the crystal onto the CCD simultaneously, is depicted in figure 5.1. The beam is first splitted by a beam splitter (BS1). For the reflected part,

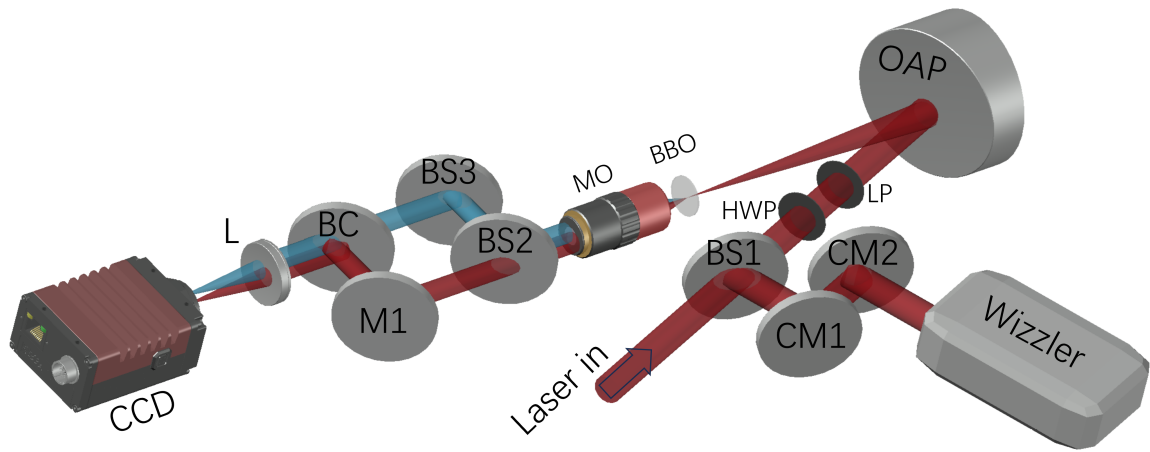


Figure 5.1: Laser intensity tagging system: For the beam reflected by BS1 (beam splitter), its spectral phase is compensated by the chirped mirrors (CM1 and CM2) and its temporal duration is measured by a Wizzler. The beam transmitted through BS1 passes through a half-wave plate (HWP) and thin linear polarizer (LP), allowing for continuous energy tuning. A thin BBO crystal with a thickness of $10\ \mu\text{m}$ is positioned at the focal plane for SHG. An imaging system consisting of a microscope objective (MO) and an achromatic lens (L) images the same focal plane to a coupled-charge device (CCD) camera for the different colors.

a pair of chirped mirrors (CM1 and CM2) are used to compensate the spectral phase. Then the temporal profile of the fundamental beam is measured simultaneously for each shot via Self Reference Spectral Interferometry (SRSI, Fastlite, WIZZLER)[48]. For the beam transmitted through BS1, a polarizer (Thorlabs, LPNIRB100) with an extinction ratio $> 10^3$ at 800 nm is used to purify the laser polarization, allowing only the horizontal polarization component to pass through and filter out the perpendicular component. The input energy to the SHG crystal can be continuously tuned by rotating the half-wave plate (HWP) located before the polarizer. The laser beam is focused by an off-axis parabolic mirror (OAP) with a focal length of 444.5 mm. A thin BBO crystal with a thickness of $10\ \mu\text{m}$ is placed at the focal plane. The thickness of $10\ \mu\text{m}$ is chosen to ensure a low conversion rate of 0.1% and to avoid temporal walk-off [94, 95].

The imaging system consisting of a microscope objective (10X Mitutoyo Plan Apo NIR) and an achromatic lens is used to image the plane of the laser focal spot onto a CCD camera. The MO also provides reliable performance at the wavelength range of 400 nm. The CCD camera is Allied Vision GT1660.

To simultaneously record images of the fundamental focal spot and the 2ω focal spot on the same CCD chip, a beam-splitter (BS2, S1: AR(750-850nm) $<1\%$, S2: HR(375-425nm) $>99.8\%$, R(750-850) $<5\%$) is used that reflects the SHG beam at the rear surface and transmits the fundamental beam. A beam combiner (BC, S1: AR(380-430nm) $<0.25\%$, S2: HR(750-870nm) $>99.9\%$, R(360-480nm) $<5\%$) combines the two beams with a small spatial offset to be distinguishable on the CCD. The pulse temporal shape is manipulated by applying group-delay dispersion (GDD) and third-order dispersion (TOD) to the spectral phase by means of an acousto-optic programmable dispersive filter [84] (Fastlite, Dazzler), which is part of the JETi laser system to compensate for higher-order spectral phase aberrations.

5.2 Results and Discussions

First step is to confirm the same plane at the focal spot is imaged by both imaging paths, and the BBO crystal is placed at the focal plane.

Fig.5.2(a) displays the focal spot image focused by the scheme with $f/36$, with a full-width-half-maximum(FWHM) diameter of $35.7 \mu m$ while the diffraction limit is $35.1 \mu m$. Figure 5.2(b) shows the 2ω focal spot with an FWHM diameter of $22.2 \mu m$. This focal spot is a nonlinear copy of the fundamental one. In Figure 5.2(c), the blue curve is the lineout of the horizontal profile of (b) at $y=0$ and the red dotted curve is the squared of the lineout of the horizontal profile at $y=0$ (a). The two curves overlap, showing a quadratic relationship between each corresponding point in the transverse plane of the two focal spots, indicating that the wavefront is well optimized. The calculated Pearson correlation coefficient between the blue and the red dotted curves in Fig.5.2(c) is 1.00, indicating a strong positive linear correlation.

The high-resolution imaging system magnifies the focal plane by 16 times with a scale of $0.4 \mu m/\text{pixel}$. The FWHM area A of the focal spot is the pixel numbers whose values are larger than FWHM, and the precision on average is 0.80%. The precision of the relative energy encircled within the FWHM area depends on the total count number within this area, limited by the dynamic range of the CCD sensor with a bit depth of 14 bits, and the result gives 0.01%. The temporal duration measured by the technique SRSI with Wizzler contributes an error of 0.2% for close to Fourier transform pulses [92].

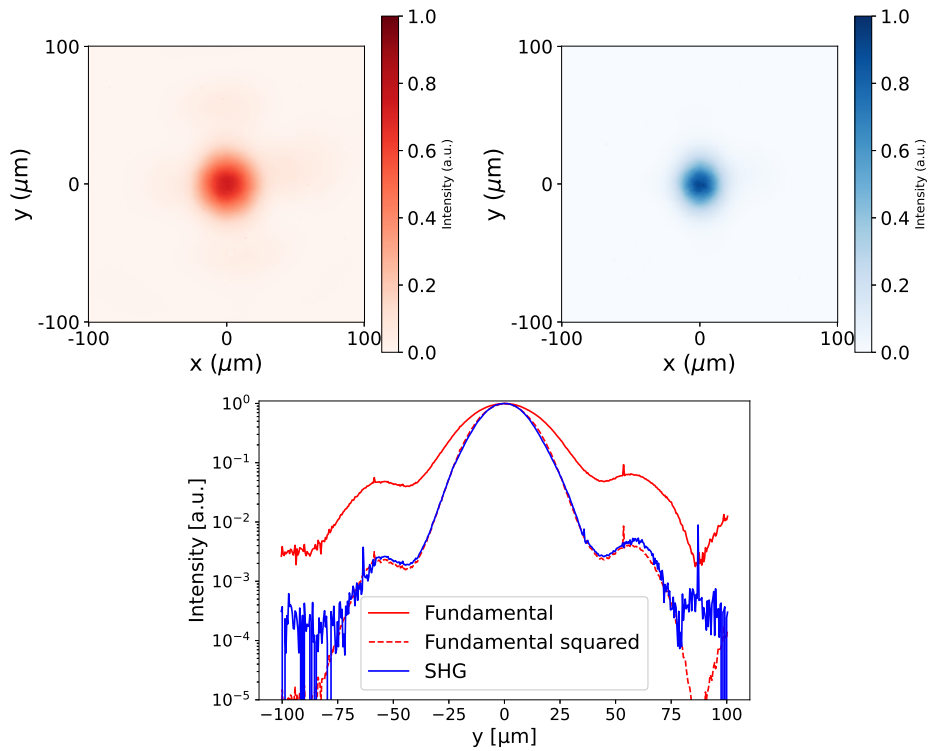


Figure 5.2: (a) The focal spot of the fundamental beam with an energy of 230 nJ. (b) the focal spot of the 2ω beam. (c) the lineout of the fundamental focal spot (solid red) and the 2ω focal spot (solid blue) in the log scale. To compare the two foci, take the red curve squared (dotted red) and it perfectly overlaps with the blue curve.

At low conversion rates, the undepleted pump approximation assumes that the fundamental beam's intensity remains constant within the nonlinear crystal and that the generated SHG beam is weak. The intensity of the SHG beam follows a quadratic dependence on the incident fundamental beam's intensity, expressed as $I(2\omega) \propto I(\omega)^2$. The fluence ratio R is supposed to remain constant and can serve as a reliable reference for on-shot, high-precision intensity tagging. As the input pulse energy increases and the conversion efficiency becomes significant, the depletion of the incident beam must be taken into account.

To determine the region of quadratic dependency, focal spot images of the fundamental and SHG beams at varying input laser energies are captured. By continuously tuning the energy via the rotation of the HWP while keeping the polarizer fixed, the intensity growth of the generated SHG beam is characterized. The results are plotted in Fig.5.3. The peak fluence of the SHG focal spot exhibits a quadratic increase with the rise in the fundamental laser energy, with a coefficient of $3.1e-6$. The residual

sum of squares of this quadratic fitting curve is 0.07, indicating a good fitting of the model to the data.

The ratio R of each laser pulse shot with a transform-limited temporal profile and

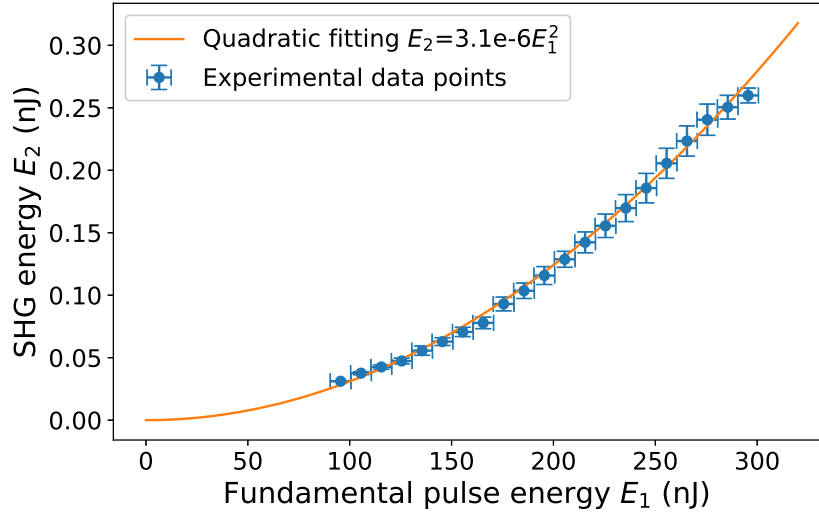


Figure 5.3: The figure shows the response of the SHG beam energy to the fundamental laser pulse energy. The overall results follow a quadratic curve, suggesting the quadratic relationship between the fundamental beam energy and the generated SHG beam energy in the low conversion regime.

a flat wavefront is expected to remain constant. A series of focal spot images are taken at the repetition rate of 5 Hz consecutively for more than 2000 shots with an input energy of 230 nJ, which is within the quadratic regime and the images has a signal-to-noise ratio of 37 dB. The peak fluence fluctuations are plotted in panel (a) in Fig.5.7 for both beams. For simplification, the fluences are normalized to their mean values respectively. The jitter of $F_{2\omega}$ relies on the statistical results of F_{ω} :

$$\frac{\sigma_{F_{2\omega}}}{\langle F_{2\omega} \rangle} = 2 \frac{\sigma_{F_{\omega}}}{\langle F_{\omega} \rangle} \quad (5.1)$$

where $\sigma_{F_{2\omega}}, \sigma_{F_{\omega}}$ are the RMSE of fluence of the SHG and the fundamental focal spots, respectively, and $\sigma_{F_{2\omega}}/\langle F_{2\omega} \rangle, \sigma_{F_{\omega}}/\langle F_{\omega} \rangle$ the RMSE normalized to their mean values. The normalized RMSE is 6% for the fundamental beam. The RMSE is 12% for the 2ω beam. The twice RMSE value of SHG beam compared to the fundamental beam accords with the expectation from Eq.5.1. The Q-factor, which is the ratio of energy encircled within the FWHM of the focal spot to the total energy, is also plotted in

Fig.5.7(b) for each shot. The RMS of the Q factor of the fundamental beam is 7.0%, which is very close to the RMS value of its fluence. The wavefront fluctuation from shot to shot contributes to the fluence jitter. The RMS of the Q factor is 7.5% for the SHG beam, smaller than its fluence RMS, indicating that not only the wavefront fluctuation but also the temporal profile contributes to such change.

In this study, the precision of intensity measurements is assessed through the exam-

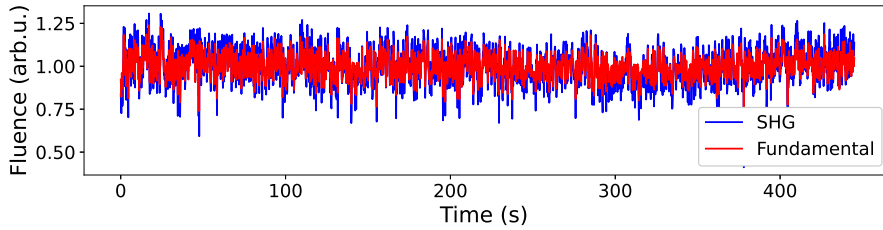


Figure 5.4: The peak fluence of the fundamental and the SHG focal spots taken consecutively for more than 400 s at a repetition rate of 5 Hz.

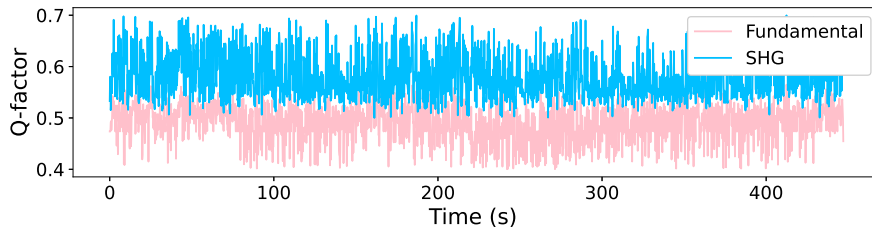


Figure 5.5: The Q-factor, which is the ratio of energy encircled within FWHM to the total energy, of both the fundamental and SHG focal spots.

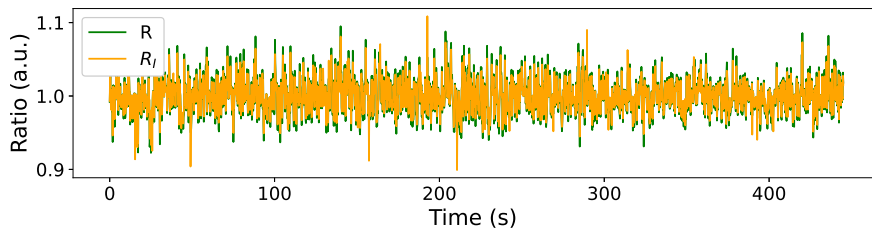


Figure 5.6: The fluence ratio R and the intensity ratio R_I of each shot.

ination of the ratio R for each laser pulse. Fig.5.7(c) shows that this ratio R remains consistently stable across the consecutive measurements, with an RMSE of 2.4%. This low value indicates higher precision. Even though this experimental setup is installed

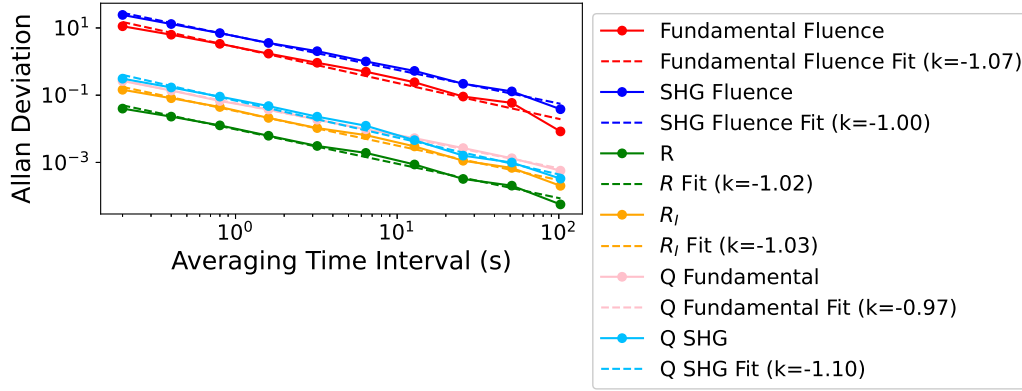


Figure 5.7: The Allan deviation.

inside a vacuum chamber and the disturbance of air current has been eliminated, the wavefront and spectral phase have shot-to-shot fluctuations, which consequently affect the pulse intensity distribution, thereby contributing to the jitter in the ratio R [96]. The temporal profile of the fundamental beam is measured simultaneously for each shot and the temporal profile of the second-order beam can be calculated from it. The ratio R_I between the intensities is defined as $R_I = \sqrt{I_{2\omega}}/I_\omega = R\tau_\omega/\sqrt{\tau_{2\omega}}$, where τ_ω and $\tau_{2\omega}$ are the temporal durations of the fundamental and SHG beams respectively. The corresponding R_I of each shot is also plotted in Fig.5.7(c) and its RMSE is 2.1%, which has been improved compared to that of R .

Spectral intensity and spectral phase jitters from shot to shot, resulting in jitters of temporal duration. To investigate the impact of temporal profile variations on the ratio R , the spectral phase is systematically modified. Chromatic dispersion is characterized by coefficients denoted as D_n , with D_2 representing the group delay dispersion (GDD) and D_3 the third-order dispersion (TOD). It degrades pulse temporal profiles and peak intensities, ultimately affecting SHG conversion efficiency. Specifically, D_2 contributes to a longer pulse duration and a significant reduction in pulse peak intensity, resulting in a quadratic decline in SHG conversion rate. D_3 asymmetrically broadens the laser pulse, and decreases the contrast between the main pulse peak and the sidelobes, increasing the sidelobes and lowering the peak intensity. To investigate these effects, different dispersions are applied by adjusting D_2 and D_3 using the Dazzler device in the CPA system to modify pulse temporal shapes while maintaining pulse energy and focus size constant. Fig.5.8(a) shows the experimental results of the ratio R with varying spectral phase. When setting the compensating dispersion to $D_2 = 0$ and $D_3 = 0$, the pulse temporal duration converges towards the bandwidth

limit of 20 fs FWHM. Consequently, the peak fluence of 2ω beam reaches its maximum value, yielding a normalized ratio R of 1.0. In the presence of D_2 and D_3 , the SHG peak fluence decreases, with the ratio varying according to the alterations in temporal profiles. In the laser diagnostics, analyzing the fundamental focal spot and its SHG nonlinear counterpart, the relative pulse duration can be inferred from this table of calibrated R . The corresponding R_I of different spectral phase aberrations is plotted in Fig.5.8(b), with τ_ω measured by the Wizzler of each shot and $\tau_{2\omega}$ derived from τ_ω . D_2 and D_3 have shot-to-shot fluctuations and will cause temporal duration fluctuations. The R and R_I of each shot plotted in Fig.5.7(b) with the Dazzler setting $D_2 = 0$ and $D_3 = 0$ underscore the ratio's sensitivity to pulse duration alterations. However, the temporal profile measurement has a higher precision when the pulse is close to the Fourier transform limit. When the incident beam exhibits significant chirp, this pulse duration is not accurate due to the intrinsic limitation of the nonlinear crystal in the Wizzler setup, which is intended to create a reference beam with flat spectral phase from the incident beam. This results in a reference beam with a non-flat spectral phase, ultimately leading to measurements with diminished accuracy. The R and R_I of each shot with the chirps setting of $D_2 = 400fs^2$ and $D_3 = -4000fs^3$ are plotted in Fig.5.8(c). The RMSE of R is 5.4% and the RMSE of R_I is 7.8%, indicating the precision limits in characterizing temporal profiles under varying dispersion settings.

In this work, an assessment of the precision of the laser focal spot intensity measurement using the nonlinear optical process of second harmonic generation is conducted. Such high precision is attained by the high-resolution imaging of the focal plane, the high-level count numbers on CCD chip and the control of spectral chirp within the range of $\pm 200fs^2$ for GDD and $\pm 2000fs^3$ for TOD as pulses close to Fourier transform limit. This method has approached the targeted precision of 1% required by the LUXE project. To further improve the precision, several potential solutions are proposed. One involves using a CCD camera with a bit depth of 16 bits or more if available, to improve the precision of relative energy caused by shot noise by 0.7 times smaller. In the LUXE experiment, this method will be applied using the actual focal spot and the results of this nonlinear intensity measurement will be cross-verified with the comprehensive intensity measurements of the focal spot.

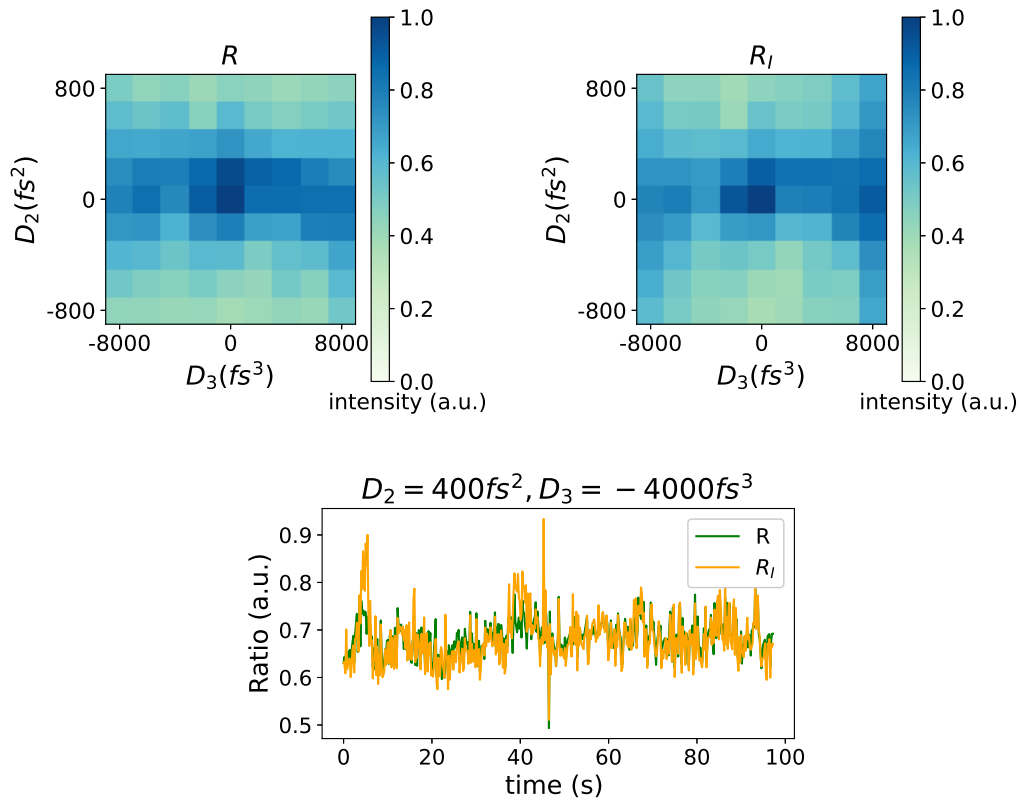


Figure 5.8: (a) plots the ratio R with different chirps added to the spectral phase. (b) plots the intensity ratio R_I with τ_ω measured and $\tau_{2\omega}$ inferred from the corresponding measured τ_ω . (c) plots the R and R_I of 500 shots consecutively taken when setting $D_2 = 400fs^2$ and $D_3 = -4000fs^3$.

6 Three-dimensional Characterization of Ultrashort Laser Pulses

The presence of spatio-temporal couplings (STC) within laser beams, such as spatial chirp and pulse-front tilt, significantly impacts the intensity of the focal spot. These couplings cause the focal spot of each wavelength to shift in both longitudinal and transversal directions, resulting in a spectrum that varies across the temporal and transversal regions of the focal spot. This misalignment, typically induced by chromatic optical components such as gratings and lenses, compromises both spatial and temporal alignment, leading to a decrease in peak intensity.

To address these issues, it is essential to measure the entire three-dimensional electric field at the focal spot to deduce STCs. The INSIGHT technique is employed to measure and fully reconstruct the laser electric field $E(x, y, \omega)$. By obtaining this comprehensive measurement, one can deduce the local profiles at each point within the focal spot and thus determine the local intensity distribution. This technique is crucial for improving the precision of determining the pulse intensity and accurately simulating laser-matter interactions by providing precise laser parameter inputs.

Further details about INSIGHT, including its principles and scheme, are presented in Section 6.1.1. Moreover, to validate the measurements by INSIGHT, an additional experiment was conducted. This involved employing narrow band-pass filters of different wavelengths to measure the wavefront. The results of both measurements are presented and discussed in Sec. 6.2.

6.1 Method

6.1.1 INSIGHT

The INSIGHT technique [54] offers an approach for obtaining the electric field $E(x, y, \omega)$ of an ultrashort laser pulse. This method achieves a complete three-dimensional reconstruction of the spatio-spectral phase, $\phi(x, y, \omega)$, and the spatio-spectral amplitude, $A(x, y, \omega)$, of the laser beam, based on the combination of spatially-resolved Fourier-transform spectroscopy and an alternate-projection phase-retrieval algorithm. Initially, INSIGHT obtains the amplitude profiles at different transversal planes along

the z -direction near focus from the 3D interferograms. These interferograms are collected at the optimal focus position ($z = 0$) and a few Rayleigh lengths before and after the focus ($z = \pm 3z_R$ in this study). Subsequently, the phase information is retrieved from the amplitude data. Typically, Gerchberg-Saxton iterative algorithm [97] is employed to extract the spatial phase profile of a monochromatic beam through repeated 2D Fourier transform iterations of the complex field between two transversal planes. However, INSIGHT applies this algorithm to individually retrieve the complex field at each frequency within the laser spectrum. This process provides not only detailed insights into $E(x, y, \omega)$ of the focal spot but also the laser beam propagation along the z -direction. Furthermore, INSIGHT extends its analysis by decomposing the spatial phase of each wavelength into a linear combination of Zernike polynomials. It significantly deepens the understanding of the STCs influencing the focal spot profile, allowing for a more quantitative identification of specific aberrations. Such decomposition facilitates the precise optimization of the laser's performance.

The INSIGHT device is very compact, for it operates near the focal spot and is unaffected by the size of the beam. This feature enables the use of smaller optical components while ensuring the entire beam is measured accurately. The setup of INSIGHT consists of a Michelson interferometer, as illustrated in Fig. 6.1. This configuration employs a beamsplitter to generate two identical versions of the incident beam. The first beam, after transmitting through the beamsplitter, is reflected by the high-reflection mirror M2. The transmission rate of the mirrors is in the order of 10^{-6} , allowing the observation of leak light from M2 by CCD1. The other path is the beam reflected by the beamsplitter. The two beams are carefully aligned to overlap on the (x, y) plane when they arrive at CCD2. Their interference is then recorded by the CCD2. To adjust the time delay between these two paths, the high-reflection mirror M1 is driven along the beam-propagation direction by a piezo element with a sub-optical-cycle precision, resulting in an interference pattern recorded by CCD2.

In the focal spot characterization experiment utilizing the INSIGHT device, the original focal spot is located inside a vacuum chamber, focused by an off-axis parabolic mirror with $f/20$, while INSIGHT is set up outside of the chamber. To bridge this spatial divide, a 1:1 relay imaging system is employed. This system comprises two identical achromatic lenses (Thorlabs ACT508-250-B) which images the focal spot directly onto the camera sensor. Additionally, the wavefront of this focal spot has been optimized to an RMS of 0.05λ by using an adaptive mirror. Its spectral phase is

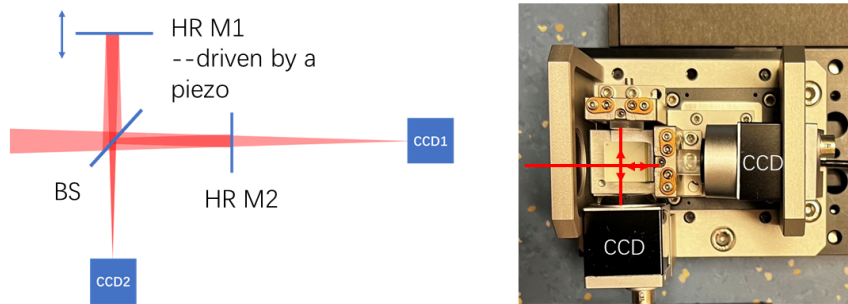


Figure 6.1: Left: the scheme of INSIGHT. Right: the picture of the commercial model of INSIGHT from SourceLAB.

also optimized to close to Fourier transform limit by tuning the Dazzler. As multiple shots are necessary to complete one measurement, INSIGHT uses the leak light image captured on CCD1 as a reference to compensate for the shot-to-shot fluctuation of the beam pointing.

The three-dimensional(3D) interferograms, as presented in Fig.6.2, are obtained by scanning the temporal delay between two beam paths with a temporal resolution of 0.5 fs spanning a range of ± 100 fs, until the two beam paths no longer overlap temporally. The scanning procedure is performed at the optimal focal plane (where $z = 0$) and at the near-focus planes (where $z = \pm 3z_R$).

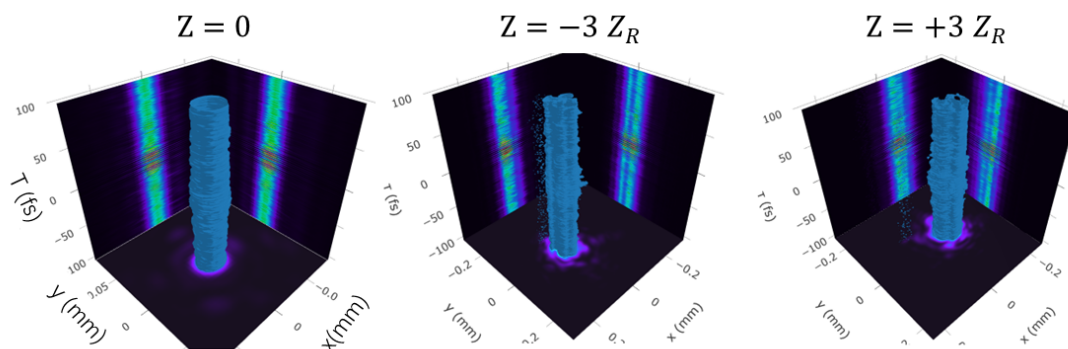


Figure 6.2: 3D interferograms are obtained by scanning the temporal delay between the two beams at a time step of 0.5 fs and a range of ± 100 fs at the transversal planes where $z = 0, \pm 3z_R$

6.1.2 Spectrally-Resolved Wavefront Measurement

To verify the measurements obtained with INSIGHT and cross-check the results, a second measurement method involving spectrally-resolved wavefront analysis was employed. By measuring the wavefront at each specific wavelength, focal spots of different wavelengths can be retrieved by performing a Fourier transform and hence the spectral electric field distribution of the laser pulse. This will allow us to assess the divergence behavior of the beam as it propagates and to evaluate and compare the size and centroid of the focal spot for each wavelength. The local spectrum across the spectrally-integrated focal spot's transversal plane can be acquired, leading to a precise determination of the local intensity distribution. Such comparisons are crucial for thoroughly understanding how individual wavelengths and STC contribute to the beam's overall focus.

Additionally, the wavefront deformation is measured in units of λ . A notable challenge with ultrashort laser pulses, which are characterized by a broad spectrum, is that the measurements do not specify the exact value of λ for such a wide range of wavelengths. This can result in optimization and measurement processes that are inherently less precise.

In this experiment, the process begins with the employment of an imaging system, consisting of the focusing OAP and an achromatic lens with $f=40$ mm. This system images the near-field plane located at the vicinity of the deformable mirror onto the wavefront sensor. To isolate and measure the wavefront of each specific wavelength, narrow band-pass filters (BPF) are placed before the wavefront sensor, with central wavelengths of 750, 770, 780, 800, 810, and 830 nm, each with a FWHM band-pass of 10 nm.

6.1.3 Longitudinal Focal Shift Measurement

A third measurement, focusing on the longitudinal focal shift of different wavelengths, was also performed to further verify the reliability of the previous two measurements. This method again involves the use of narrow band-pass filters. BPFs are placed at the CCD to capture the focal spots of each wavelength. By scanning the microscope objective in the z direction to image different planes near the focal spot, the divergence behavior of the beam is assessed as it propagates along the z -axis for individual wavelengths. By adjusting the microscope objective along the z -axis within a range of

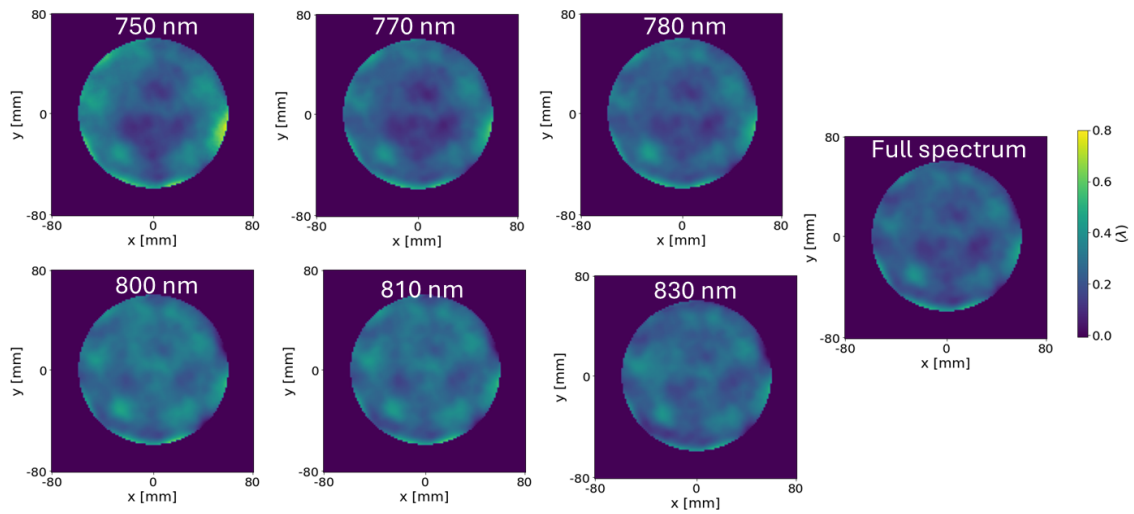


Figure 6.3: Wavefront measured by placing BPFs to the wavefront sensor and the wavefront without BPFs. Each wavelength displays a distinct wavefront pattern. The full-spectrum wavefront illustrates the combined effect of all the individual wavelengths.

± 5 mm around the focal point, and employing narrow band-pass filters designed for 770 nm, 800 nm, and 830 nm—with each filter allowing an FWHM bandpass of 10 nm—images of the beams' focal regions are captured, as well as the focal spot with full spectrum without BPFs.

6.2 Results

This section discusses the outcomes of the 3-dimensional measurement, including the methods using INSIGHT and BPFs, to assess the focal spot characteristics of the JETi200 laser.

6.2.1 Spectrally-Resolved Wavefront

The result of the wavefront by INSIGHT is shown in Fig.6.5(e)-(f). The wavefront measurements for each wavelength, by using the wavefront sensor SID with narrow band-pass filters, displayed in Fig.6.3, show a clear variation across the spectrum, indicating that the wavefront deformation is wavelength-dependent. The decomposition of the wavefronts into Zernike modes, as shown in Fig.6.4, provides a detailed

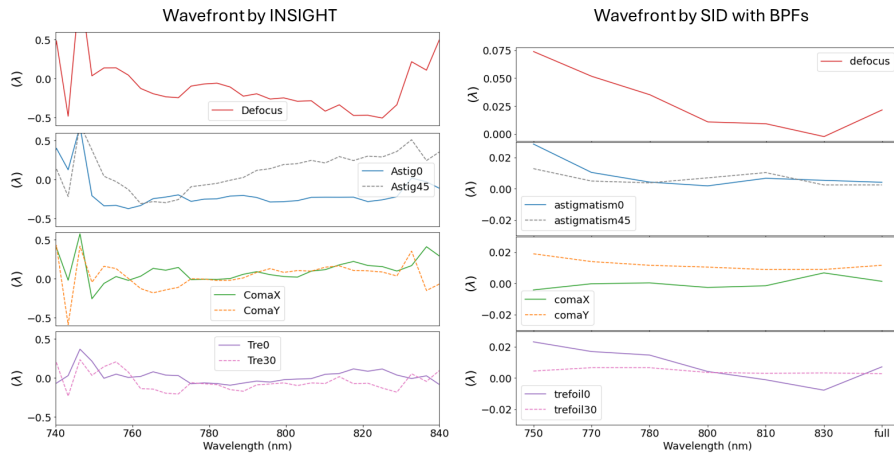


Figure 6.4: Zernike polynomials of spectrally-resolved wavefronts acquired by (left) INSIGHT and (right) the wavefront sensor SID with BPFs.

breakdown of the specific aberrations present at each wavelength. The left panel represents the Zernike polynomials acquired by INSIGHT, while the right panel shows the wavefront sensor SID measurements with BPFs. The overall tendency of the defocus term decreases with increasing wavelength, indicating a shift of focal spot along the propagation direction, while the other six terms are relatively stable with slight changes across the spectrum (except the astigmatism 45 term of INSIGHT measurement). The differences in the wavefront across the spectrum result in spatio-temporal couplings, including transversal focal shift, longitudinal focal shift, and variations in focal spot size across the same transversal plane.

6.2.2 Spectrally-Resolved Far-Field

The INSIGHT measurement retrieves the intensity distribution $A^2(x, y, \omega)$ at $z = 0$, as illustrated in Fig.6.5. The figure presents the spectrally-integrated focal spot, the spectrum, the spectrally-resolved focal spot intensity and especially for $\lambda = 830, 800,$ and 770 nm, and the wavefront for the three wavelengths.

However, compared to the focal spot obtained by a high-resolution imaging system, as shown in Fig.4.4, the focal spot obtained by INSIGHT has a much lower resolution. Using the 1:1 relay imaging, the focal spot with an FWHM of $20 \mu m$ is resolved to only about 4 pixels. Furthermore, using an imaging system with a magnification greater than 1 is not feasible. With a magnification >1 , Z_R increases quadratically

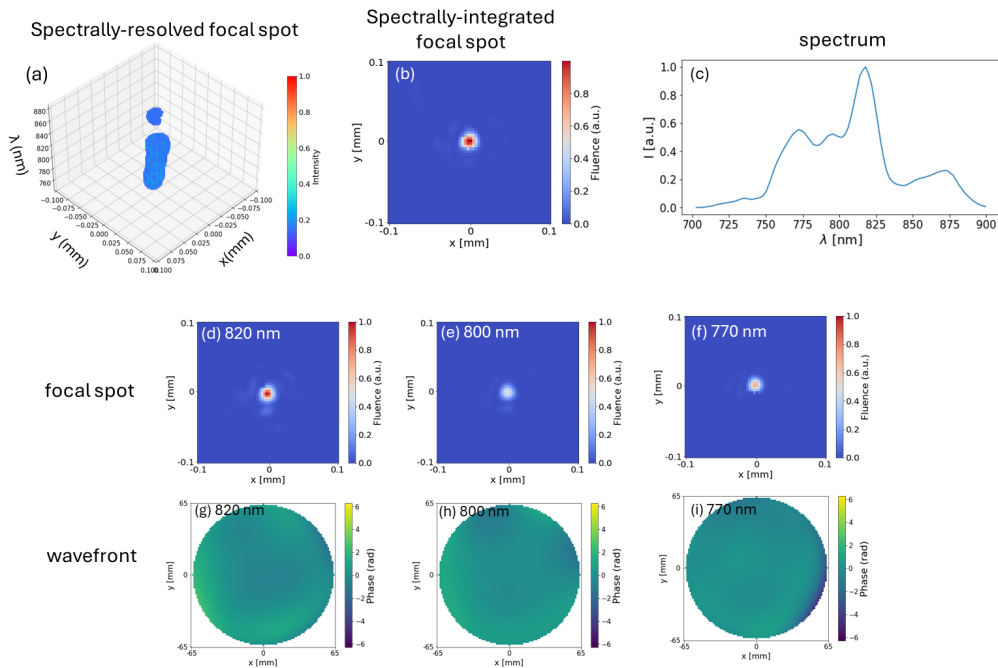


Figure 6.5: INSIGHT results: (a) Spectrally resolved focal spot $|E(x, y, \lambda)|^2$. (b) spectrally-integrated focal spot. (c) spectrum. (d)-(f): three focal spots with three individual wavelengths. (g)-(i) the wavefront of each corresponding wavelength.

with the magnification. When acquiring data by scanning at $Z = \pm 3Z_R$, the beam size becomes much larger and the intensity decreases significantly, resulting in signal levels that are as low as the noise level. Especially when scanning at $Z = 3Z_R$, the focal spot is inside the cubic beamsplitter, which will damage the beamsplitter.

The spectrum obtained by INSIGHT is different from the one measured with a spectrometer as shown in Fig.4.9. Especially, there should not be a peak at around 870 nm.

For a numerical comparison of the spot size and centroid of the focal spot across wavelengths, further analysis of Fig.6.5 leads to the plot of Fig.6.6. This figure shows the spectrally-resolved beam centroid shift in both x- and y-directions as well as the spectrally-resolved focal spot width $D4\sigma_x$ and $D4\sigma_y$. In the x-direction, the centroid shifts between $-5 \mu\text{m}$ and $10 \mu\text{m}$. In the y-direction, the centroid values range from $-5 \mu\text{m}$ to $0 \mu\text{m}$. These centroid shifts correspond to the spatial chirp of $0.17 \mu\text{m}/\text{nm}$ and the angular chirp of $0.06 \mu\text{rad}/\text{nm}$ in the x-direction, and the spatical chirp of $0.06 \mu\text{m}/\text{nm}$ and the angular chirp of $0.02 \mu\text{rad}/\text{nm}$. The centroid shifts, however, are a shift of 3 pixels in the x-direction and 1 pixel in the y-direction, which has an

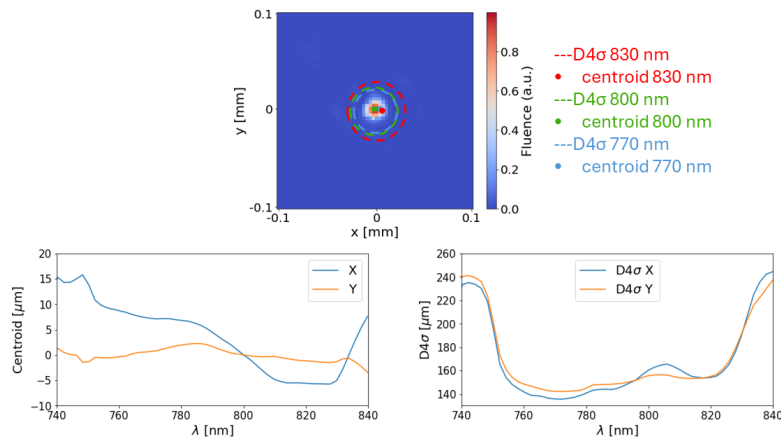


Figure 6.6: INSIGHT results: The centroid, indicating the focal shift, and $D4\sigma$ focal spot size for each spectral component in the transversal plane.

error of 33% and 100%.

On the other hand, the focal spots are calculated using the wavefront measured with BPFs, as shown in Fig. 6.7. The focal spot images are calculated at $z=f$ where f is the focal length of the OAP. In this case, the longitudinal focal shift, which is the variation in the best focal position for different wavelengths along the z -axis, can cause the focal spots to be larger at $z=f$ than their respective minima. As a result, the resulting focal spot with the full spectrum would appear larger than the diffraction limit. Similarly, the centroid and the $D4\sigma$ spot size at $z=f$ are obtained from these focal spots. The results are plotted in Fig.6.8. Compared to the results obtained using INSIGHT, the focal spot drift in the transversal plane is within $1 \mu\text{m}$, which is negligible. The focal spot sizes range from about $100 \mu\text{m}$ to $120 \mu\text{m}$ in both x - and y - directions. The overall trend indicates that the focal spot size is larger for shorter wavelengths and smaller for longer wavelengths. However, this observation contradicts the trend predicted by Eq.2.39, which suggests that longer wavelengths should result in larger focal spot sizes. Consequently, the change in focal spot size at $z = f$ is primarily due to the longitudinal focal shift, indicating that at $z=f$, the spot size for each wavelength may not be at its minimum. When comparing the measured $D4\sigma$ sizes to the diffraction limit, which is $50 \mu\text{m}$ in the x -direction and $58 \mu\text{m}$ in the y -direction, it is evident that the actual focal spot sizes are significantly larger. This discrepancy further supports the hypothesis that the focal spots are not at their minimum sizes at $z = f$ likely due to longitudinal focal shifts.

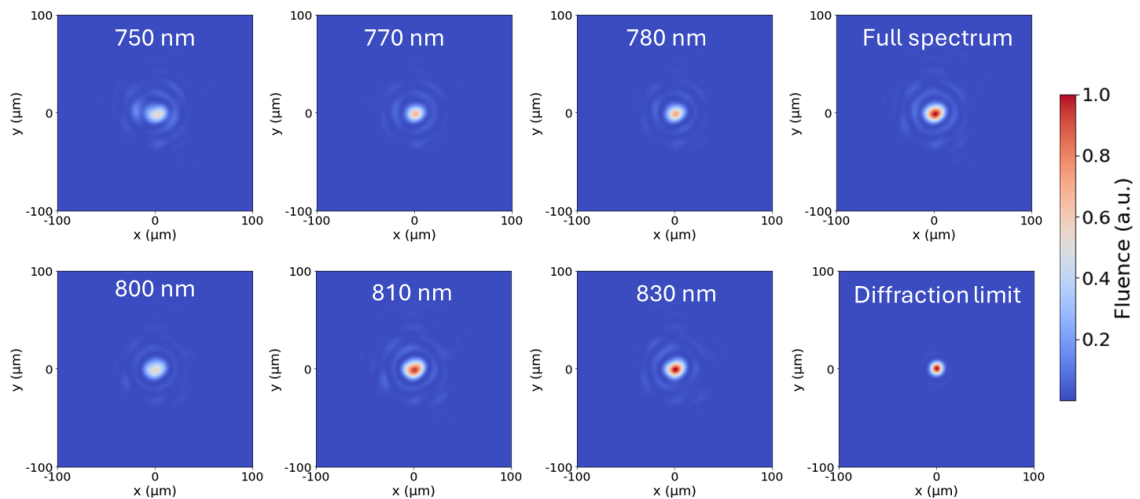


Figure 6.7: SID with BPFs results: the focal spot at $z=f$, calculated from the wavefront measured with BPFs, normalized to the relative spectral intensity, as well as the focal spot at $z=f$ with full spectrum and the diffraction-limited focal spot.

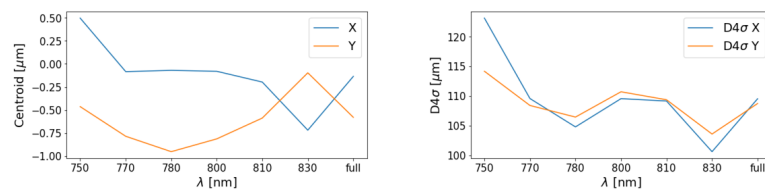


Figure 6.8: SID with BPFs results: The centroid and $D4\sigma$ focal spot size for each spectral component at $z=f$

6.2.3 Longitudinal Focal Shift

When analyzing the wavefront of each wavelength by decomposing it into Zernike polynomials, the term of curvature is different for each wavelength, which contributes to the longitudinal focal shift, caused by several refractive telescopes in the laser. The results are plotted in Fig.6.9. The results of both measurement methods exhibit a linear chromatic focal shift where longer wavelengths converge closer to the focusing optics, in contrast to shorter wavelengths with a 'slower' focusing. The overall longitudinal focal shift obtained through the measurement using SID wavefront sensor with BPFs is approximately 0.6 mm from 750 nm to 830 nm. The longitudinal focal shift for the measurement of INSIGHT is around 1.0 mm over the same wavelength range.

The two methods using INSIGHT and wavefront with BPFs perform measurements

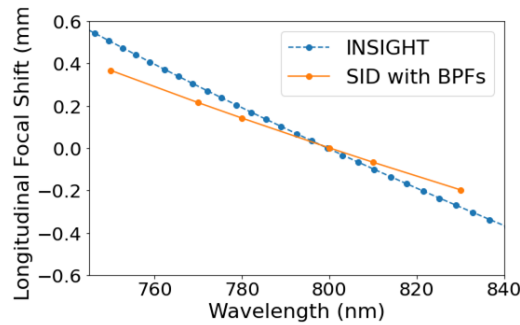


Figure 6.9: The figures show the focal shift in the longitudinal direction, where the peak intensity position in the z -direction of each wavelength shifts. The blue dots are the results measured by INSIGHT, while the orange dots are the results obtained from the wavefront measured using SID4 with BPFs.

independently and show different results. To determine which method is more reliable, a third measurement is introduced. This method involves measuring the spots near the focal plane with BPFs and cross-referencing the results with the other two measurement results.

The measurement is performed by scanning the microscope objective between -5 mm to $+5$ mm in the z direction around the focal plane to image different planes near the focal spot with a step size of 1 mm. The near-focus profiles are shown in Fig.6.10 for three different band-pass filters at wavelength 770 nm (b), 800 nm (c), and 830 nm (d), as well as for the full spectrum without any BPFs (a). The full spectrum case (a) shows the combined effect of all wavelengths, where the best focal plane remains around 0 mm. Columns (b) to (d) show that as the wavelength increases from 770 nm to 830 nm, the most tightly focused spot shifts from 0 mm to -1 mm. Additionally, the spot size at $z=-5$ mm decreases with increasing wavelength, while the spot size at $z = +5$ mm increases with increasing wavelength. These observations indicate that the focal plane shifts longitudinally in the $-z$ direction with increasing wavelength .

The $D4\sigma$ of these beams are plotted in Fig.6.11 with quadratic fittings.

The numerical findings derived from Fig.6.11 are listed in Table6.1. Analysis along the x -axis reveals a longitudinal focal shift ranging between 770 nm and 830 nm of approximately 0.6 mm, whereas along the y -axis, this shift increases slightly to 0.7 mm. This observed focal shift is consistent with the results calculated from wavefronts measured with BPFs, which is 0.6 mm, and is less than the 1.0 mm shift measured using INSIGHT, as shown in Fig.6.9.

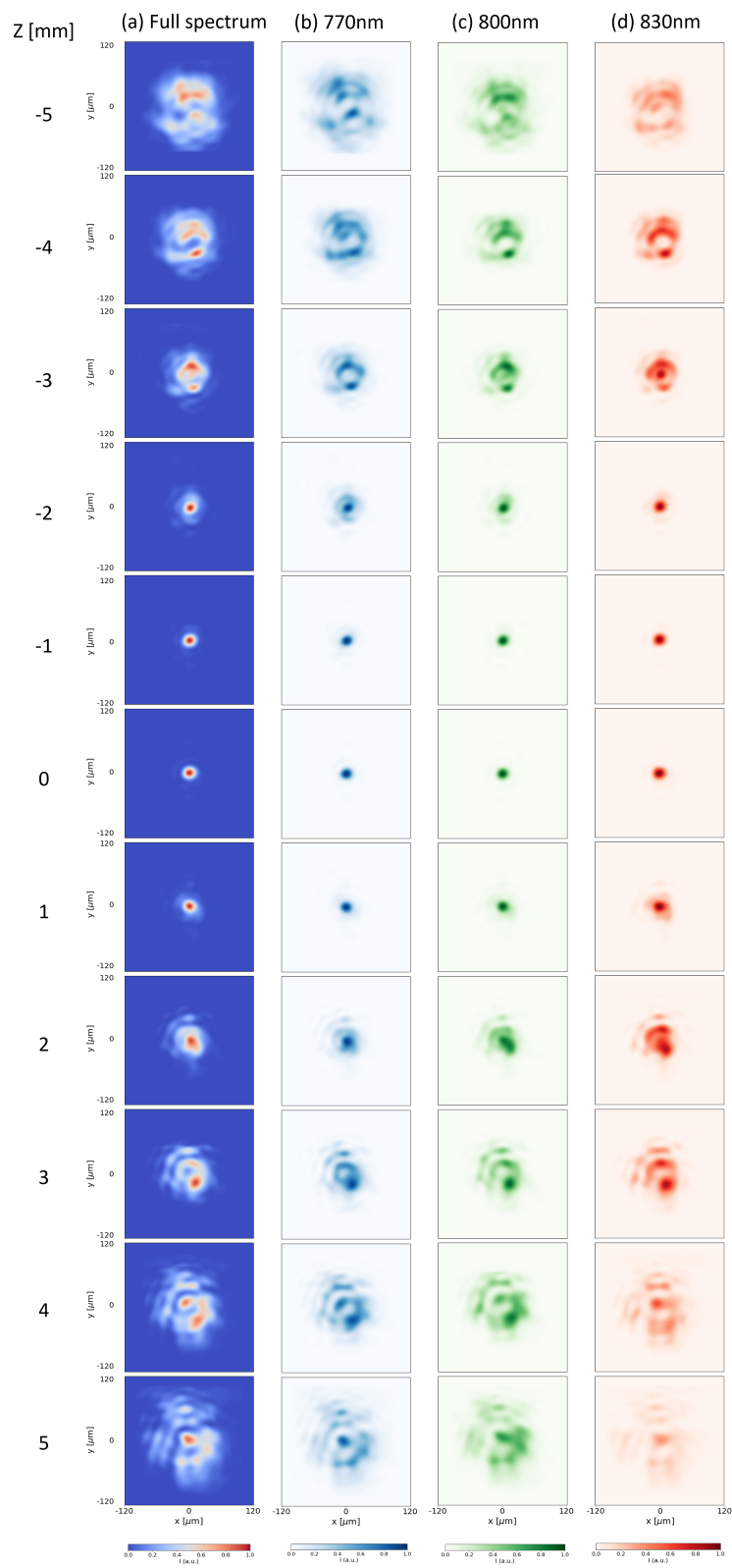


Figure 6.10: Focal spot profiles near the focal plane, scanned between -5 mm to $+5$ mm along the z -axis, with band-pass filters at different wavelengths: (b) 770 nm, (c) 800 nm, (d) 830 nm, and (a) the full spectrum without BPFs.

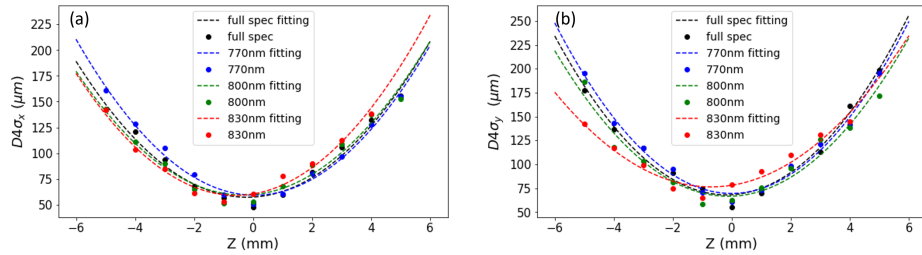


Figure 6.11: (a) Represents the $D4\sigma$ beam size measured along the x-axis for various wavelengths as a function of the z-axis position. (b) the $D4\sigma$ beam size along the y-axis as a function of the z-axis. Each graph showcases the focusing characteristics of laser beams at 770 nm, 800 nm, and 830 nm wavelengths, alongside the behavior of the full-spectrum beam, as well as a quadratic fitting for each.

As a result of comparing the three different measurements, the longitudinal focal

	Best focus position x[mm]	M_x^2	$D4\sigma_x$ [μm]	Best focus position y[mm]	M_y^2	$D4\sigma_y$ [μm]
830nm	-0.58	2.4	59.0	-0.70	3.2	76.3
800nm	-0.33	2.3	59.3	-0.13	3.0	66.5
770nm	0.06	2.5	59.2	-0.01	3.5	69.5
Full spectrum	-0.20	2.3	57.2	-0.18	3.3	68.0

Table 6.1: Numerical results for beam parameters at best focus position. This table presents the data corresponding to Fig.6.11, detailing the best focus position, M^2 factor, and $D4\sigma$ beam size for the full-spectrum beam and individual wavelengths of 770 nm, 800 nm, and 830 nm along both the x- and y-axes.

shift results obtained with INSIGHT are larger than those from the other two methods, while the other two methods present similar results. This comparison indicates that the results from wavefront measurements with BPFs and the third measurement method are more consistent with each other, suggesting they are more reliable than the INSIGHT method for assessing longitudinal focal shifts.

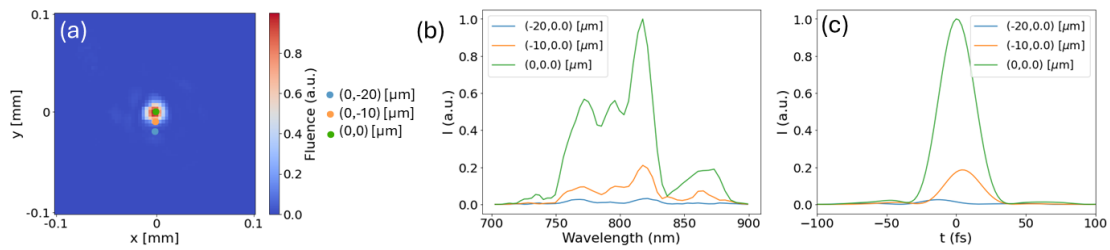


Figure 6.12: INSIGHT results: (a) indicates three locations at the focal spot plane. (b) the local spectra of the three points. (c) the local temporal profiles at the three points.

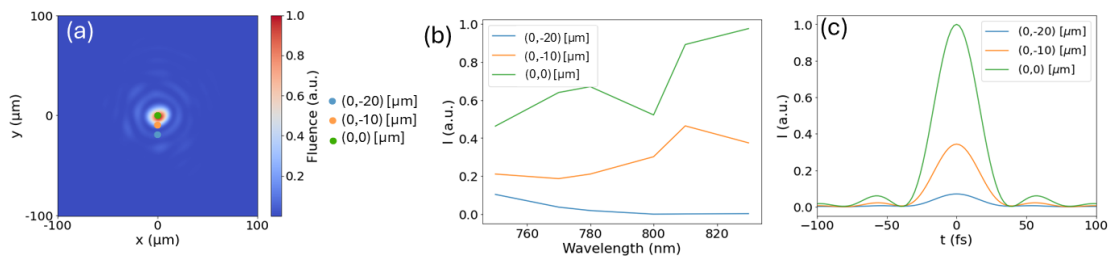


Figure 6.13: SID with BPFs results: (a) indicates three locations at the focal spot plane. (b) the local spectra of the three points. (c) the local temporal profiles at the three points.

6.2.4 Local Spectrum and Local Temporal Profile

By re-analyzing the same dataset with an alternative approach, where the spectrum at each local position (or each single pixel) is integrated, the impact of transversal focal drift with frequency on the local spectral variations across the transversal plane of the focal spot can be observed. Fig.6.12 and Fig.6.13 provide comparative results of the local spectra and temporal profiles at three different positions (0,0), (0,-10), and (0,-20) μm at the focal spot. Specifically, for the INSIGHT results, the spectrum at point (0,0) is found to be more intense than that at other points. However, its FWHM bandwidth is the same as that of the spectrum at (0,-10). Such disparities in local spectra inevitably lead to variations in the temporal peak intensity but the same pulse duration of 23 fs. The local temporal profile can be deduced by taking the Fourier transform using the local spectrum and the local spectral phase. However, INSIGHT only determines $E(x, y, \omega)$ up to an unknown spatially-homogeneous spectral phase, incapable of precisely reconstructing the pulse in the (x, y, t) domain. To complement INSIGHT's measurements, the temporal profile characterized by $E(\omega)$ and $\phi(\omega)$ is measured independently. The results measured by the technique of SRSI using Wizzler

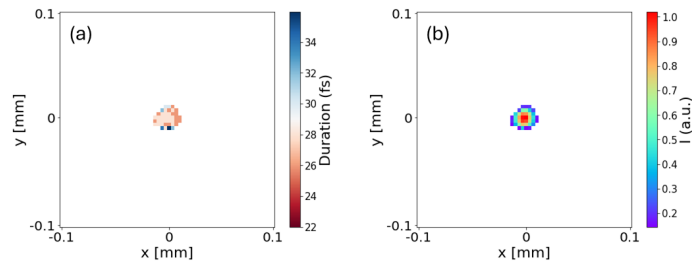


Figure 6.14: INSIGHT results: (a) the local pulse duration at the focal spot plane. (b) the local intensity

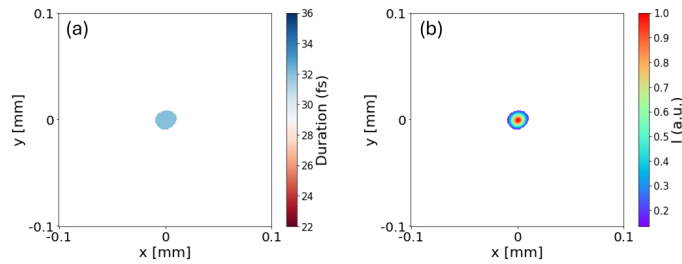


Figure 6.15: SID with BPFs results: (a) the local pulse duration at the focal spot plane. (b) the local intensity

have been presented in Sec.4.7. Given the prior optimization of the spectral phase through a Dazzler and the measurement of the temporal profile via a Wizzler, a flat spectral phase is assumed for the INSIGHT calculations.

Limited by narrow band-pass filters, the spectrum of the measurement with BPFs, as shown in Fig.6.13(b), is discontinuous and less accurate. Consequently, using this spectrum to perform a Fourier transform to obtain the temporal profile results in a pulse duration of 32 fs. This duration is larger than the results obtained with INSIGHT, due to the incomplete spectral information.

Using this method, the comprehensive plot of pulse duration across the focal spot, where the fluence is greater than $1/e^2$ of its maximum, is obtained and presented in Fig 6.14(a) and Fig.6.15(a).

In the end, instead of obtaining the intensity by taking the average fluence within the FWHM focal spot area and dividing it by the temporal duration measured at the near-field, the local intensity at each point across the transversal plane is obtained and presented Fig 6.14(b) and Fig.6.15(b). Instead of averaging out the intensity variation across the focal spot, as the three-dimensional characterization directly correlates the local fluence with the corresponding temporal duration at each point, it leads to a more accurate mapping of intensity distributions across the focal plane.

For the INSIGHT to accurately characterize a laser source, the laser source should exhibit stability and reproducibility in both temporal and spatial domains across about one thousand (depending on the settings of measurement) successive shots for this multi-shot measurement. However, shot-to-shot fluctuations in both the spectral and spatial phases of the laser beam are common, leading to variations in its temporal and spatial profiles. Specifically, according to the results presented in Sec.4.9, the RMS of wavefront fluctuation shot-to-shot is 10%, leading to the RMS of the Strehl ratio to be 2.7%, and the RMS of focal spot size variation is 2%. Consequently, the interferograms of the INSIGHT measurements acquire a cumulative effect of all laser shots fluctuation over 1000 shots with a precision of approximately 5%. Furthermore, in the INSIGHT measurement, the low resolution of the focal spot, which takes only 4 pixels as discussed above, result in a precision of the focal spot of 25%.

BPFs are limited by the availability of narrow band-pass filters, which results in a discontinuous spectrum. This discontinuity leads to incomplete spectral information and, consequently, an inaccurate temporal duration measurement. Compared to the results obtained by INSIGHT and SRSI, the pulse duration obtained using BPFs can be off by more than 30%. This inaccuracy in temporal duration directly affects the calculation of local intensity. Therefore, while BPFs method is more trustworthy when measuring the longitudinal focal shift, their limitations in spectral completeness must be considered when interpreting the results.

7 Characterization and Optimization of Laguerre-Gaussian Laser Pulses with Orbital Angular Momentum

In the work by Allen *et al.*[59], Laguerre-Gaussian (LG) laser beams were shown to carry orbital angular momentum (OAM) along their propagation axis. This certain type of laser mode contains the azimuthal phase variation of the wavefront, characterized by the non-zero topological charge l . Its far-field intensity profile is ring-shaped, featuring a hollow central core. Various methods have been proposed to generate an LG beam carrying OAM. It can be achieved through computer-generated holograms[60], segmented deformable mirrors[61], and a variety of spiral phase plates (SPP), such as SPP made of liquid crystals[62] and those fabricated by the method of electron beam lithography on polymethylmethacrylate layers over glass substrates[63, 64]. An SPP is an optical element that introduces an azimuthal dependence, $l\varphi$, with φ representing the azimuthal angle, to the electric field of the laser, transforming a flat wavefront into a helix. An LG beam with OAM has applications in various fields of science and technology, such as optical manipulation, where LG beams enable precise control of motions of micro-particles in optical tweezers by transferring the OAM to trapped particles[65], and in microscopy, where LG beams are employed in stimulated-emission depletion (STED) microscopy to enhance the resolution to scales of 30-80 nm[66], and in the field of particle acceleration, where structured wakefields can be generated using OAM-carrying laser beams to accelerate positrons [67] and ring-shaped electron beams[68].

The generation of terawatt-level vortex beams carrying OAM with topological charges of $l=1,2$, and 3 has been successfully reported in [98]. An uneven intensity distribution has been observed along the ring of the vortex beams. It can be optimized by applying Zernike modes to the wavefront according to the ring deformation [99]. Despite the groundbreaking achievements of generating and optimizing such high-power vortex beams, the specific factors contributing to this non-homogeneous intensity distribution have yet to be identified and characterized. This gap in understanding underscores the need for further investigation into the beam formation mechanisms

and the influence of system parameters on the spatial intensity profile of vortex beams at such high energy levels.

The focal spot of an LG beam carrying OAM, generated by inserting a spiral phase plate with $l = 1$ at a central wavelength of $\lambda_0 = 800nm$ to the beam path, is characterized by a donut-shaped fluence profile. Despite efforts to optimize the beam's wavefront using a deformable mirror prior to the SPP insertion, the spatial fluence profile remains significantly influenced by the near-field profile and wavefront characteristics of the beam. Moreover, the focal spot fluence profiles exhibit considerable variability from shot to shot, which can lead to substantial instability in structured wakefields, thereby impacting the experimental results in laser-plasma acceleration processes. In this study, the aim is to characterize the focal spot of the LG beam and systematically identify the factors that influence its profile. Subsequently, a systematic optimization strategy based on these factors is proposed and conducted, including the application of a phase mask comprising a linear combination of Zernike polynomials. This approach is designed to achieve a more uniform fluence distribution across the focal spot profile, which is particularly crucial for experiments focused on laser guiding in plasma[69], where the predictability and stability of the focal spot profile play a vital role in the success and accuracy of the experimental outcomes.

7.1 Characterization of Laser Pulse with Orbital Angular Momentum

The focal spot of a Laguerre-Gaussian (LG) beam which carries orbital angular momentum (OAM), is created using a spiral phase plate with $l = 1$ at a central wavelength of $\lambda_0 = 800nm$. The focal spot measured is illustrated in Fig.7.1(a). Unlike the uniform shape of a Gaussian beam, the focal spot of an LG beam with OAM has a donut-like shape, making the usual Gaussian fitting inappropriate for its characterization. To better represent this unique shape, the donut-shaped focal spot is transformed into polar coordinates, as depicted in Fig.7.1(b). For a more detailed view of how the fluence changes along a specific circle within the donut, a lineout at selected radii is plotted, as shown in Fig.7.1(c), chosen based on the average fluence values at half the maximum (HM) for the inner circle, the peak maximum, and half the maximum for the outer circle. The peak-to-valley (PtV) and standard deviation

values across these radii—0.67 and 0.22 for $r=8.6 \mu\text{m}$ at inner HM, 0.52 and 0.13 for $r=14.6 \mu\text{m}$ at the maximum, and 0.34 and 0.09 for $r=20.3 \mu\text{m}$ at outer HM—offer a detailed visualization of fluence variation around the beam’s perimeter. This approach not only clarifies the spatial fluence distribution within the LG beam’s focal spot but also establishes a benchmark for evaluating beam quality.

However, the spatial fluence profile of the donut-shaped focal spot differs significantly

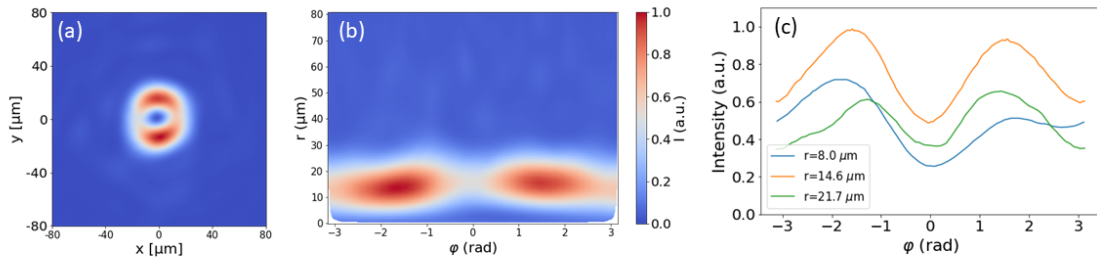


Figure 7.1: (a) The measured focal spot of LG beam with OAM, with $l = 1$ at $\lambda_0 = 800\text{nm}$, features a donut shape. (b) The donut-shaped focal spot is plotted in polar coordinates. (c) Lineouts at selected radii ($r=8.6, 14.6,$ and $20.3 \mu\text{m}$) showcasing the fluence variation along specific circumferences within the donut shape, with the radii chosen at inner half maximum, maximum, and outer half maximum points, respectively.

from shot to shot, which can lead to considerable instability in experimental outcomes in laser-plasma acceleration processes. It is imperative to systematically identify the factors influencing the focal spot’s profile. Then optimization strategies should be developed to ensure a more consistent and stable beam profile.

7.1.1 Influence from Near-field Intensity Profile

The FF profile is strongly influenced by the NF profile. However, the near-field beam profile from the laser system does not always exhibit a perfect super-Gaussian shape with a symmetric intensity distribution centered at the beam axis, as shown in Fig.7.2(a). The near-field profile of the beam is not uniform and the measured NF is illustrated in Fig.7.2(b). When a spiral wavefront, depicted in Fig.7.2(c), is applied to this non-homogeneous near-field, the resulting far-field pattern is as shown in Fig.7.2(e). This FF pattern contrasts with the one in Fig.7.2(d), which is generated

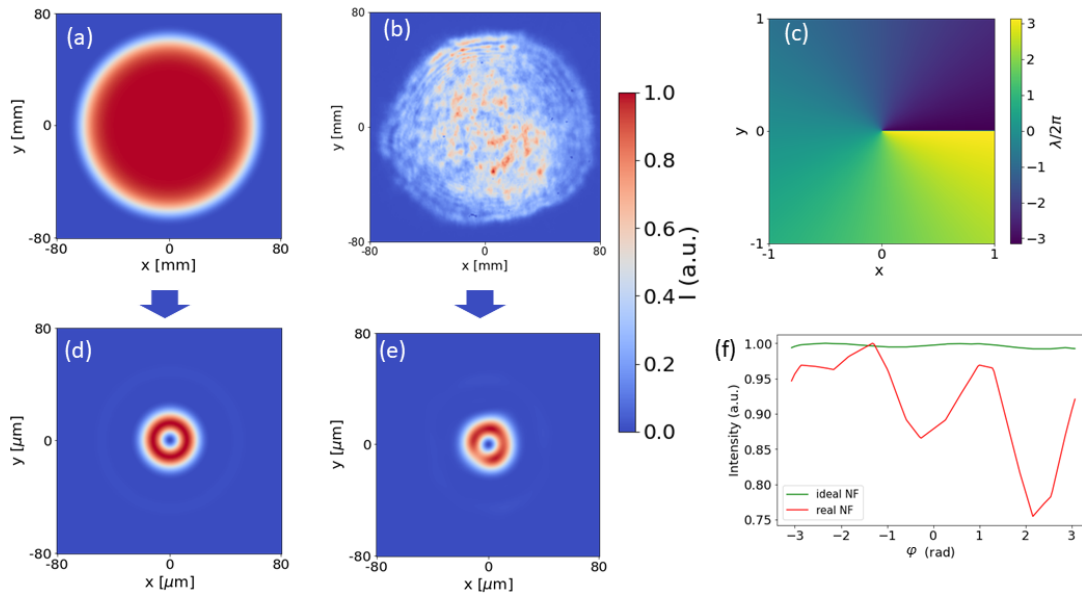


Figure 7.2: The figures illustrate the impact of near-field beam profile inhomogeneity on the far-field pattern when subjected to a spiral wavefront. It compares (d) the FF pattern resulting from (a) a super-Gaussian with $p=6$ NF profile with (e) the FF from (b) a non-homogeneous NF profile, both under the influence of (c) the same spiral wavefront. (f) The lineout shows differences at the peak-to-peak radius of $12.8 \mu\text{m}$, with a maximum difference of 25%.

from a perfect super-Gaussian near-field (shown in Fig.7.2(a) with $p=6$) combined with the same spiral wavefront in Fig.7.2(c). The lineout analysis in Fig.7.2(f) reveals PtV and standard deviation values of the intensity to be 0.25 and 0.08, respectively, at the peak-to-peak radius of $12.8 \mu\text{m}$ for Fig.7.2(e). In comparison, for FF derived from the perfect super-Gaussian near-field scenario in Fig.7.2(d), both PtV and standard deviation of the intensity are 0 at the peak-to-peak radius $12.8 \mu\text{m}$. This demonstrates that the inhomogeneous distribution observed in the far-field pattern primarily originates from the near-field profile's non-uniformity.

7.1.2 Influence from Alignment of the Singularity Point

In addition, the uneven intensity distribution in the near-field significantly influences the donut-shaped far-field pattern, especially when the singularity point of the SPP does not precisely align with the center of the NF beam. Aligning the SPP accu-

rately to position its singularity point at the beam's center poses practical challenges. Imperfections in the NF's intensity distribution, such as its unevenness and lack of circularity, create asymmetries around the singularity point. These asymmetries lead to noticeable variations in the FF intensity distribution. The effect of the singularity point's misalignment on the focus intensity is illustrated in Fig.7.3, obtained by calculation using the NF profile in Fig.4.9(a), while the measured experiment results are illustrated in Fig.7.5. When the singularity point of the SPP is shifted to the left of the NF beam's center, the NF intensity distribution becomes less symmetrical around the singularity point. This asymmetry leads to a FF intensity distribution that is denser on the left side, as demonstrated in Fig.7.3(a) and Fig.7.5(a). On the other hand, when the singularity point is shifted to the right, as shown in Fig.7.3(b) and Fig.7.5(b), the uneven intensity distribution also shifts, resulting in a more intense right side of the FF pattern. To ensure a more uniform FF intensity distribution during experiments, it is recommended to first capture an image of the NF. Subsequently, calculations should be made to find the optimal position for the singularity point before aligning the SPP in the laser beam path.

As shown in Fig.7.4, the curves are the lineouts at the peak-to-peak radius of the

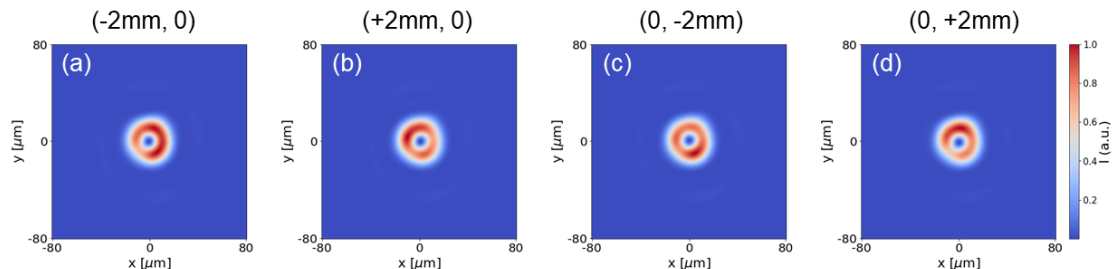


Figure 7.3: The calculated results: The coordinates above each column are the locations of the singularity points in the frame of NF, with the central point as $(0,0)$. (a)-(d) are the resulting far-field profiles.

focal spots in Fig.7.3 with different locations of the singularity point in the frame of NF, with $(0,0)$ defined as the center-of-mass of NF. The RMS value of each is: 0.09 for $(-2\text{mm},0)$, 0.11 for $(+2\text{mm},0)$, 0.09 for $(0,-2\text{mm})$, and 0.16 for $(0,+2\text{mm})$. The RMS value for $(0,0)$, as shown above, is 0.08, which is the smallest, indicating that aligning the singularity point of SPP at the center-of-mass of NF can obtain the most homogeneous intensity distribution of the donut-shaped focal spot.

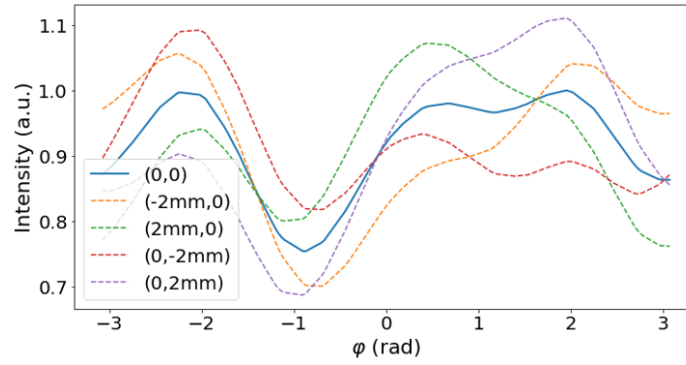


Figure 7.4: The lineout of the focal spots with different coordinates of the singularity point in Fig.7.3 and Fig.7.2(e). $(0,0)$ indicates the coordinates of the center-of-mass of the measured NF.

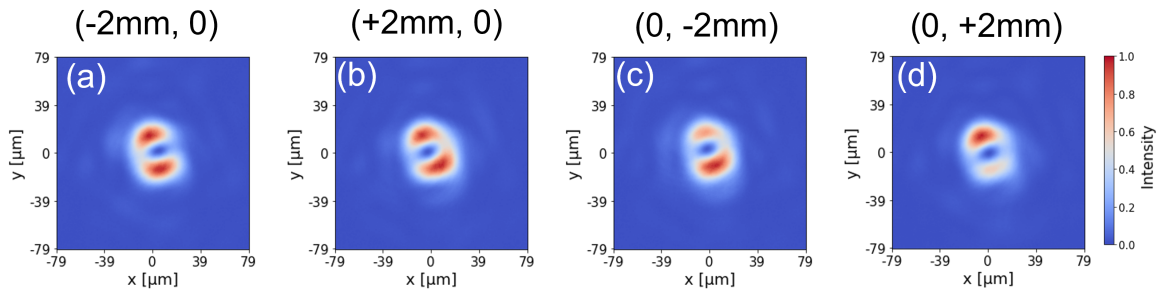


Figure 7.5: The measurement results of far-field profiles: The coordinates above each column are the locations of the singularity points in the frame of NF. The result of $(0,0)$ is shown in Fig.7.1(a).

7.1.3 Influence from Wavefront Aberrations

Wavefront aberrations significantly impact the intensity distribution of the donut-shaped focal spot in laser beams carrying orbital angular momentum. These aberrations, which can stem from various sources including imperfections in optical elements or alignment, affect the symmetry and uniformity of the beam's focus. Specifically, the different types of Zernike aberrations, each corresponding to a distinct kind of wavefront distortion, can alter the shape and intensity distribution of the donut-shaped focal spot, as depicted in Fig.2.9.

7.1.4 Influence from Different Spectral Components

Additionally, the wavefront differences are introduced by the broad spectrum inherent to the ultrashort laser pulse. The SPP used to implement orbital angular momentum to the beam is designed to introduce a 2π phase shift for the central wavelength λ_0 . However, for wavelengths within the pulse spectrum that deviate from λ_0 , the phase shift introduced by the SPP does not precisely match 2π . This means that the effective azimuthal index l , which determines the amount of orbital angular momentum carried by the beam, varies across the spectrum of the pulse. As a result, the far-field focus profiles for different wavelengths within the pulse can exhibit subtle yet significant variations in the intensity distribution. Fig.7.6 by calculation and Fig.7.7 by experiment measuring illustrate how the focus profiles change for three different wavelengths within the pulse spectrum. While the overall donut shape is maintained across these wavelengths, there is a noticeable variation in the intensity contrast which can vary by up to 20% for different wavelengths, highlighting the inhomogeneity introduced by the broad spectrum of the ultrashort pulse. Each wavelength within the broad spectrum of an ultrashort pulse contributes differently to the overall focal spot based on its intensity within the spectrum. Consequently, the focal spot intensity distribution, which is the cumulative effect of beams at different wavelengths, changes according to the varying intensity distribution of the spectrum.

7.1.5 Influence from Spiral Phase Plate

Furthermore, the SPP contributes to wavefront aberrations. The use of an $l = 1$ SPP, designed to introduce a continuous azimuthal phase variation of 2π at the central wavelength λ_0 , is a common approach to generating beams with OAM. However, due to manufacturing limitations, an ideal continuous phase variation is often approximated by a multi-step phase profile. In this study, the SPP used exhibits a 16-step approximation to the continuous phase change required for a 2π phase gap at λ_0 , as depicted in Fig.7.8(a). This approximation, while practical, introduces wavefront distortions that can affect the quality of the FF profile. Through computational analysis, the FF profile resulting from the 16-step SPP, as plotted in Fig.7.8(b), is compared with that obtained from a theoretical continuous phase change SPP, as plotted in Fig.7.2(d), revealing slight differences in the intensity distribution of the focal spot and the difference is plotted in Fig.7.8(c). Particularly, a lineout at the peak-to-peak

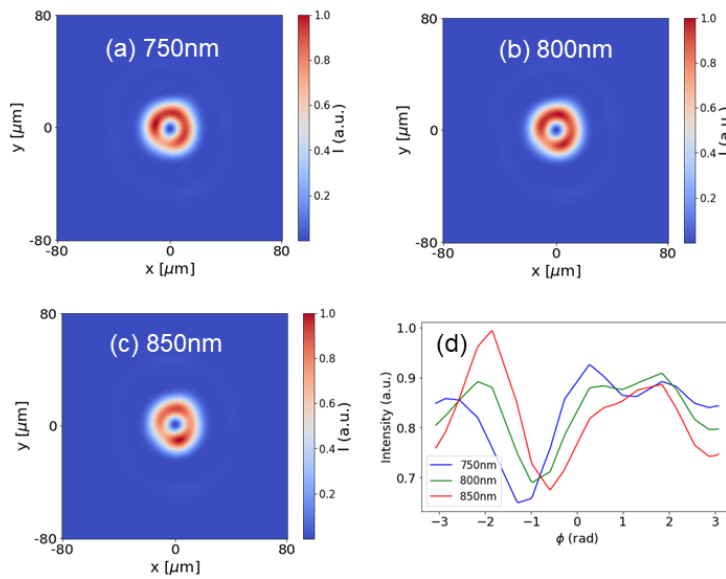


Figure 7.6: Calculated results: (a)-(c) Individual focus profiles of each spectral component showing the variation in intensity distribution. (d) The lineout of intensity along the peak-to-peak radius highlights the differences in intensity contrast for each spectral component.

radius ($r=12.8 \mu m$), as plotted in Fig.7.8(e), between the calculated FF profile of the 16-step SPP and the ideal continuous phase change indicates a maximum intensity difference of 1.5%. Compared to the intensity difference caused by other factors, such as the uneven NF intensity profile and wavefront aberrations, this difference caused by the segmented spiral phase plate is negligible.

In conclusion, achieving a uniform doughnut-shaped far-field intensity profile requires meticulous attention to the near-field intensity distribution's symmetry and homogeneity. It is crucial to precisely align the spiral phase plate so that its phase singularity point is perfectly centered within the beam. This ensures that any deviations, which could lead to an uneven intensity distribution, are minimized. Furthermore, the broad spectral bandwidth of the laser, ideally symmetrical around the central wavelength, plays a significant role in optimizing the focus profile by reducing spectral-induced distortions. Prior to the incorporation of the SPP into the beam path, it is imperative to optimize the wavefront to be as flat as possible, utilizing adaptive optics loops to correct any pre-existing aberrations. However, the introduction of the SPP necessitates further wavefront corrections to counteract the aberrations introduced by its discrete steps and the variations in the OAM value (l) across the spectrum. Employ-

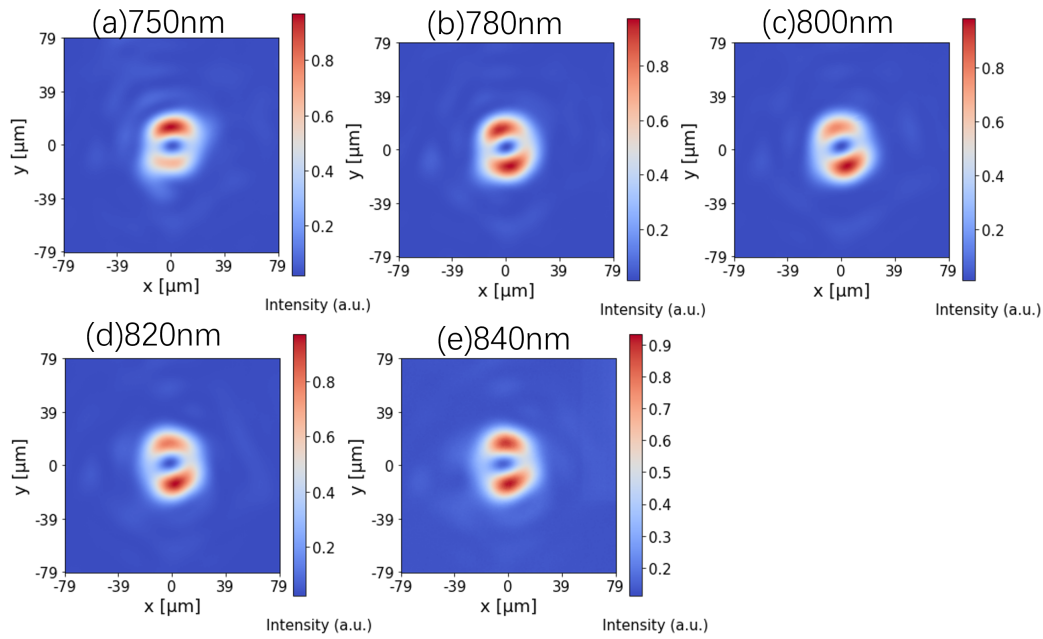


Figure 7.7: Experiment results of the focal spot at each spectral component by implementing narrow band-pass filters to the CCD camera, proving the aberrations caused by wavelength difference from the central wavelength.

ing a deformable mirror for additional wavefront corrections is essential to mitigate the effects of a nonuniform NF profile and the wavefront aberrations caused by the SPP's design and the broad spectral bandwidth. This comprehensive approach ensures the generation of a high-quality, homogenous doughnut-shaped far-field profile, vital for applications relying on precise beam shaping and control.

7.2 Optimization of beam with OAM

To counteract the non-uniformity of the NF intensity distribution and to mitigate the complex wavefront aberrations introduced by factors such as the non-unity values of the orbital angular momentum (l) for different frequencies, the potential misalignment of the phase singularity point from the beam center, and other inherent aberrations, an optimization approach involving adaptive optics is employed. This process includes the application of phase masks that are linear combinations of Zernike polynomials to the wavefront of the laser beam.

Initially, the laser's focal spot is optimized without the SPP in the optical path, by utilizing a wavefront sensor connected with a deformable mirror, enabling iterative

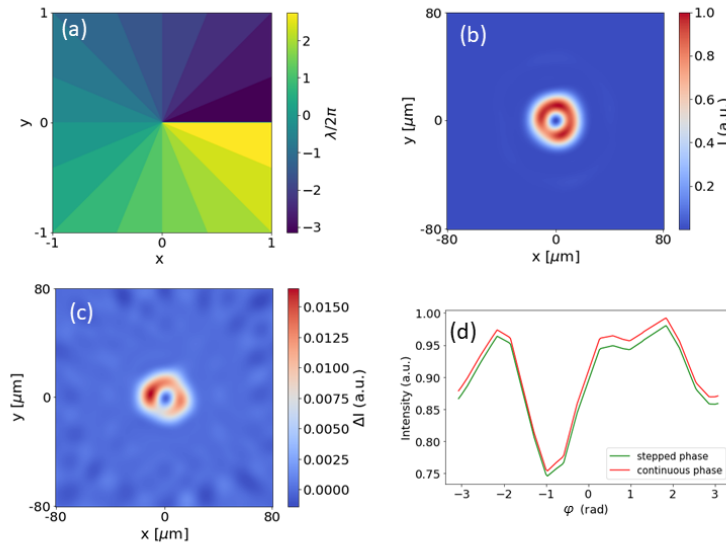


Figure 7.8: The figure demonstrates the impact of SPP design on wavefront aberrations and FF focus profile quality. (a) Shows the 16-step approximation of the SPP used to introduce a 2π phase shift at λ_0 , highlighting manufacturing compromises. (b) Depicts the FF profile generated by this 16-step SPP, while (c) illustrates the differences in intensity distribution when compared to an ideal continuous phase SPP plotted in Fig.7.2(d). A line-out at peak-to-peak radius $r=12.8 \mu\text{m}$ in (d) reveals a maximum intensity discrepancy of 1.5%.

adjustments to minimize wavefront aberrations. The RMS value of the wavefront aberration is reduced down to 0.06λ and PtV value to 0.6λ , thereby ensuring a nearly diffraction limited profile of the focal spot.

Upon achieving this initial optimization, the center-of-mass of the near-field image is calculated. When inserting SPP, the location of the singularity point of SPP overlaps with the center-of-mass of NF, such that a most homogeneous intensity distribution of the donut-shaped focal spot can be obtained.

The spectrum of the laser pulse should be ensured to be symmetric to the central wavelength, as shown in Fig.7.9. This step is to reduce the challenge introduced when inserting the SPP, due to its inherent characteristics, where the l value varies across different frequencies.

To finely tune the donut-shaped focal spot in the presence of the SPP, additional corrections are applied by using Zernike polynomials for compensating the wavefront aberrations and the inhomogeneity of the NF profile.

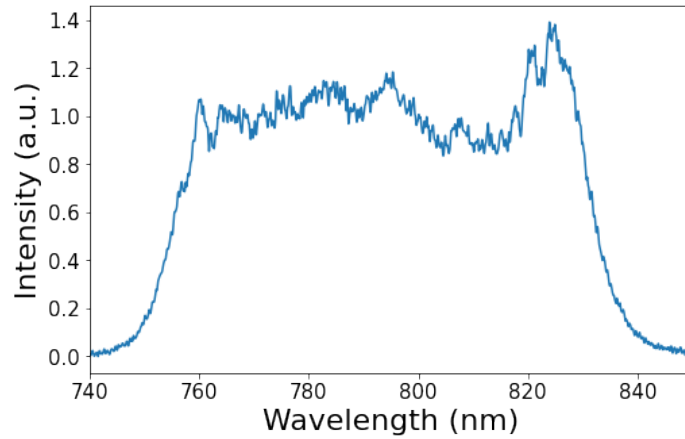


Figure 7.9: The spectrum measured, optimized to be symmetric to the central wavelength.

To determine the optimal linear combination of Zernike modes for achieving an

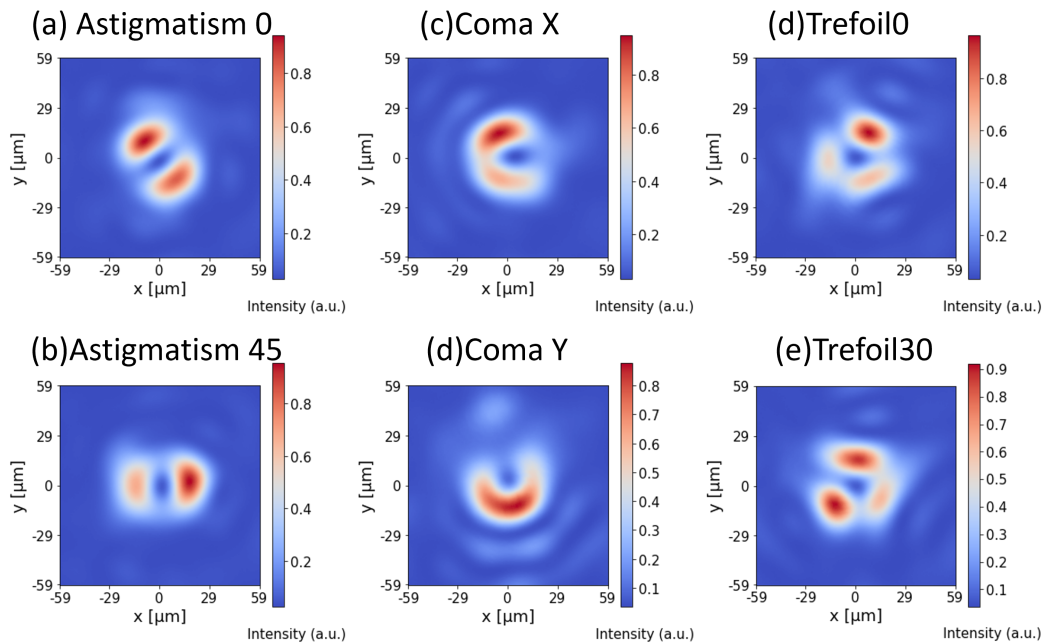


Figure 7.10: The focal spot profiles obtained for individual Zernike modes with RMS amplitudes of 0.1λ each, leading to the calculation of optimal coefficients for each mode to achieve the desired FF profile.

ideal donut-shaped focal spot, first the phase mask of each individual Zernike mode is applied, each with an RMS amplitude of 0.1λ , and recorded the resulting focal spot profiles, as shown in Fig.7.10. The coefficients for each Zernike mode were calculated to reach the ideal FF profile, which are as follows: 0 for astigmatism 0° , -0.03λ for

astigmatism 45° , -0.04λ for coma X, -0.03λ for coma Y, -0.01λ for trefoil 0° , and 0.01λ for trefoil 30° . The FF profile resulting from the combination of FF profiles with Zernike modes in these coefficients is depicted in Fig.7.11, alongside the lineout along the radii of inner HM, peak-to-peak, and outer HM. At the peak-to-peak radius of $15.4 \mu\text{m}$, the PtV intensity difference is significantly reduced to 0.18, and the standard deviation reduced to 0.05, indicating an improvement over the values presented in Fig.7.1.

After applying the phase mask that incorporates the calculated linear combination

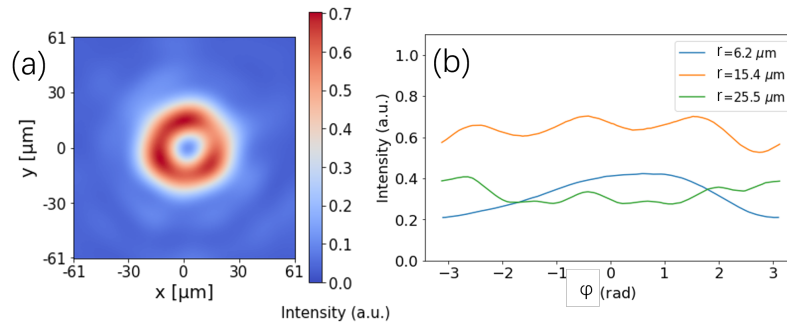


Figure 7.11: (a) Calculated FF profile as a result of the linear combination of Zernike modes, aiming for an ideal donut-shaped focal spot. (b) The lineout analysis along the radii of inner HM, peak-to-peak, and outer HM reveals a peak-to-peak radius of $15.4 \mu\text{m}$ where the PtV intensity difference is significantly minimized to 0.18 with a standard deviation of 0.05.

of Zernike modes using the adaptive optics, the resulting FF intensity distribution, as illustrated in Fig.7.12, shows a more homogeneous intensity distribution compared to the FF profile depicted in Fig.7.1. This enhancement is further quantified by examining the lineout along the radii of inner HM, peak-to-peak, and outer HM. At the peak-to-peak radius of $15.4 \mu\text{m}$, the PtV intensity difference is 0.28, with a standard deviation of 0.08. Although these values are slightly higher than those predicted by the computational model, the improvement in uniformity and symmetry of the FF intensity distribution, when compared to the initial FF profile before optimization with an RMS of 0.13 and PtV of 0.52, as shown in Fig.7.1 and Fig.7.12(c) and (d), is significant.

In conclusion, the optimization method employing a linear combination of Zernike modes has proven to be a highly effective strategy for improving the quality of the far-field intensity distribution of laser beams requiring a homogeneous doughnut-shaped focal spot. By meticulously adjusting the coefficients for specific Zernike modes to

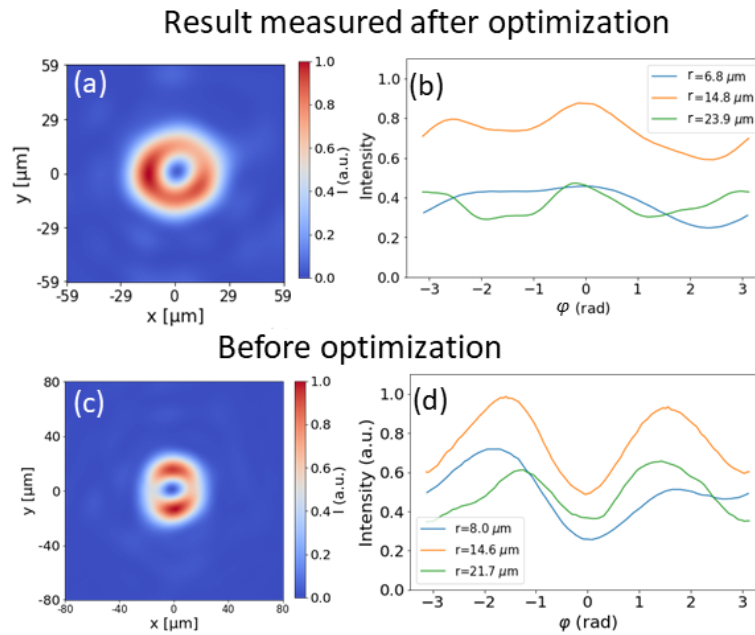


Figure 7.12: (a) Improved FF intensity distribution achieved through adaptive optics that applies the phase mask as a linear combination of Zernike modes. (b) the lineout along the radii of inner HM, peak-to-peak, and outer HM. (c)(d) are the measured results before optimization

counteract the aberrations introduced by the spiral phase plate, the non-uniformity of the near-field, and other system imperfections, this approach allows for a precise correction of the donut-shaped focal spot. The experimental results, showcasing a more uniform FF intensity profile, underscore the method's capability to compensate for the inhomogeneous intensity distribution and achieve a profile closer to the ideal focal spot.

8 Conclusion and Outlook

8.1 Conclusion

In this thesis, a comprehensive method for the high-precision characterization of ultra-short high-power laser pulses has been developed and analyzed, motivated by the LUXE project, which aims to explore the strong-field regime of Quantum Electrodynamics. By colliding high-power laser beams with electron bunches from the European XFEL or a secondary high-energy photon beam, LUXE seeks to investigate non-perturbative processes such as non-linear Compton scattering, Breit-Wheeler pair production, and the trident process. High-precision determination of laser intensity can significantly improve the precision of experimental results in LUXE, such as the pair creation rate.

To ensure the accuracy of the laser intensity measurement, it is crucial to reconstruct an identical focal spot at the diagnostic system by relay imaging the focal spot at the interaction point to the diagnostic system. The resulting focal spot shares the same profile as at the IP with negligible aberrations. It is sufficient to characterize this imaged focal spot at the diagnostic table. The only difference is the diameter of the focal spot, which is advantageous for high-precision measurement, as a larger focal spot size leads to higher resolution.

The intensity of a laser pulse can be determined by measuring the focal spot, energy, and pulse duration independently by assuming STC-free. The method includes high-resolution imaging of the focal spot, achieving a precision of 1%. The energy is determined by calculating the pixel values of the near field and calibrating the energy according to the spectrum at different locations, achieving a precision of up to the order of 10^{-5} . This is a significant improvement over the conventional energy meter, which has an uncertainty of 3%. The pulse duration measurement using the SRSI technique has an uncertainty of 0.2%. Overall, the combined precision is 1%, meeting the goal of this thesis.

The presence of spatio-temporal couplings adds complexity to intensity determination. To address this, the technique of INSIGHT is used to reconstruct the 3D electric field and phase at the focal spot. The results show a focal shift in the transversal plane and longitudinal direction due to the variations in wavefront for different wavelengths

when transmitting through lenses, resulting in a variation of the local spectrum across the focal spot plane. By including the local pulse duration in the analysis, the intensity precision can be improved by accurately determining the local intensity.

The diagnostic system can also be applied to laser pulses with more complex structures, such as Laguerre-Gaussian pulses with orbital angular momentum. However, such beams exhibit an uneven intensity distribution of their donut-shaped focal spot when generated using a spiral phase plate in JETi200. Various factors contributing to the focal spot intensity distribution are examined, including the near-field profile, alignment of the spiral phase plate, spectral components, and wavefront aberrations. A systematic method to optimize the focal spot profile, based on these factors and using a wavefront mask composed of Zernike modes, has been proven a success, with the flatness of the fluence along a certain radius improved.

8.2 Outlook

In the future, when applying this laser intensity diagnostic system to the LUXE project, several enhancements can be implemented to improve the precision and reliability of the experiment results.

First of all, it is crucial to image the focal spot at the interaction point to the diagnostic system accurately using the method of direct imaging using a OAP as discussed in Section 3.2.3. With a magnification of up to 250 times compared to the focal spot at IP, the precision of the focal spot size can be improved from 1% to 0.5%. This can be achieved by using a CCD camera with a large sensor size to capture the complete image of the focal spot with high resolution. Additionally, these cameras should be able to be cooled to significantly reduce noise caused by dark current.

Furthermore, measurements in this study were performed at low energy. When applied to the LUXE experiment, the laser will operate at full energy, necessitating further attenuation of the laser before it reaches the diagnostic table. It can be achieved by using a few glass wedges without introducing significant wavefront aberrations and each wedge has a reflection of approximately 3%. Consequently, during experiments, laser intensity diagnostics can be performed using only the attenuated laser at the diagnostic table.

Currently, the three-dimensional characterization of spatial-temporal couplings (STC)

is performed over multiple shots using INSIGHT or wavefront measurements with band-pass filters. There is a space for future research to employ techniques to achieve this characterization in a single shot [100], enhancing the efficiency and accuracy of the measurements.

The optimization of lasers with OAM has led to a more homogeneous distribution of donut-shaped focal spots. It has the potential for future applications, such as laser wakefield acceleration of ring-shaped electron beams [68] and the acceleration of positrons[67].

Bibliography

- [1] W. Greiner and J. Reinhardt, *Quantum Electrodynamics*. Physics and Astronomy, Springer Berlin Heidelberg, 2008.
- [2] G. Gabrielse, D. Hanneke, T. Kinoshita, M. Nio, and B. Odom, “New determination of the fine structure constant from the electron g value and qed,” *Phys. Rev. Lett.*, vol. 97, p. 030802, Jul 2006.
- [3] L. S. Brown and T. W. B. Kibble, “Interaction of intense laser beams with electrons,” *Phys. Rev.*, vol. 133, pp. A705–A719, Feb 1964.
- [4] G. Breit and J. A. Wheeler, “Collision of two light quanta,” *Phys. Rev.*, vol. 46, pp. 1087–1091, Dec 1934.
- [5] V. I. Ritus, “Quantum effects of the interaction of elementary particles with an intense electromagnetic field,” *Journal of Soviet Laser Research*, vol. 6, pp. 497–617, Sep 1985.
- [6] V. Dinu and G. Torgrimsson, “Trident process in laser pulses,” *Physical Review D*, vol. 101, Mar. 2020.
- [7] S. Tang and B. King, “Locally monochromatic two-step nonlinear trident process in a plane wave,” *Physical Review D*, vol. 107, May 2023.
- [8] T. G. Blackburn, “Radiation reaction in electron–beam interactions with high-intensity lasers,” *Reviews of Modern Plasma Physics*, vol. 4, Mar. 2020.
- [9] Abramowicz, H., Acosta, U., Altarelli, M., Aßmann, R., Bai, Z., Behnke, T., Benhammou, Y., Blackburn, T., Boogert, S., Borysov, O., Borysova, M., Brinkmann, R., Bruschi, M., Burkart, F., Büßer, K., Cavanagh, N., Davidi, O., Decking, W., Dosselli, U., Elkina, N., Fedotov, A., Firlej, M., Fiutowski, T., Fleck, K., Gostkin, M., Grojean, C., Hallford, J., Harsh, H., Hartin, A., Heinemann, B., Heinzl, T., Helary, L., Hoffmann, M., Huang, S., Huang, X., Idzik, M., Ilderton, A., Jacobs, R., Kämpfer, B., King, B., Lahno, H., Levanon, A., Levy, A., Levy, I., List, J., Lohmann, W., Ma, T., Macleod, A. J., Malka, V., Meloni, F., Mironov, A., Morandin, M., Moron, J., Negodin, E., Perez, G.,

- Pomerantz, I., Pöschl, R., Prasad, R., Quéré, F., Ringwald, A., Rödel, C., Rykovanov, S., Salgado, F., Santra, A., Sarri, G., Sävert, A., Sbrizzi, A., Schmitt, S., Schramm, U., Schuwalow, S., Seipt, D., Shaimerdenova, L., Shchedrolosiev, M., Skakunov, M., Soreq, Y., Streeter, M., Swientek, K., Hod, N. Tal, Tang, S., Teter, T., Thoden, D., Titov, A. I., Tolbanov, O., Torgrimsson, G., Tyazhev, A., Wing, M., Zanetti, M., Zarubin, A., Zeil, K., Zepf, M., and Zhemchukov, A., “Conceptual design report for the luxe experiment,” *Eur. Phys. J. Spec. Top.*, vol. 230, no. 11, pp. 2445–2560, 2021.
- [10] W. Heisenberg and H. Euler, “Consequences of dirac theory of the positron,” 2006.
- [11] J. Schwinger, “On gauge invariance and vacuum polarization,” *Phys. Rev.*, vol. 82, pp. 664–679, Jun 1951.
- [12] A. Hartin, A. Ringwald, and N. Tapia, “Measuring the boiling point of the vacuum of quantum electrodynamics,” *Physical Review D*, vol. 99, Feb. 2019.
- [13] A. K. Harding and D. Lai, “Physics of strongly magnetized neutron stars,” *Reports on Progress in Physics*, vol. 69, p. 2631, aug 2006.
- [14] V. Yakimenko, S. Meuren, F. Del Gaudio, C. Baumann, A. Fedotov, F. Fiuza, T. Grismayer, M. J. Hogan, A. Pukhov, L. O. Silva, and G. White, “Prospect of studying nonperturbative qed with beam-beam collisions,” *Phys. Rev. Lett.*, vol. 122, p. 190404, May 2019.
- [15] C. Bamber, S. J. Boege, T. Koffas, T. Kotseroglou, A. C. Melissinos, D. D. Meyerhofer, D. A. Reis, W. Ragg, C. Bula, K. T. McDonald, E. J. Prebys, D. L. Burke, R. C. Field, G. Horton-Smith, J. E. Spencer, D. Walz, S. C. Berridge, W. M. Bugg, K. Shmakov, and A. W. Weidemann, “Studies of nonlinear qed in collisions of 46.6 gev electrons with intense laser pulses,” *Phys. Rev. D*, vol. 60, p. 092004, Oct 1999.
- [16] C. Bula, K. T. McDonald, E. J. Prebys, C. Bamber, S. Boege, T. Kotseroglou, A. C. Melissinos, D. D. Meyerhofer, W. Ragg, D. L. Burke, R. C. Field, G. Horton-Smith, A. C. Odian, J. E. Spencer, D. Walz, S. C. Berridge, W. M. Bugg, K. Shmakov, and A. W. Weidemann, “Observation of nonlinear effects in compton scattering,” *Phys. Rev. Lett.*, vol. 76, pp. 3116–3119, Apr 1996.

-
- [17] J. M. Cole, K. T. Behm, E. Gerstmayr, T. G. Blackburn, J. C. Wood, C. D. Baird, M. J. Duff, C. Harvey, A. Ilderton, A. S. Joglekar, K. Krushelnick, S. Kuschel, M. Marklund, P. McKenna, C. D. Murphy, K. Poder, C. P. Ridgers, G. M. Samarin, G. Sarri, D. R. Symes, A. G. R. Thomas, J. Warwick, M. Zepf, Z. Najmudin, and S. P. D. Mangles, “Experimental evidence of radiation reaction in the collision of a high-intensity laser pulse with a laser-wakefield accelerated electron beam,” *Phys. Rev. X*, vol. 8, p. 011020, Feb 2018.
- [18] Z. Chen, S. Meuren, E. Gerstmayr, V. Yakimenko, P. H. Bucksbaum, and D. A. R. and, “Preparation of strong-field qed experiments at facet-ii,” in *Optica High-brightness Sources and Light-driven Interactions Congress 2022*, p. HF4B.6, Optica Publishing Group, 2022.
- [19] F. C. Salgado, *Design of a single-particle detection system for strong-field QED experiments*. PhD thesis, Jena, 2023. Dissertation, Friedrich-Schiller-Universität Jena, 2023.
- [20] J. Jaeckel and M. Spannowsky, “Probing mev to 90 gev axion-like particles with lep and lhc,” *Physics Letters B*, vol. 753, p. 482–487, Feb. 2016.
- [21] S. Knapen, T. Lin, H. K. Lou, and T. Melia, “Searching for axionlike particles with ultraperipheral heavy-ion collisions,” *Physical Review Letters*, vol. 118, Apr. 2017.
- [22] D. Strickland and G. Mourou, “Compression of amplified chirped optical pulses,” *Optics Communications*, vol. 56, no. 3, pp. 219–221, 1985.
- [23] J. W. Yoon, Y. G. Kim, I. W. Choi, J. H. Sung, H. W. Lee, S. K. Lee, and C. H. Nam, “Realization of laser intensity over 10^{23} w/cm²,” *Optica*, vol. 8, pp. 630–635, May 2021.
- [24] H. Abramowicz, M. A. Soto, M. Altarelli, R. Aßmann, A. Athanassiadis, G. Avoni, T. Behnke, M. Benettoni, Y. Benhammou, J. Bhatt, T. Blackburn, C. Blanch, S. Bonaldo, S. Boogert, O. Borysov, M. Borysova, V. Boudry, D. Breton, R. Brinkmann, M. Bruschi, F. Burkart, K. Büßer, N. Cavanagh, F. D. Corso, W. Decking, M. Deniaud, O. Diner, U. Dosselli, M. Elad, L. Epshteyn, D. Esperante, T. Ferber, M. Firlej, T. Fiutowski, K. Fleck, N. Fuster-Martinez, K. Gadow, F. Gaede, A. Gallas, H. G. Cabrera, E. Gerstmayr, V. Ghenescu,

- M. Giorato, N. Golubeva, C. Grojean, P. Grutta, G. Grzelak, J. Hallford, L. Hartman, B. Heinemann, T. Heinzl, L. Helary, L. Hendriks, M. Hoffmann, D. Horn, S. Huang, X. Huang, M. Idzik, A. Irles, R. Jacobs, B. King, M. Klute, A. Kropf, E. Kroupp, H. Lahno, F. L. Manghi, J. Lawhorn, A. Levanon, A. Levi, L. Levinson, A. Levy, I. Levy, A. Liberman, B. Liss, B. List, J. List, W. Lohmann, J. Maalmi, T. Madlener, V. Malka, T. Marsault, S. Mattiazzo, F. Meloni, D. Miron, M. Morandin, J. Moroń, J. Nanni, A. T. Neagu, E. Negodin, A. Paccagnella, D. Pantano, D. Pietruch, I. Pomerantz, R. Pöschl, P. M. Potlog, R. Prasad, R. Quishpe, E. Ranken, A. Ringwald, A. Roich, F. Salgado, A. Santra, G. Sarri, A. Sävert, A. Sbrizzi, S. Schmitt, I. Schulthess, S. Schuwalow, D. Seipt, G. Simi, Y. Soreq, D. Spataro, M. Streeter, K. Swientek, N. T. Hod, T. Teter, A. Thiebault, D. Thoden, N. Trevisani, R. Urmanov, S. Vasiukov, S. Walker, M. Warren, M. Wing, Y. C. Yap, N. Zadok, M. Zanetti, A. F. Żarnecki, P. Zbińkowski, K. Zembaczyński, M. Zepf, D. Zerwas, W. Ziegler, and M. Zuffa, “Technical design report for the luxe experiment,” 2023.
- [25] O. E. Vais and V. Y. Bychenkov, “Complementary diagnostics of high-intensity femtosecond laser pulses via vacuum acceleration of protons and electrons,” *Plasma Physics and Controlled Fusion*, vol. 63, p. 014002, nov 2020.
- [26] S. Jacquemot and P. Zeitoun, “APOLLON: a multi-PW laser facility,” in *X-Ray Lasers and Coherent X-Ray Sources: Development and Applications XIII* (A. Klisnick, ed.), vol. 11111, (San Diego, United States), p. 18, SPIE - International Society for Optics and Photonics, Aug. 2019.
- [27] “Atlas.” <https://www.pulse.physik.uni-muenchen.de/research/high-power/atlas/index.html>. Accessed: 2024-05-22.
- [28] K. Nakamura, H.-S. Mao, A. J. Gonsalves, H. Vincenti, D. E. Mittelberger, J. Daniels, A. Magana, C. Toth, and W. P. Leemans, “Diagnostics, control and performance parameters for the bella high repetition rate petawatt class laser,” *IEEE Journal of Quantum Electronics*, vol. 53, no. 4, pp. 1–21, 2017.
- [29] C. Radier, O. Chalus, M. Charbonneau, S. Thambirajah, G. Deschamps, S. David, J. Barbe, E. Etter, G. Matras, S. Ricaud, and et al., “10 pw peak power femtosecond laser pulses at eli-np,” *High Power Laser Science and Engineering*, vol. 10, p. e21, 2022.

-
- [30] H.-H. Chu, S.-Y. Huang, L.-S. Yang, T.-Y. Chien, Y.-F. Xiao, J.-Y. Lin, C.-H. Lee, S.-Y. Chen, and J. Wang, “A versatile 10-tw laser system with robust passive controls to achieve high stability and spatiotemporal quality,” *Applied Physics B*, vol. 79, pp. 193–201, Jul 2004.
- [31] W. Cho, S. I. Hwang, C. H. Nam, M. R. Bionta, P. Lassonde, B. E. Schmidt, H. Ibrahim, F. Légaré, and K. T. Kim, “Temporal characterization of femtosecond laser pulses using tunneling ionization in the uv, visible, and mid-ir ranges,” *Scientific Reports*, vol. 9, p. 16067, Nov 2019.
- [32] C. Smeenk, J. Z. Salvail, L. Arissian, P. B. Corkum, C. T. Hebeisen, and A. Staudte, “Precise in-situ measurement of laser pulse intensity using strong field ionization,” *Opt. Express*, vol. 19, pp. 9336–9344, May 2011.
- [33] W. C. Wallace, O. Ghafur, C. Khurmi, S. Sainadh U, J. E. Calvert, D. E. Laban, M. G. Pullen, K. Bartschat, A. N. Grum-Grzhimailo, D. Wells, H. M. Quiney, X. M. Tong, I. V. Litvinyuk, R. T. Sang, and D. Kielpinski, “Precise and accurate measurements of strong-field photoionization and a transferable laser intensity calibration standard,” *Phys. Rev. Lett.*, vol. 117, p. 053001, Jul 2016.
- [34] H. Hu, H. Xu, Y. Bai, R. T. Sang, I. V. Litvinyuk, P. Liu, and R. Li, “Wavelength and intensity effects on the dissociation of H_2^+ in intense laser fields,” *Phys. Rev. A*, vol. 94, p. 053415, Nov 2016.
- [35] K. Krajewska, F. C. Véléz, and J. Z. Kamiński, “High-energy ionization for intense laser pulse diagnostics,” *Plasma Physics and Controlled Fusion*, vol. 61, p. 074004, may 2019.
- [36] M. F. Ciappina, E. E. Peganov, and S. V. Popruzhenko, “Focal-shape effects on the efficiency of the tunnel-ionization probe for extreme laser intensities,” *Matter and Radiation at Extremes*, vol. 5, no. 4, p. 044401, 2020.
- [37] A. L. Galkin, M. P. Kalashnikov, V. K. Klinkov, V. V. Korobkin, M. Y. Romanovsky, and O. B. Shiryayev, “Electrodynamics of electron in a superintense laser field: New principles of diagnostics of relativistic laser intensity,” *Physics of Plasmas*, vol. 17, no. 5, p. 053105, 2010.

- [38] M. Kalashnikov, A. Andreev, K. Ivanov, A. Galkin, V. Korobkin, M. Romanovsky, O. Shiryaev, M. Schnuerer, J. Braenzel, V. Trofimov, and et al., “Diagnostics of peak laser intensity based on the measurement of energy of electrons emitted from laser focal region,” *Laser and Particle Beams*, vol. 33, no. 3, p. 361–366, 2015.
- [39] F. Mackenroth, A. R. Holkundkar, and H.-P. Schlenvoigt, “Ultra-intense laser pulse characterization using ponderomotive electron scattering,” *New Journal of Physics*, vol. 21, p. 123028, dec 2019.
- [40] A. R. Holkundkar and F. Mackenroth, “Characterization of ultra-intense laser in radiation damping regime using ponderomotive scattering,” *Plasma Physics and Controlled Fusion*, vol. 64, p. 045019, feb 2022.
- [41] J. Gao, “Laser intensity measurement by thomson scattering,” *Applied Physics Letters*, vol. 88, no. 9, p. 091105, 2006.
- [42] O. Har-Shemesh and A. D. Piazza, “Peak intensity measurement of relativistic lasers via nonlinear thomson scattering,” *Opt. Lett.*, vol. 37, pp. 1352–1354, Apr 2012.
- [43] Z. Léczy and A. Andreev, “Diagnostics of peak laser intensity by pair production from thin foil target,” *Laser Physics Letters*, vol. 17, p. 056101, apr 2020.
- [44] D. Kane and R. Trebino, “Characterization of arbitrary femtosecond pulses using frequency-resolved optical gating,” *IEEE Journal of Quantum Electronics*, vol. 29, no. 2, pp. 571–579, 1993.
- [45] R. Trebino, K. W. DeLong, D. N. Fittinghoff, J. N. Sweetser, M. A. Krumbügel, B. A. Richman, and D. J. Kane, “Measuring ultrashort laser pulses in the time-frequency domain using frequency-resolved optical gating,” *Review of Scientific Instruments*, vol. 68, no. 9, pp. 3277–3295, 1997.
- [46] C. Iaconis and I. A. Walmsley, “Spectral phase interferometry for direct electric-field reconstruction of ultrashort optical pulses,” *Opt. Lett.*, vol. 23, pp. 792–794, May 1998.
- [47] I. Sytceвич, C. Guo, S. Mikaelsson, J. Vogelsang, A.-L. Viotti, B. Alonso, R. Romero, P. T. Guerreiro, I. nigo J. Sola, A. L’Huillier, H. Crespo, M. Miranda, and C. L. Arnold, “Characterizing ultrashort laser pulses with second

- harmonic dispersion scans,” *J. Opt. Soc. Am. B*, vol. 38, pp. 1546–1555, May 2021.
- [48] T. Oksenhendler, S. Coudreau, N. Forget, V. Crozatier, S. Grabielle, R. Herzog, O. Gobert, and D. Kaplan, “Self-referenced spectral interferometry,” *Applied Physics B*, vol. 99, pp. 7–12, Apr 2010.
- [49] Fastlite, “Wizzler.” <https://fastlite.com/produits/wizzler-ultrafast-pulse-measurement/>. Accessed: 2024-05-22.
- [50] N. Minkovski, G. I. Petrov, S. M. Saltiel, J. Etchepare, and O. Albert, “Nonlinear polarization rotation and orthogonal polarization generation experienced in a single-beam configuration,” *JOSA B, Vol. 21, Issue 9, pp. 1659-1664*, vol. 21, pp. 1659–1664, sep 2004.
- [51] J.-C. Chanteloup, “Multiple-wave lateral shearing interferometry for wave-front sensing,” *Appl. Opt.*, vol. 44, pp. 1559–1571, Mar 2005.
- [52] Imagine Optic, “Haso4 126 broadband.” <https://www.imagine-optic.com/products/haso4-126-broadband/>. Accessed: 2024-05-22.
- [53] M. Miranda, M. Kotur, P. Rudawski, C. Guo, A. Harth, A. L’Huillier, and C. L. Arnold, “Spatiotemporal characterization of ultrashort laser pulses using spatially resolved fourier transform spectrometry,” *Opt. Lett.*, vol. 39, pp. 5142–5145, Sep 2014.
- [54] A. Borot and F. Quéré, “Spatio-spectral metrology at focus of ultrashort lasers: a phase-retrieval approach,” *Opt. Express*, vol. 26, pp. 26444–26461, Oct 2018.
- [55] N. Weisse, J. Esslinger, S. Howard, F. M. Foerster, F. Haberstroh, L. Doyle, P. Norreys, J. Schreiber, S. Karsch, and A. Döpp, “Measuring spatio-temporal couplings using modal spatio-spectral wavefront retrieval,” *Opt. Express*, vol. 31, pp. 19733–19745, Jun 2023.
- [56] J.-C. Diels and W. Rudolph, “1 - fundamentals,” in *Ultrashort Laser Pulse Phenomena (Second Edition)* (J.-C. Diels and W. Rudolph, eds.), pp. 1–60, Burlington: Academic Press, second edition ed., 2006.
- [57] A. E. Siegman, *Lasers / Anthony E. Siegman*. Mill Valley, Calif: University Science Books, 1986.

- [58] ISO, “Iso 11146-1:2021(en) lasers and laser-related equipment —test methods for laser beam widths, divergence angles and beam propagation ratios —part 1: Stigmatic and simple astigmatic beams,” 2021.
- [59] L. Allen, M. W. Beijersbergen, R. J. C. Spreeuw, and J. P. Woerdman, “Orbital angular momentum of light and the transformation of laguerre-gaussian laser modes,” *Phys. Rev. A*, vol. 45, pp. 8185–8189, Jun 1992.
- [60] N. R. Heckenberg, R. McDuff, C. P. Smith, and A. G. White, “Generation of optical phase singularities by computer-generated holograms,” *Opt. Lett.*, vol. 17, pp. 221–223, Feb 1992.
- [61] M. Scipioni, R. K. Tyson, and J. Viegas, “Mode purity comparison of optical vortices generated by a segmented deformable mirror and a static multilevel phase plate,” *Appl. Opt.*, vol. 47, pp. 5098–5102, Oct 2008.
- [62] Q. Wang, X. W. Sun, and P. Shum, “Generating doughnut-shaped beams with large charge numbers by use of liquid-crystal spiral phase plates,” *Appl. Opt.*, vol. 43, pp. 2292–2297, Apr 2004.
- [63] G. Ruffato, M. Massari, and F. Romanato, “Generation of high-order laguerre-gaussian modes by means of spiral phase plates,” *Opt. Lett.*, vol. 39, pp. 5094–5097, Sep 2014.
- [64] M. Massari, G. Ruffato, M. Gintoli, F. Ricci, and F. Romanato, “Fabrication and characterization of high-quality spiral phase plates for optical applications,” *Appl. Opt.*, vol. 54, pp. 4077–4083, May 2015.
- [65] D. G. Grier, “A revolution in optical manipulation,” *Nature*, vol. 424, pp. 810–816, Aug 2003.
- [66] L. Schermelleh, R. Heintzmann, and H. Leonhardt, “A guide to super-resolution fluorescence microscopy,” *Journal of Cell Biology*, vol. 190, pp. 165–175, 07 2010.
- [67] J. Vieira and J. T. Mendonça, “Nonlinear laser driven donut wakefields for positron and electron acceleration,” *Phys. Rev. Lett.*, vol. 112, p. 215001, May 2014.

- [68] G.-B. Zhang, M. Chen, J. Luo, M. Zeng, T. Yuan, J.-Y. Yu, Y.-Y. Ma, T.-P. Yu, L.-L. Yu, S.-M. Weng, and Z.-M. Sheng, “Acceleration of on-axis and ring-shaped electron beams in wakefields driven by Laguerre-Gaussian pulses,” *Journal of Applied Physics*, vol. 119, p. 103101, 03 2016.
- [69] L. Yu, H. M. Zhao, Q. Cao, X. Z. Zhu, J. L. Li, B. Y. Li, F. Liu, M. Chen, and Z. M. Sheng, “Guiding of laguerre-gaussian pulses in high-order plasma channels,” *Plasma Physics and Controlled Fusion*, vol. 64, p. 075009, jun 2022.
- [70] R. J. Noll, “Zernike polynomials and atmospheric turbulence*,” *J. Opt. Soc. Am.*, vol. 66, pp. 207–211, Mar 1976.
- [71] V. N. Mahajan, “Strehl ratio for primary aberrations in terms of their aberration variance,” *J. Opt. Soc. Am.*, vol. 73, pp. 860–861, Jun 1983.
- [72] S. Akturk, X. Gu, P. Bowlan, and R. Trebino, “Spatio-temporal couplings in ultrashort laser pulses,” *Journal of Optics*, vol. 12, p. 093001, aug 2010.
- [73] M. Rhodes, Z. Guang, J. Pease, and R. Trebino, “Visualizing spatiotemporal pulse propagation: First-order spatiotemporal couplings in laser pulses,” *Applied Optics*, vol. 56, p. 3024, 04 2017.
- [74] S. Akturk, X. Gu, E. Zeek, and R. Trebino, “Pulse-front tilt caused by spatial and temporal chirp,” *Opt. Express*, vol. 12, pp. 4399–4410, Sep 2004.
- [75] Z. Guang, M. Rhodes, and R. Trebino, “Measurement of the ultrafast lighthouse effect using a complete spatiotemporal pulse-characterization technique,” *J. Opt. Soc. Am. B*, vol. 33, pp. 1955–1962, Sep 2016.
- [76] Zemax, LLC, “Zemax optical studio.” <https://www.zemax.com>, 2024. Version 21.3, Accessed: 2024-05-22.
- [77] Optical Surface, “Off-axis paraboloids.” <https://www.optisurf.com/index.php/products/off-axis-paraboloids/>, 2023.
- [78] Helmholtz Institute Jena, “Jeti200 laser.” https://www.hi-jena.de/en/helmholtz_institute_jena/about-the-institute/experimental-facilities/local/jeti200-laser, 2024. Accessed: 2024-06-06.

- [79] N. Minkovski, G. I. Petrov, S. M. Saltiel, O. Albert, and J. Etchepare, “Nonlinear polarization rotation and orthogonal polarization generation experienced in a single-beam configuration,” *J. Opt. Soc. Am. B*, vol. 21, pp. 1659–1664, Sep 2004.
- [80] A. Jullien, O. Albert, F. Burgy, G. Hamoniaux, J.-P. Rousseau, J.-P. Chambaret, F. Augé-Rochereau, G. Chériaux, J. Etchepare, N. Minkovski, and S. M. Saltiel, “ 10^{-10} temporal contrast for femtosecond ultraintense lasers by cross-polarized wave generation,” *Opt. Lett.*, vol. 30, pp. 920–922, Apr 2005.
- [81] Amplitude, “Sequoia.” https://amplitude-laser.com/add_ons/metrology/sequoia/, 2024. Accessed: 2024-06-06.
- [82] S. Keppler, A. Sävert, J. Koerner, M. Hornung, H. Liebetrau, J. Hein, and M. Kaluza, “The generation of amplified spontaneous emission in high-power CPA laser systems,” *Laser Photonics Review*, vol. 10, p. 264, 03 2016.
- [83] Amplitude, “Titan.” https://amplitude-laser.com/products/nanosecond-lasers/flashlamps_pumped_lasers/titan/, 2024. Accessed: 2024-06-06.
- [84] P. Tournois, “Acousto-optic programmable dispersive filter for adaptive compensation of group delay time dispersion in laser systems,” *Optics Communications*, vol. 140, no. 4, pp. 245–249, 1997.
- [85] ISP System, “Deformable mirror.” <https://www.isp-system.fr/en/products/opto-mechanics/deformable-mirror/>, 2024. Accessed: 2024-06-06.
- [86] F. C. Salgado, A. Kozan, D. Seipt, D. Hollatz, P. Hilz, M. Kaluza, A. Sävert, A. Seidel, D. Ullmann, Y. Zhao, and M. Zepf, “All-optical source size and emittance measurements of laser-accelerated electron beams,” *Phys. Rev. Accel. Beams*, vol. 27, p. 052803, May 2024.
- [87] C. Zepf, A. Seidel, M. Zepf, M. C. Kaluza, and A. Sävert, “Role of spatiotemporal couplings in stimulated Raman side scattering,” *Phys. Rev. Res.*, vol. 5, p. L012023, Feb 2023.

- [88] A. Seidel, B. Lei, C. Zepf, M. C. Kaluza, A. Sävert, M. Zepf, and D. Seipt, “Polarization and cep dependence of the transverse phase space in laser driven accelerators,” *Phys. Rev. Res.*, vol. 6, p. 013056, Jan 2024.
- [89] M. Yeung, J. Bierbach, E. Eckner, S. Rykovanov, S. Kuschel, A. Sävert, M. Förster, C. Rödel, G. G. Paulus, S. Cousens, M. Coughlan, B. Dromey, and M. Zepf, “Noncollinear polarization gating of attosecond pulse trains in the relativistic regime,” *Phys. Rev. Lett.*, vol. 115, p. 193903, Nov 2015.
- [90] AlliedVision, “Prosilica gt downloads.” <https://www.alliedvision.com/en/support/technical-documentation/prosilica-gt-documentation/>. Accessed: 2024-05-22.
- [91] Onsemi, “Image sensors | kai-02050.” <https://www.onsemi.com/products/sensors/image-sensors/KAI-02050>. Accessed: 2024-05-22.
- [92] T. Oksenhendler, “Self-referenced spectral interferometry theory,” 2012. Available at <https://doi.org/10.48550/arXiv.1204.4949>.
- [93] Gentec-EO, “Laser energy measurement.” https://www.gentec-eo.com/products?Type=energy&ProductFilterParamViewModel.MaxMeasurableEnergys=_1mJTo1J#page:1. Accessed: 2024-05-22.
- [94] C.-Y. Hu, H.-J. He, B.-Q. Chen, Z.-Y. Wei, and Z.-Y. Li, “Theoretical solution to second-harmonic generation of ultrashort laser pulse,” *Journal of Applied Physics*, vol. 122, no. 24, p. 243105, 2017.
- [95] L.-H. Hong, B.-Q. Chen, C.-Y. Hu, and Z.-Y. Li, “Spatial-temporal evolution of ultrashort laser pulse second harmonic generation in β -barium borate (β -bbo) crystal,” *Journal of Applied Physics*, vol. 129, no. 23, p. 233102, 2021.
- [96] J. V. Thompson, B. H. Hokr, G. A. Throckmorton, D. Wang, M. O. Scully, and V. V. Yakovlev, “Enhanced second harmonic generation efficiency via wavefront shaping,” *ACS Photonics*, vol. 4, no. 7, pp. 1790–1796, 2017.
- [97] I. V. Il’ina, T. Y. Cherezova, and A. V. Kudryashov, “Gerchberg—saxton algorithm: experimental realisation and modification for the problem of formation of multimode laser beams,” *Quantum Electronics*, vol. 39, p. 521, jun 2009.

- [98] R. Feng, J. Qian, Y. Peng, Y. Li, W. Li, Y. Leng, and R. Li, “Terawatt-class few-cycle short-wave infrared vortex laser,” *Ultrafast Science*, vol. 3, p. 0039, 2023.
- [99] J. B. Ohland, D. Posor, U. Eisenbarth, V. Iancu, R. Ungureanu, D. Ursescu, and V. Bagnoud, “Zernike-coefficient extraction via helical beam reconstruction for optimization (zebro) in the far field,” *High Power Laser Science and Engineering*, vol. 11, p. e86, 2023.
- [100] S. Howard, J. Esslinger, R. H. W. Wang, P. Norreys, and A. Döpp, “Hyperspectral compressive wavefront sensing,” *High Power Laser Science and Engineering*, vol. 11, p. e32, 2023.

Danksagung

Finally, I have reached the end of my PhD journey. I am filled with gratitude and joy. This journey, with its ups and downs, has been one of the most important experiences of my life. I have no regrets, only thanks for everyone who helped me along the way. From the bottom of my heart, I thank my supervisors, Matt and Alex. Your patience, guidance, and support have been crucial to my success. I couldn't have asked for better mentors.

To my lab partner, Yu Zhao, thank you for all the late nights we spent working together in the lab. Your dedication and friendship made the hard times easier.

Many thanks to George for your work on the JETi200 laser, giving us a reliable laser source for our research. I really appreciate your efforts and help.

A big thank you to Pooyan for your help in the lab and for lending me many optics. Isra, my dear sista/officie, sharing our office with you has been a joy. Our talks, laughter, and girls' time together have been a great source of comfort.

I also would like to thank Andreas and Carola, for sharing your experience in the lab. Thank you to everyone in our group for the wonderful times we spent together. Whether it was lunch times, movie nights, drinks, barbecues, boat-rowing, or moving houses, these moments made the tough PhD journey much easier and less stressful. Your company and friendship turned the hard days into memorable ones.

Unfortunately, the COVID-19 pandemic started just two months after I began my PhD. It has brought many challenges to my life and work. Quarantined in a nearly empty new apartment, I faced the isolation and uncertainty of my life. I am deeply grateful to my friend Jin Zhuo. Though you are far away in Japan with a time difference of 8 hours, our time together for online chatting and gaming helped me survive those hard times.

In the end, I am forever grateful to my parents, for their unconditional love and support.

我永远感激我的父母，即使我们远隔万里，这些年来只能通过视频见面，依然给予我无条件的爱与支持。

轻舟已过万重山。